Scanning Tunneling Microscopy of Electrically Driven Phase Transitions in a Charge Density Wave Material

by

Sean Walker

A thesis
presented to the University of Waterloo
in fulfillment of the
thesis requirement for the degree of
Doctor of Philosophy
in
Chemistry (Quantum Information)

Waterloo, Ontario, Canada, 2022

Examining Committee Membership

The following served on the Examining Committee for this thesis. The decision of the Examining Committee is by majority vote.

External Examiner:	Neil Curson Professor, University College London
Supervisor:	Jonathan Baugh Associate Professor, University of Waterloo
Internal Members:	Shirley Tang Professor, University of Waterloo
Internal-External Member:	Guo-Xing Miao Associate Professor, University of Waterloo
Other Member:	Germán Sciaini Associate Professor, University of Waterloo

Author's Declaration

This thesis consists of material all of which I authored or co-authored: see Statement of Contributions included in the thesis. This is a true copy of the thesis, including any required final revisions, as accepted by my examiners.

I understand that my thesis may be made electronically available to the public.

Statement of Contributions

Material in Chapters 2, 3 and 4 has been adapted from,

> **Walker, S. M.**, Patel, T, Okamoto, J, Langenberg, D, Bergeron, E. A., Gao, J., Luo, X., Lu, W., Sun, Y. P., Tsen, A. W., and Baugh, J. Observation and manipulation of a phase separated state in a charge density wave material. *Nano Letters* **2022**, *22*, 1929 – 1936 [1].

Author Contributions:

- S. M. Walker and T. Patel conceived of the project.
- S. M. Walker performed the scanning tunneling microscopy experiments, the transport measurements, and the data analysis.
- T. Patel fabricated the samples with supervision from A. W. Tsen.
- J. Okamoto carried out the time-dependent Ginzburg-Landau simulations.
- D. Langenberg contributed to the scanning tunneling microscopy experiments.
- E. A. Bergeron contributed to the understanding of the phase separated state.
- Jingjing Gao, Xuan Luo, Wenjian Lu and Yuping Sun grew the crystals of 1T-TaS_2.
- J. Baugh supervised the project.
- S. M. Walker led the writing of the manuscript, with contributions from all co-authors.

Abstract

The 1T polytype of the van der Waals material TaS_2, has been studied extensively as a strongly correlated system. Exhibiting several different charge density wave (CDW) states, the phase diagram of 1T-TaS_2 has been explored for close to fifty years, as the forces driving the formation of the charge modulation and determining the characteristics of each of the phases, have been elucidated. In recent years, interest in this system has concerned expanding the phase diagram, with the bulk equilibrium states being further probed and manipulated. While much of the research has focused on the low-temperatures phase, where 1T-TaS_2 has emerged as a test bed for Mott physics, as the material is thinned towards the 2D limit, its phase diagram shows significant deviations from that of the bulk system, even in the higher temperature range. Optoelectronic maps of ultrathin (< 10 nm thick) 1T-TaS_2 have indicated the presence of non-equilibrium CDW phases within the hysteresis region of the nearly commensurate (NC) to commensurate (C) transition. The work in this thesis investigates the nature of these non-equilibrium phases, and in doing so, further elucidates the phase diagram of ultrathin 1T-TaS_2.

We perform scanning tunneling microscopy (STM) on exfoliated ultrathin flakes of 1T-TaS_2 within the NC-C hysteresis window. Imaging exfoliated flakes using STM poses certain difficulties. Specifically, STM is very sensitive to surface contamination and is ill-suited for locating a specific region of interest in a sample with micron scale dimensions. We address the challenges associated with performing STM on exfoliated materials, utilizing a simple device design that allows for the *in situ* measurement of both the electrical properties of an exfoliated flake and the topography of the flake. With such a device design, it is possible to correlate changes in electronic structure with changes in the bulk properties of the material.

When imaging ultrathin 1T-TaS_2 within the NC-C transition region, we find that rather than possessing distinct electronic order, the topography of the flake indicates the presence of intertwined, irregularly shaped NC-like and C-like domains. After applying lateral electrical signals to the sample, we image changes in the geometric arrangement of the different regions. The ability to measure the change in electronic structure with the application of a driving signal provides an invaluable perspective on the evolution of the CDW phases in the material at the nanoscale. Inhomogeneity similar to what we measure in ultrathin 1T-TaS_2, has been seen in related strongly correlated systems, such as perovskite manganites and doped Mott insulators. Starting with a phase separation model to simulate the observed inhomogeneity, we incorporate ideas derived from percolation theory to explore the relationship between the electronic structure present in ultrathin 1T-TaS_2 and its bulk resistivity. With this model, we are able to qualitatively reproduce many of the

features observed when driving the inhomogeneous CDW state. These results highlight the importance of understanding the role of phase competition in determining the properties of strongly correlated systems.

Acknowledgements

I would first like to acknowledge my supervisor, Jonathan Baugh. Additionally, I would like to recognize my advisory committee, Guo-xing Miao, Kathryn Preuss, and Shirley Tang, for their advice throughout my graduate studies. I would also like to thank Neil Curson and Germán Sciaini, for being a part of my thesis defence committee.

I would like to especially thank Deler Langenberg for keeping the STM up and running, and for always being willing to offer his expertise. And Junichi Okamoto, for working with me on the time-dependent Ginzburg-Landau simulations.

To the people I have met over my time at IQC. Annelise, for always being supportive, offering insightful comments, and for being endlessly willing to humour my many rants, diatribes, and soliloquies, usually accompanied by at least one cup of coffee. Kay, for our many long conversations, and for being one of the most dedicated and thorough researchers I have had the joy of meeting. Kyle, for spending multiple hours with me trying to figure out a project I could pursue with carbon nanotubes. My officemates, Eduardo and Brandon, for always being willing to lend an ear. And many of the other members of the group over the years, for patiently listening to me during group meetings.

To Chris and John and Harmeny, for making RAC the best home away from home it could possibly be, given its obvious limitations. And Cathy, for always being willing to help me navigate all of the administrative challenges that come with graduate studies.

Lastly, I would like to thank my family, especially my mother and father, for always thinking science was just as interesting as I found it to be.

And Lindsey, for your seemingly limitless support and patience. It is impossible to articulate the depths of your contributions to this thesis.

Table of Contents

List of Figures

List of Tables

List of Abbreviations

1T-TaS_2	1T polytype of tantalum disulfide
AFI	Antiferromagnetic insulating
C	Commensurate CDW phase
CDW	Charge density wave
DFT	Discrete Fourier transform
FFT	Fast Fourier transform
FM	Ferromagnetic metallic
FT	Fourier transform
GL	Ginzburg-Landau
hBN	Hexagonal boron nitride
HOPG	Highly oriented pyrolytic graphite
IC	Incommensurate CDW phase
LDOS	Local density of states
NC	Nearly commensurate CDW phase
PDMS	Polydimethylsiloxane
PLD	Periodic lattice distortion
PPC	Polypropylene carbonate

SPM	Scanning probe microscopy
STM	Scanning tunneling microscopy
STS	Scanning tunneling spectroscopy
TDGL	Time-dependent Ginzburg-Landau
TEM	Transmission electron microscopy
TMD	Transition metal dichalcogenide
XPS	X-ray photoelectron spectroscopy
XRD	X-ray diffraction

Chapter 1

Introduction

Dimensionality plays an integral role in determining the properties of a system. While in the past, research into 2D phenomenon has depended largely on the engineering of quasi-2D systems [2], with the isolation of graphene via mechanical exfoliation, the experimental expertise became available to probe the effect of dimensionality on many layered van der Waals materials [3–5]. Insulators, semiconductors, superconductors, and other materials possessing different exotic properties, have all been isolated and studied [6]. Furthermore, with the development of polymer transfer techniques, the possibility of assembling multiple 2D materials into heterostructures has opened up a new avenue for the engineering of systems possessing novel and interesting physics [7].

Strongly correlated electronic systems exhibit rich phase diagrams often characterized by competing phases with different kinds of order [8]. Charge, spin, lattice, and orbital degrees of freedom can all play a part and contribute to the existence of a variety of states exhibiting a range of bulk properties, including high-temperature superconductivity [9] and electronic inhomogeneity [10, 11]. Inhomogeneity at the nanoscale, arising from non-statistical fluctuations, has been observed in many complex systems. In this context, we adopt the definition of complexity outlined in [8] and [12]: in a complex system where many particles interact, the properties of the system are not entirely determined by those of the constituent components, but instead correlations betweens the particles give rise to emergent behaviours. The origins of these novel behaviours can be traced to both the properties of the equilibrium phases involved and the nature of the competition between them. Beyond being interesting from a purely fundamental perspective, when two equilibrium states with vastly different properties are nearly degenerate, small external stimuli that serve to drive a phase transition between the two states have the potential to produce

a large change in bulk observables [13]. Harnessing this behaviour could lead to advances in sensing and memory technologies.

The 1T polytype of the transition metal dichalcogenide (TMD) TaS_2 has been studied extensively, due to the variety of charge density wave (CDW) phases it exhibits [14]. Each of the equilibrium CDW phases displays distinct properties. Characterizing the many behaviours of these states, and determining the origin of the features of the different CDW phases, has been the basis of research into 1T-TaS_2 for almost fifty years. In particular, the low-temperature phase of 1T-TaS_2 has attracted significant interest due to the strong electron correlations it exhibits. Within a certain temperature region, the phase is believed to behave as a Mott insulator [15, 16]. Furthermore, the low-temperature phase is amenable to perturbation, and the exploration and manipulation of this state has motivated 1T-TaS_2 as a test bed for Mott physics. While significant effort has been devoted to characterizing the low-temperature phase of this material, with many competing equilibrium phases, 1T-TaS_2 is sensitive to a wide range of external stimuli in many temperature regimes. The expansion of the phase diagram of 1T-TaS_2 by thinning the material to the ultrathin limit is the primary focus of this thesis.

1.1 Thesis overview

This thesis is organized as follows. The rest of this chapter begins by introducing charge density waves (CDW), describing phenomenologically their basic characteristics, and the origins of CDW phases. A short introduction to the transition metal dichalcogenide (TMD) studied in this thesis, the 1T polytype of TaS_2, is then given. After introducing the equilibrium CDW phases observed in this system, and the differences in their bulk properties, we discuss some of the efforts in the literature to expand the phase diagram of 1T-TaS_2. Lastly, the fundamentals of the principle measurement technique used throughout this work, scanning tunneling microscopy (STM), are presented.

Chapter 2 expands upon the nature of the equilibrium phases in 1T-TaS_2, with particular emphasis on how these phases are observed and analyzed using STM. The phenomenological Ginzburg-Landau theory for CDWs is summarized, with the primary goal of introducing useful notation for describing CDW phases. Armed with this description of CDWs, we present data that illustrates the characteristics of the two bulk CDW phases that are observed within the temperature range studied in this thesis: the nearly commensurate (NC)-commensurate (C) transition region. Through explaining this data, we introduce some general STM analysis techniques. Lastly, some of the considerations required for imaging exfoliated ultrathin flakes of 1T-TaS_2 with STM are discussed, and a

device design is presented that consists of an ultrathin flake integrated into a nanodevice. The design allows for the *in situ* measurement of both the bulk electrical properties of the sample and the topography of the integrated flake, making it possible to correlate changes in electrical behaviour with changes in electronic structure.

Utilizing the device design described in the previous chapter, Chapter 3 presents results pertaining to the CDW phases observed in exfoliated ultrathin flakes of 1T-TaS_2. The electrical properties of ultrathin flakes of 1T-TaS_2 are discussed, and a brief overview of the literature pertaining to possible explanations for these properties is given. Results of STM measurements on ultrathin flakes are then presented. A state with electronic inhomogeneity is imaged using STM and manipulated through the application of lateral electrical signals to the sample. The evolution of the state is captured over multiple STM scans. This study is the first work conducted on the electronic structure of exfoliated ultrathin flakes of 1T-TaS_2 at the atomic scale within the NC-C transition temperature range.

In Chapter 4 a model of phase separation is utilized for explaining the nature of the inhomogeneous state observed in the previous chapter. After outlining some of the basic thermodynamics underpinning phase separation, the dynamics of the separation process are modelled, producing microstructures consisting of the constituent phases arranged in a variety of geometric patterns. This model is extended to qualitatively reproduce some of the changes observed when the inhomogeneous state is manipulated.

1.2 Background

1.2.1 Charge density waves

Figure 1.1 depicts a simple 1D model that can be used to describe the formation of a charge density wave [17]. A collection of particles connected by harmonic springs interacts with a potential. The atoms possess a periodicity with the lattice constant a_0, while the potential oscillates with the wavelength b. Depending on the strength of the potential, if it is energetically favourable, the system of particles will distort and form a periodic superstructure with the new wavelength a. If this new periodicity is a rational fraction of the periodicity of the potential, then the superstructure is said to have locked in to the underlying potential, forming a commensurate superstructure. However, if the potential is not sufficiently strong, the harmonic term describing the interaction between pairs of atoms dominates, and the system will not lock in, forming an incommensurate modulation.

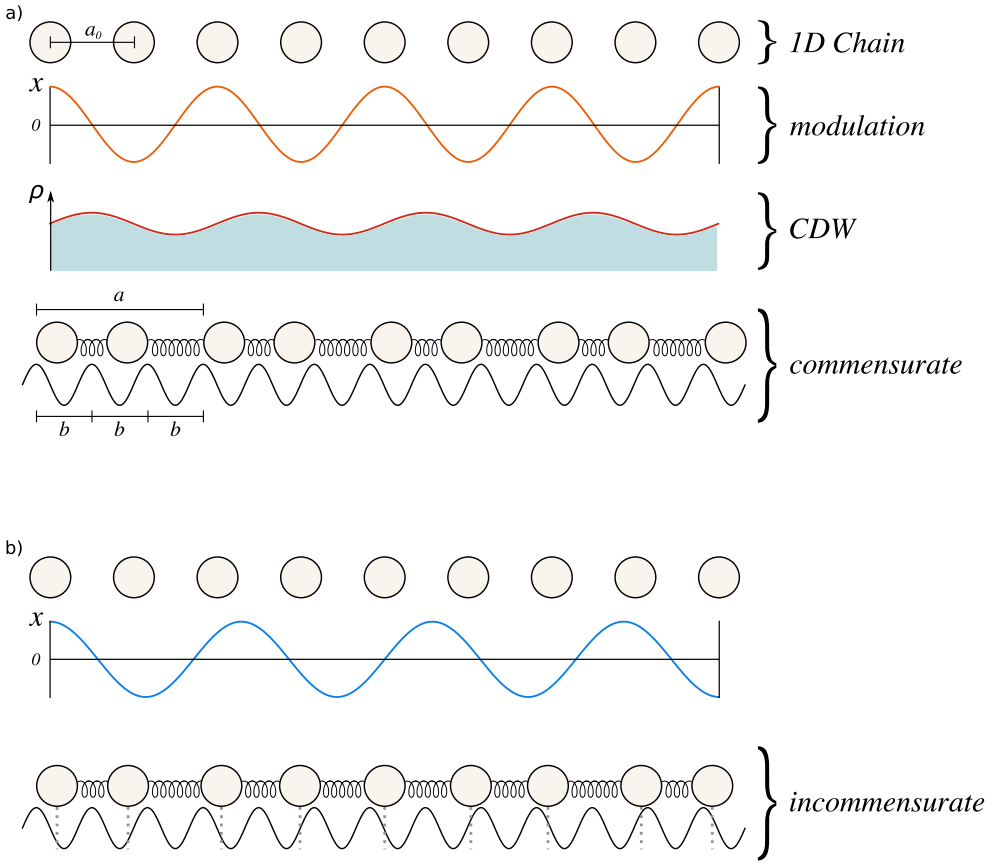

Figure 1.1: Commensurate and incommensurate lattice modulations. (a) The orange curve demonstrates a possible distortion that modulates a one-dimensional chain of atoms such that the resulting structure forms a CDW (red curve) commensurate with the potential with wavelength b. (b) The blue curve demonstrates a possible distortion that modulates a one-dimensional chain of atoms such that the resulting structure forms an incommensurate superstructure. The gray dotted lines mark the locations of the modulated lattice relative to the underlying potential, demonstrating the incommensurability of the two.

This basic picture describes many different systems with different dimensionalities, including the adsorption of atoms on a surface, the intercalation of a van der Waals material with another compound, or a 3D structure with two interpenetrating lattices. In certain condensed matter systems, rather than stemming from two distinct chemical species, the interaction can arise between conduction electrons and their corresponding atomic lattice. In this case, a periodic lattice distortion (PLD) is coupled with a modulation of the conduction electron density, forming what is called a charge density wave (CDW). Assuming the density is cosinusoidally modulated, the wave can be written as [18]

$$\rho\left(\boldsymbol{r}\right) = \rho_0\left(\boldsymbol{r}\right)\left[1 + \phi_0 \cos\left(\boldsymbol{q_0 r} + \phi\right)\right], \tag{1.1}$$

where ϕ_0, $\boldsymbol{q_0}$, and ϕ are the amplitude, wave vector and phase of the CDW, and $\rho_0\left(\boldsymbol{r}\right)$ represents the unmodulated density. The function describing the accompanying PLD itself, is then given by,

$$u_n = u_0 \sin\left(n|\boldsymbol{q_0}|a_0 + \phi\right), \tag{1.2}$$

where the index n runs over each of the atoms in the 1D chain, u_0 represents the magnitude of the atomic displacement, and a_0 is the unperturbed lattice constant. In Figure 1.1a, the orange curve represents a possible lattice distortion that results in the formation of a commensurate superstructure. The resulting modulation in charge density, ρ, is given by the red curve. Figure 1.1b demonstrates an example of an incommensurate lattice distortion; the modulation generated by the blue curve results in a superstructure that does not align with the underlying potential.

The different lenses through which CDW formation is viewed can be delineated based on whether the CDW phase exhibits long-range order or short-range order. In the long-coherence-length picture, it is natural to view the CDW as a distortion in $\boldsymbol{k}$ space, with the Fermi surface playing a significant role. On the other hand, when the CDW displays a shorter coherence length, the local environment becomes more relevant, and CDW formation can be discussed in terms of local interactions, such as through a chemical bonding picture or through Mott physics. The mechanisms of CDW formation can also be differentiated based upon the fundamental nature of the interaction that stabilizes the CDW state. When studying a distortion rooted in $\boldsymbol{k}$ space, the Peierls instability, which is based on electron-phonon coupling, is often discussed as the driving force behind the CDW formation. In other cases, electron-electron interactions, such as the Coulombic forces observed in Mott physics, will be the driver.

An understanding of the bulk CDW phases in the class of materials studied in this thesis, layered Ta dichalcogenides, is an active field of research [19–23]. Elucidating the origin of the CDW phases in these materials is not the goal of this thesis, but in the

remainder of this section we present the typical outline of the CDW problem in 1D using a mean field theory of a coupled electron-phonon system, [24, 25], for the purposes of introducing the reader to the considerations that guide CDW formation. After giving some of the governing equations for the energetics of a 1D CDW system, we summarize the basic results, leading to an instability condition for the qualitative prediction of CDW formation. While a complete microscopic theory for understanding CDW phases in 2D systems remains elusive, we describe some of the considerations that distinguish the 2D problem from the 1D problem, and provide some intuition for understanding a 2D CDW material, like 1T-TAS_2. The goal of this introduction is to provide the reader with a brief overview of many of the concepts found in the CDW literature, specifically the Peierls instability, the giant Kohn anomaly and Fermi surface nesting. While the widespread applicability of these models to real-world materials is questionable [26], they provide a useful framework for discussing many of the interactions behind the formation of CDWs. In a later section, Section 1.2.2, we round out this survey of CDW formation by discussing the origins of CDW phases in the primary material system studied in this thesis, 1T-TaS_2, in terms of a local bonding picture and Mott physics. Much of this material follows the presentation in [18] and [24].

The Peierls instability

The tendency for a 1D system to distort and form a CDW is often defined as a Peierls instability, and is a consequence of electron-phonon coupling. In a Peierls distortion, a modulation of an atomic lattice, and the formation of a CDW, opens a gap at the Fermi surface, lowering the energy of occupied states while raising the energy of unoccupied states (Figure 1.2). If this energy gain is larger than the Coulombic and elastic energy cost accompanying the distortion, this modified lattice represents the ground state of the system. In this context CDW and PLD are used interchangeably; rather than viewing this instability as being electronically driven the formation of a CDW is seen as a structural phase transition where the charge modulation and the lattice distortion go hand in hand.[1]

To describe the energetics of the coupled electron-phonon system, we start with a Fröhlich Hamiltonian in second quantized form [27],

$$\mathcal{H} = \sum_{\boldsymbol{k}} \epsilon_{\boldsymbol{k}} a^{+}_{\boldsymbol{k}} a_{\boldsymbol{k}} + \sum_{\boldsymbol{q}} \hbar\omega_{\boldsymbol{q}} b^{+}_{\boldsymbol{q}} b_{\boldsymbol{q}} + \frac{1}{\sqrt{N}} \sum_{\boldsymbol{k},\boldsymbol{q}} g_{\boldsymbol{q}} a^{+}_{\boldsymbol{k}+\boldsymbol{q}} a_{\boldsymbol{k}} \left(b^{+}_{-\boldsymbol{q}} + b_{\boldsymbol{q}} \right), \tag{1.3}$$

[1] It is important to note that even in cases where electron-electron interactions drive CDW formation, a PLD is still commonly observed.

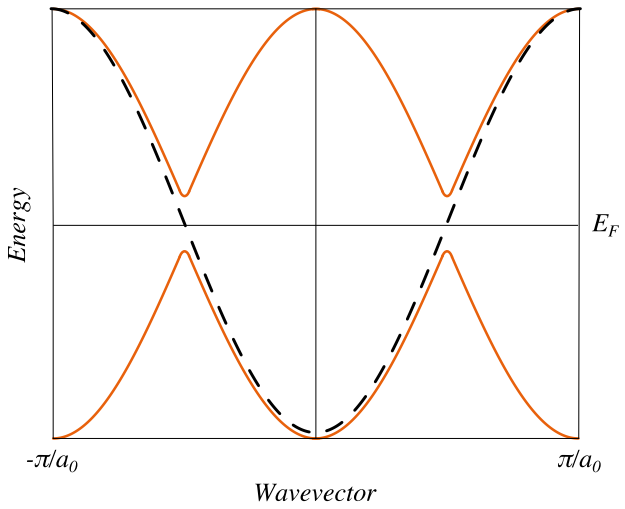

Figure 1.2: Effect of the Peierls instability on the electronic dispersion curve. A gap is opened up in the dispersion curve of a one-dimensional system with the formation of a CDW (orange curve). The dispersion curve of the undistorted system is given by the black dashed line.

where $\epsilon_{\boldsymbol{k}}$ is the energy of the electronic state $\boldsymbol{k}$, $a^+_{\boldsymbol{k}}$ and $a_{\boldsymbol{k}}$ are creation and annihilation operators for $\boldsymbol{k}$, $\omega_{\boldsymbol{q}}$ is the frequency of the phonon mode $\boldsymbol{q}$, $b^+_{\boldsymbol{q}}$ and $b_{\boldsymbol{q}}$ are the creation and annihilation operators for $\boldsymbol{q}$, $g_{\boldsymbol{q}}$ is the electron-phonon coupling constant, and N is the number of lattice sites per unit length. The first and second terms of this Hamiltonian describe the electronic and phonon spectra respectively, while the last term captures the coupling between the different electron and phonon modes, where the wave vector is conserved. To evaluate the favourability of CDW formation, we need to consider the changes in the electronic energy spectrum, and the induced lattice strain. From second order perturbation theory, the change in the electronic energy due to the CDW is related to the potential $\nu_{\boldsymbol{q}}$ formed by the static displacement, u_q, of the phonon mode $\boldsymbol{q}$ that accompanies the modulation:

$$\delta E_{band} = -|\nu_{\boldsymbol{q}}|^2 \chi_0 (\boldsymbol{q}) . \tag{1.4}$$

The function $\chi_0 (\boldsymbol{q})$ is the non-interacting electronic susceptibility and is defined as,

$$\chi_0 (\boldsymbol{q}) = \frac{1}{L} \sum_{\boldsymbol{k}} \frac{f_{\boldsymbol{k}+\boldsymbol{q}} - f_{\boldsymbol{k}}}{\epsilon_{\boldsymbol{k}} - \epsilon_{\boldsymbol{k}+\boldsymbol{q}}} > 0, \tag{1.5}$$

where $f_{\boldsymbol{k}}$ is the value of the Fermi function for the energy $f (\epsilon_{\boldsymbol{k}})$ and L is the length of the one-dimensional system. Lastly, the energy of the lattice strain associated with the

phonon displacement is given by,

$$\delta E_{lattice} = \frac{1}{2} M \omega_{\boldsymbol{q}}^2 u_{\boldsymbol{q}}^2. \tag{1.6}$$

where M is the mass of the ions in the 1D chain. If $\delta E_{band} + \delta E_{lattice} < 0$, CDW formation is favoured, where the wave vector of the resulting modulation is defined as $\boldsymbol{q_0}$.

The susceptibility defined in Equation 1.5 is directly related to the electronic energy gain, and thus is a useful parameter for comparing CDW formation in different regimes. Consider the case of a 1D chain of atoms described by the lattice constant a_0, with a half-filled band, and assuming a tight-binding dispersion, $\epsilon_{\boldsymbol{k}} = -E_F \cos(k a_0)$, with the Fermi energy E_F and the Fermi vector $|\boldsymbol{k}_F| = \pi/2a_0$. For this system, the susceptibility is found to diverge as a function of temperature when evaluated at $\boldsymbol{q} = 2\boldsymbol{k}_F$, specifically in the limit where $E_F/k_B T$ is large:

$$\chi_0(2\boldsymbol{k}_F, T) = \frac{1}{2} N(0) \ln\left(\frac{2.28 E_F}{k_B T}\right), \tag{1.7}$$

where $N(0)$ is the density of states at E_F.[2] The temperature-dependent peaking of χ_0 has a large impact on the energy gain defined by Equation 1.4, and results in a renormalization of the phonon mode around $2\boldsymbol{k}_F$. At the transition temperature this mode is softened, a phenomenon known as the giant Kohn anomaly. The renormalized phonon frequency is given by,

$$\tilde{\omega}_{\boldsymbol{q}}^2 = \omega_{\boldsymbol{q}}^2 \left(1 - \frac{4 g_{\boldsymbol{q}}^2}{\hbar \omega_{\boldsymbol{q}}} \chi_0(\boldsymbol{q})\right). \tag{1.8}$$

A complete softening of the phonon mode at the wave vector $\boldsymbol{q}_0 = 2k_F$ corresponds to a frozen-in lattice distortion, the formation of the CDW. When this occurs, the wavelength of the density wave, $\boldsymbol{q_0}$ is,

$$\lambda_0 = \frac{2\pi}{|\boldsymbol{q}_0|} = \frac{\pi}{|\boldsymbol{k}_F|}. \tag{1.9}$$

Therefore, the wavelength of the CDW is found to be dependent on the Fermi wave vector $\boldsymbol{k}_F$. Considering $\boldsymbol{k}_F$ is unrelated to the underlying crystal lattice, being determined by the filling of the electronic bands in $\boldsymbol{k}$ space, the CDW arising from the Peierls instability is typically incommensurate with the 1D chain of atoms.

[2]The concept of "density of states" is discussed in greater detail in Section 1.2.3 in the context of the meaning of the data collected using scanning tunneling microscopy.

From Equation 1.8, one can derive a simple condition for determining whether CDW formation in a 1D system is favourable:

$$\frac{4g_{\boldsymbol{q}}^2}{\hbar\omega_{\boldsymbol{q}}} - 2U_{\boldsymbol{q}} + V_{\boldsymbol{q}} \geq \frac{1}{\chi_0\left(\boldsymbol{q}\right)}, \tag{1.10}$$

where the additional electronic energy parameters $U_{\boldsymbol{q}}$ and $V_{\boldsymbol{q}}$, the Coulomb and exchange interactions respectively, are included. In this condition, all of the relevant microscopic parameters are assumed to be independent of $\boldsymbol{k}$. This condition is sufficiently reliable to be employed in practice, and reinforces some basic intuition regarding the Peierls instability: CDW formation is favoured by a strong electron-phonon coupling ($g_{\boldsymbol{q}}$), a strong exchange interaction ($V_{\boldsymbol{q}}$), a weak Coulomb interaction ($U_{\boldsymbol{q}}$), a small lattice strain ($\omega_{\boldsymbol{q}}$), and by a large non-interacting susceptibility ($\chi_0(\boldsymbol{q})$).

2D charge density wave systems and Fermi surface nesting

The situation becomes more complicated when considering CDW formation in 2D systems. In particular, the role of the non-interacting electronic susceptibility and the shape of the Fermi surface play substantially different roles depending on the dimensionality of the system. In discussing the formation of a CDW in a 1D chain of atoms we have highlighted the importance of the non-interacting electronic susceptibility. The energy gain associated with CDW formation is related to the logarithmic divergence of the susceptibility at the transition temperature. In 2D, the peaking of the susceptibility is both weaker and broader, spread out over a range of wave vectors. Consequently, the susceptibility plays a significantly smaller role in driving CDW formation in 2D materials compared to 1D systems.

The Peierls instability can be discussed in the context of the shape of the Fermi surface. In 3D $\boldsymbol{k}$ space the Fermi surface of a 1D chain of atoms is planar, and is located at the same location where discontinuities are formed in the energy dispersion curves after the charge modulation (Figure 1.2). Fermi surface nesting occurs when a part of the Fermi surface is displaced by a vector $\boldsymbol{q_0}$ such that it can be completely superimposed on another portion of the Fermi surface. Therefore, for a 1D system, Fermi surface nesting is *perfect* in that all points on the Fermi surface can be mapped onto another portion of the contour (Figure 1.3a). For a system with perfect Fermi surface nesting, the gap created at the Fermi energy is complete (at $T = 0$). On the other hand, for a two dimensional system, the Fermi surface typically has a more complex geometry (Figure 1.3b), and Fermi surface nesting will be *partial*. In this case, some spectral density will exist within the CDW gap ($N\left(0\right) > 0$). As a result, the Fermi surface also plays a significantly smaller role in driving

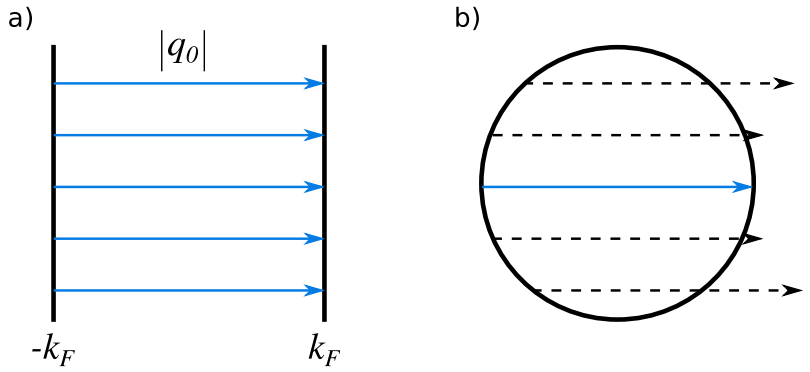

Figure 1.3: (a) A cross-section of the planar Fermi surface of a 1D chain of atoms. The blue vectors corresponding to $\boldsymbol{q_0}$ perfectly map one part of the Fermi surface on another. (b) A cross-section of a cylindrical Fermi surface in a 2D system. The Fermi surface nesting, represented by the blue vector, is incomplete.

CDW formation compared to in 1D systems. A comparison between CDW formation in 1D and 2D systems is summarized in Table 1.1. Although the relative importance of the forces that drive CDW formation in 1D and 2D systems may differ, many of the general concepts and terminology, (the Peierls instability, Fermi surface nesting, giant Kohn anomaly), can be used in describing experimental results pertaining to CDW phases in 2D systems.

	1D	2 D
Fermi surface:		
Geometry	Planar	Cylindrical
Nesting	Perfect	Partial
Electronic susceptibility:		
$\boldsymbol{q}$ dependence	log divergence	weak peaking
T dependence	log divergence	weak peaking
Kohn anomaly	lage, sharp	small, broad
CDW energy gap	complete	partial

Table 1.1

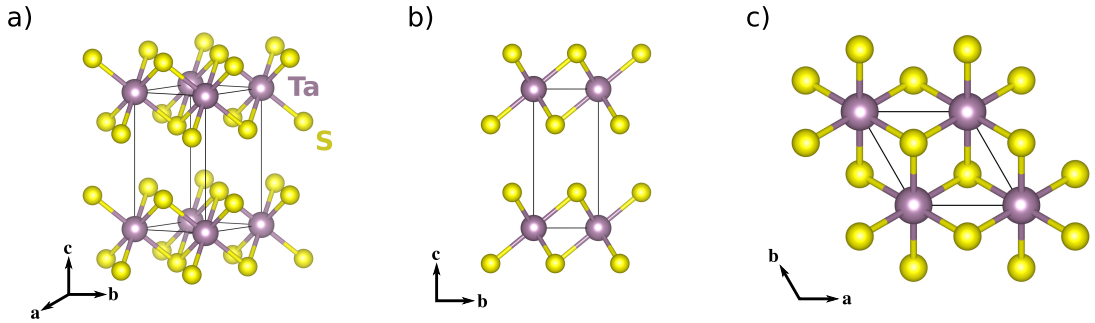

Figure 1.4: (a) The unit cell of 1T-TaS_2. (b) The unit cell of 1T-TaS_2 viewed along the a axis. This view illustrates the S-Ta-S trilayer building block of the material. (c) A top view of 1T-TaS_2 illustrating the arrangement of Ta atoms within a single layer of the material. This figure was generated using the software package described in [28], from the crystallographic data collected in [29].

1.2.2 1T-TaS_2: structure, charge density wave phases and electrical properties

The transition metal dichalcogenide (TMD) TaS_2 is a van der Waals material that exists as multiple polytypes, differing based on the stacking of a trilayer S-Ta-S building block. The 2H and 1T polytypes are the most widely studied, as both configurations form CDW phases. In the 2H polytype, the trilayer adopts a trigonal prismatic geometry, while in the 1T polytype, the Ta are octahedrally coordinated. The 2H polytype is the equilibrium form of TaS_2, while the 1T polytype can be synthesized by quenching the material from above 1073 K in a chalcogen rich atmosphere. Different views of the crystal structure of 1T-TaS_2 are given in Figure 1.4. As with all van der Waals systems, the layers of the crystal are held together with van der Waals forces, making it possible to isolate thin flakes of the material through mechanical exfoliation [30–32]. Elucidating emergent properties of 1T-TaS_2 in the 2D limit is the primary research goal of this thesis.

1T-TaS_2 has been extensively studied due to its rich phase diagram comprising a variety of charge density wave phases [14]. All of the CDW phases in 1T-TaS_2 are triple CDWs, consisting of the superposition of three distinct 1D charge modulations.[3] The system undergoes a series of successive first-order phase transitions upon cooling: starting as a normal metal,[4] it forms an incommensurate CDW (IC) at $\sim$ 543 K, a nearly commensurate

[3] As opposed to a single CDW, which is composed of a single modulation frequency mode.

[4] It is challenging to study the region of the phase diagram of 1T-TaS_2 where it exists as a normal metal as the material undergoes a structural phase change to the 2H polytype in this temperature range.

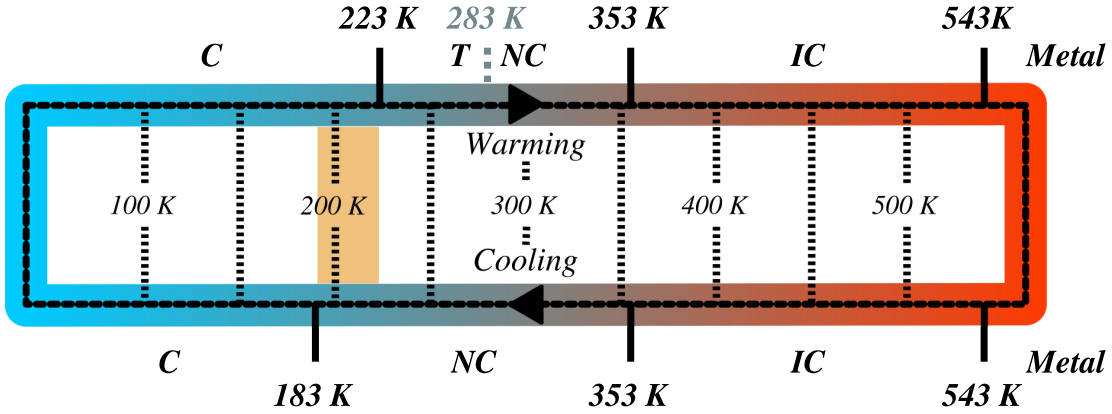

Figure 1.5: The evolution of the CDW phases in 1T-TaS_2 with thermal cycling. The region in orange corresponds to hysteresis observed between the NC-C phase transition.

CDW (NC) at $\sim$ 353 K, and lastly a commensurate CDW (C) at $\sim$ 183 K. Each of the equilibrium phases of 1T-TaS_2 has a characteristic electronic, structural and orbital order [33], and a jump in resistivity is observed with each transition as the material becomes more insulating as it is cooled. The resistivities of the NC and C phase differ by approximately one order of magnitude (see, for example, Figure 3.1 in Section 3.2). When the material is warmed from the C phase, the transition to the NC state progresses through the T phase, a state with a similar resistivity to the NC phase but a different electronic structure. The transition to the T phase occurs at 223 K and the full transition to the NC phase occurs at 283 K. Figure 1.5 presents the series of phase transitions observed as 1T-TaS_2 is thermally cycled. As is often seen with first-order phase transitions, when the sample is warmed from the C phase, hysteresis is observed in the NC-C phase transtion (orange shading in Figure 1.5).

The NC phase is an incommensurate modulation, but one whose wave vector nearly satisfies commensurability. In the IC phase, the CDW is aligned with the atomic lattice vector. When the material is cooled towards the C phase, the incommensurate modulation changes, rotating away from the underlying lattice, forming the NC state. As the system is cooled further, the NC state continuously evolves, becoming more commensurate, until the transition to the fully commensurate state occurs. Therefore, the charge ordering of the NC phase is variable, with different parameters reported in the literature dependent on the temperature at which the measurements were taken. When the CDW modulation is nearly commensurate, harmonics of the fundamental wave vector give rise to electronic features known in the literature as domain walls. The T phase is characteristically similar to the NC phase, being an incommensurate CDW state with a wave vector that is nearly

Phase	Temperature (K)	θ (°)	Description
Normal	$T > 543$		No CDW exists.
Incommensurate (IC)	$543 > T > 353$	0	Incommensurate CDW aligned with underlying lattice.
Nearly commensurate (NC)	$283 < T < 353$ (warming) $353 > T > 183$ (cooling)	$11 - 13$	CDW with hexagonal domain structure.
Triclinic (T)	$223 < T < 283$ (warming)	12-13	CDW with quasi-1D domain structure.
Commensurate (C)	$T < 223$ (warming) $T < 183$ (cooling)	13.9	Commensurate CDW.

Table 1.2: CDW phases in 1T-TaS_2. The T phase has not been typically measured upon cooling. Furthermore, the upper boundary of the temperature range in which the T phase is observed upon warming should be considered approximate.

commensurate with the underlying system. However, the domain walls observed in the T phase exhibit a lower symmetry compared to the NC phase.[5] Given the similarities between the T and NC phases, the T phase is often ignored in the phase diagram of 1T-TaS_2, especially when the focus is on the electrical properties of the different phases. Table 1.2 summarizes the characteristics of the different bulk CDW phases in 1T-TaS_2.

CDW formation in 1 T−TaS_2

Earlier in this chapter we discussed some of the interactions that govern the formation of a CDW state in a material. In this section, we delve deeper into the origins of the CDW phases in 1T-TaS_2 specfically. Below the NC-C transition temperature, in the commensurate CDW region of the 1T-TaS_2 phase diagram, x-ray photoelectron spectroscopy (XPS) and STM measurements reveal the coexistence of multiple Ta valencies that differ by up to 0.4 electrons per atom. The presence of inequivalent Ta sites suggests that local bonding plays a pronounced role in the formation of the commensurate CDW. Based on the modelling of local bonding energies, it is now understood that the Ta lattice distorts as depicted in Figure 2.1, with 13 Ta atoms forming a star-shaped cluster. This distortion results in the occupied Ta 5d t_{2g} energy levels being split into three submanifolds and a net decrease in energy [34–37].

While the above, qualitative description of CDW formation in 1T-TaS_2 is generally accepted, a complete understanding of the bulk phases in 1T-TaS_2 is still very much an

[5] A more detailed description of each of the equilibrium CDW phases of 1T-TaS_2 is provided in Chapter 2 of this thesis.

open question. Recent results in the literature have delved into the nature of the low-temperature, insulating phase, and the correlation between CDW stacking and the bulk properties of the material. Evidence exists both for the low-temperature phase constituting a Mott insulator [15, 16, 34, 35, 38], and for the electrical behaviour arising from band insulating behaviour due to the dimerization of adjacent layers of the material, akin to an interlayer Peierls-like distortion [19, 20, 39]. The phase diagram of 1T-TaS_2 is diverse, with a complexity that arises from the existence of different competing interactions. This debate as to the origin of the low-temperature insulating state has prompted further study into whether the phase diagram of 1T-TaS_2 exhibits even greater complexity than previously thought.

Having discussed the qualitative behaviour underlying the Peierls instability, we conclude this section by introducing the basics of Mott physics for completeness. A Mott insulator is a system that behaves as an insulator despite having an unfilled valence band. This behaviour stems from electron-electron correlations, and demonstrates the interplay between the potential energy cost of electron localization, and the kinetic energy of electron delocalization. This interplay is captured by the Hubbard model, expressed by the Hamiltonian,

$$H = -\sum_{\langle ij\rangle,\sigma} t_{ij}\left(c^{+}_{i\sigma}c_{j\sigma} + c^{+}_{j\sigma}c_{i\sigma}\right) + U\sum_{i} n_{i\uparrow}n_{i\downarrow}. \tag{1.11}$$

The first term in Equation 1.11 describes electron hopping between neighbours i and j, while the second term encompasses the Coulombic repulsion that exist when two electrons with opposite spins are located in the same atomic orbital.[6] It is the electron hopping that gives rise to conduction in the Hubbard model. When taking into account only the on-site repulsive contribution of the second term (i.e. where $t = 0$), each atomic orbital in the energy spectrum of the system is split, based upon the electron occupation number. When an atomic orbital is singly occupied, the energy is given by ϵ. Adding a second electron to the orbital comes with the energy cost U, producing a stepwise function. When t is finite, the split energy levels centred at ϵ and $\epsilon + U$ broaden, with a width given by the strength of the hopping parameter and the number of neighbours participating in the hopping (Figure 1.6). The bulk electrical behaviour of the system will depend on the ratio of the parameters U and t. If the split bands overlap, the material will behave as a metal. However, in the event a gap is formed between the bands, as in Figure 1.6, the material will display the electrical behaviour of an insulator, despite the fact that the valence shell is not completely filled. In the context of 1T-TaS_2, the periodic lattice distortion that accompanies the CDW formation in the C phase results in the localization of an electron

[6] In the Hubbard model, the tight binding approximation is assumed.

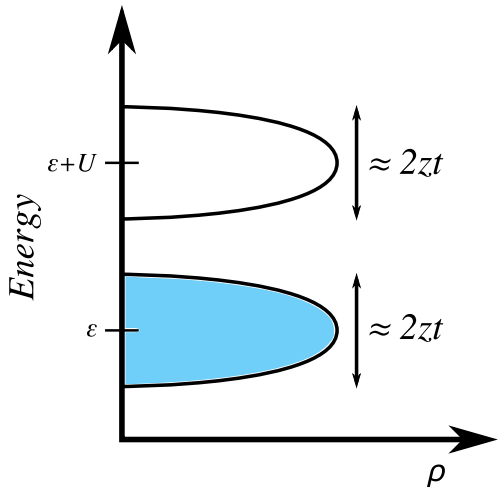

Figure 1.6: The band structure of a Mott insulator. From the Hubbard Hamiltonian, the hopping of electrons gives rise to subbands centred at the atomic energy level, ϵ, and the sum of ϵ and the on-site repulsion parameter U. The width of the subband depends upon the strength of the hopping, t, and the number of neighbours, z. The density of states is represented by ρ.

on the central Ta atom in the star-shaped cluster. It is because of this electron localization that 1T-TaS_2 garnered initial interest for exhibiting the properties of a Mott insulator [35].

Non-equilibrium CDW phases

Moving beyond the equilibrium phases of 1T-TaS_2, the phase diagram is expanded through the application of certain external stimuli or by modifying select material parameters. By applying pressure or by chemically doping the Mott insulating C phase, the material becomes superconducting at low temperatures [32, 40, 41]. Through voltage pulses applied normal to the crystal surface via a metallic tip [42, 43], or through laser photoexcitation[44, 45], non-equilibrium hidden states, possessing distinctive electronic textures, are accessed. The characterization and manipulation of these states have motivated 1T-TaS_2 as a test bed for the exploration of novel avenues of Mott physics.

1.2.3 Scanning tunneling microscopy

Lastly, we introduce some of the fundamental principles behind the primary experimental technique used in this thesis, scanning tunneling microscopy (STM). Scanning probe microscopy (SPM) describes a set of experimental techniques that consist of rastering a tip, whose properties will vary depending on the specific technique being employed, across the surface of a sample. Based upon the interactions between the tip and the surface, different types of information about the sample is obtained. This family of techniques is inherently a surface probe and thus does not necessarily convey any information concerning any bulk material properties. STM is a well known SPM technique that uses the fundamental principle of quantum tunneling to probe the electronic spectrum of the surface of the sample being measured. In STM a metallic tip is brought into close contact with a conductive sample and is rastered across the surface as the current that arises due to quantum tunneling is measured. This tunneling current is translated into topographic information with a resolution on the atomic length scale. In addition to spatial resolution, it is also possible to obtain energy resolution as well, providing information about how the electronic spectrum of a material varies in real-space. This type of experiment is called scanning tunneling spectroscopy (STS). In this section we introduce some of the theoretical underpinnings of STM experiments. For a more exhaustive treatment of the subject we refer the reader to some of the numerous textbooks written on the subject [46–49].

Quantum tunneling

One of the more interesting results encountered in quantum mechanics is the ability for a particle with kinetic energy E, to pass through a potential energy barrier V_0, even in the case where $E < V_0$. The wavefunction of a particle incident on a potential barrier will contain some finite magnitude beyond the barrier, i.e. the particle has the capability of *tunneling* through the barrier. Figure 1.7 establishes the parameters of the one-dimensional tunneling problem. A particle with energy, E, and whose wavefunction is given by $\psi = e^{ikz}$, is incident upon a potential barrier with a height given by $V = V_0$. We start with the one-dimensional, time-independent Schrödinger equation,

$$\frac{\hbar^2}{2m}\frac{\partial^2}{\partial z^2}\psi(z) = [V(z) - E]\,\psi(z)\,. \tag{1.12}$$

Inserting the wave function of the incident particle, ψ, defined as the plane wave above,

$$-\frac{\hbar^2}{2m}k^2 = V(z) - E, \tag{1.13}$$

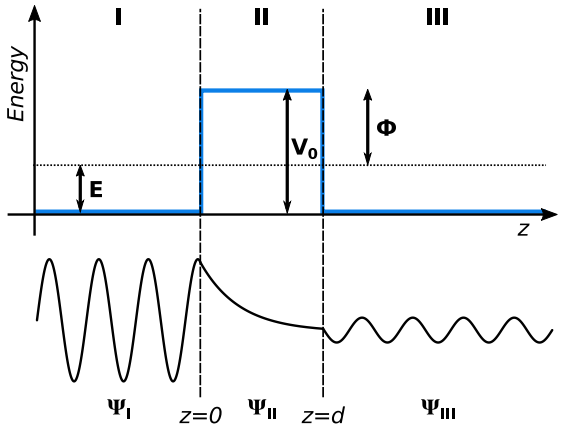

Figure 1.7: Quantum tunneling through a one-dimensional potential barrier. (Top) A particle with energy E is incident upon a potential barrier with height V_0. (Bottom) The wavefunction of the particle decays exponentially within the barrier region, and exists beyond the barrier despite the fact that $E < V_0$. This behaviour is classically forbidden.

where k is then given by,

$$k = \sqrt{\frac{2m}{\hbar^2}\left[E - V\left(z\right)\right]}. \tag{1.14}$$

Treating each region, I, II and III in Figure 1.7, individually, in regions I and III, $V = 0$, and thus the solution is an oscillating plane wave with $k = \sqrt{\left(2m/\hbar^2\right)E}$. Within the barrier, $V = V_0$ and thus k, as defined in Equation 1.14, is imaginary. Defining the variable κ by $k = i\kappa$,

$$\kappa = \sqrt{\frac{2m}{\hbar^2}\left(V_0 - E\right)}. \tag{1.15}$$

Consequently, within region II of Figure 1.7, with the initial ansatz for ψ as the equation of a plane wave, the wavefunction of the particle is $\psi = e^{-\kappa z}$. In classical mechanics, the particle would never be found in the barrier region when $E < V_0$. However, in quantum mechanics, the wavefunction exists within the barrier, where it decays exponentially as a function of distance, z, a process known as *tunneling*.

The general solution for the tunneling problem discussed above consists of linear combinations of left travelling and right travelling waves. The ansatz for the wavefunction, $\psi = e^{ikz}$, described a wave incident upon the barrier. Left travelling waves correspond to reflections off of the barrier into region I, and also off the potential drop between region II

and region III. Therefore, the full solution is given by,

$$\psi(z) = \begin{cases} Ae^{ikz} + Be^{-ikz} & z > 0, \text{ region I} \\ Ce^{-\kappa z} + De^{\kappa z} & 0 \leq z \leq d, \text{ region II} \\ Fe^{ikz} & z > d, \text{ region III.} \end{cases} \tag{1.16}$$

The coefficients, A, B, C, D and F can be solved by considering the boundary conditions at the region interfaces. The coefficient F gives the magnitude of the wavefunction beyond the barrier, and it can be shown that the absolute square of this coefficient is related to the flow of the tunneling electric current:

$$T = |F|^2 = \frac{4k^2\kappa^2}{\left(k^2 + \kappa^2\right)^2 \sinh^2(\kappa d) + 4k^2\kappa^2}, \tag{1.17}$$

where T is referred to as the transmission factor. In the regime where $\kappa d \gg 1$, Equation 1.17 can be simplified using the identity $\sinh^2 \kappa d \approx \frac{1}{4}e^{2\kappa d}$, giving,

$$T \propto e^{-2\kappa d}. \tag{1.18}$$

Therefore, the transmission factor is exponentially dependent on the width of the barrier, d.

The work function of a material, Φ, is defined as the amount of energy required for an electron to be removed from the surface of the material into the vacuum. If the vacuum reference energy is set as zero, then at $T = 0$, the Fermi energy is given by $E_F = -\Phi$. When two metal surfaces are in close proximity to each other but not touching, then a small voltage difference across the metals will induce the flow of a tunneling current, where, from Equation 1.18, we know that,

$$I \propto e^{-2\kappa z}. \tag{1.19}$$

From Equation 1.14, $k = \sqrt{2m/\hbar^2 \left[E - V(z)\right]} = \sqrt{2m\Phi/\hbar^2}$. In typical metals, $\Phi \sim 5$ eV and thus $2k \approx 1$ Å^{-1}. Therefore, for each increase in distance z by 1 Å, the tunneling current decreases by an order of magnitude. It is this relationship that enables the scanning tunneling microscope to provide atomic resolution: because of the exponential dependence of I on the distance z, changes in the tunneling current will correspond to changes in distance on the order of the atomic scale.

Density of states

When discussing the magnitude of tunneling current measured in the STM it is useful to consider the concept of the density of states. The density of states is defined as the number

of electronic states in a system within the range $(E, E+dE)$, and can be expressed by,

$$dN\left(E, E+dE\right) = \rho\left(E\right) dE. \tag{1.20}$$

The number of states within a finite energy range can then be counted using this definition,

$$N\left(E_{bottom}, E_{top}\right) = \int_{E_{bottom}}^{E_{top}} \rho\left(E\right) dE = \int_{E_{bottom}}^{E_{top}} \sum_{n} \delta\left(E - E_n\right) dE, \tag{1.21}$$

where the Dirac delta function δ was used to enumerate over all states n with $E_n \in [E_{bottom}, E_{top}]$. Given the spatial nature of STM imaging, it is useful to normalize the density of states by weighting the quantity based on the probability of a particle to be at position $\boldsymbol{r}$, given by $|\psi\left(\boldsymbol{r}\right)|^2$:

$$\rho\left(E, \boldsymbol{r}\right) = \sum_{n} |\psi_n\left(\boldsymbol{r}\right)|^2 \delta\left(E - E_n\right). \tag{1.22}$$

This normalized distribution is known as the local density of states (LDOS).

Tunneling current in STM

Different modifications can be made to the basic toy problem discussed above to determine a quantitative understanding of quantum tunneling in the context of STM. The details of these modifications are not strictly necessary for the reader to follow the rest of this thesis, but we present some of the main concepts here to provide a more complete picture of the STM experiment. Bardeen examined tunneling within the context of metal-insulator-metal junctions [50], but his model can be transferred to the STM problem. Using his approach, the tip-plus-barrier system and sample-plus-barrier system are treated as separate components to be solved independently, and then scattering from the tip states to the sample states is evaluated within time-dependent perturbation theory. The tunneling current is found to be,

$$I = \frac{4\pi e}{\hbar} \int_{0}^{eV} \rho_{tip}\left(\epsilon - eV\right) \rho_{sample}\left(\epsilon\right) T\left(\epsilon, V, d\right) d\epsilon. \tag{1.23}$$

In Equation 1.23 the current represents a convolution of both the states in the sample and the states in the tip. Consequently, in order to obtain quantitative information about the electronic structure of the sample, the tip must be fully characterized. The integral runs over the bias window and the transmission factor depends on the energy of the tunneling electron, ϵ, the bias voltage, V, and the width of the tunneling barrier. Figure 1.8a illustrates the effect of the bias voltage on the barrier potential, and the resulting modification

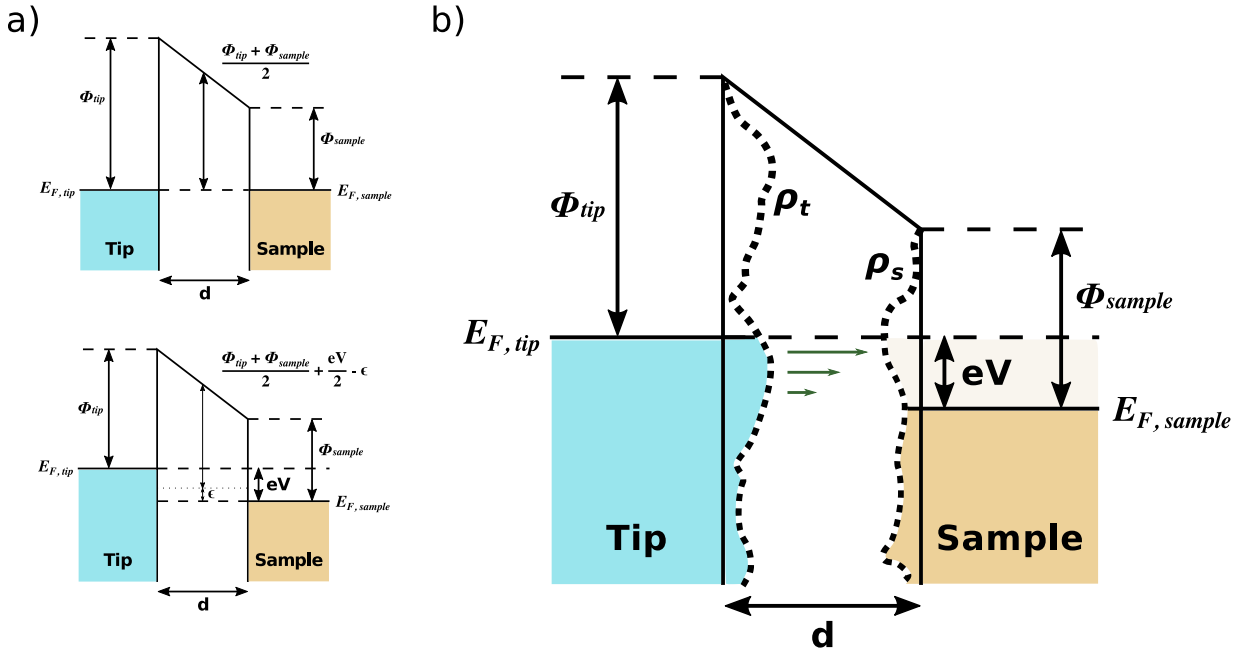

Figure 1.8: (a) The effect of a bias voltage on the potential barrier and on the relative energies of the occupied and unoccupied states of both the tip and the sample. (b) A schematic demonstrating most of the characteristics of quantum tunneling in the context of STM.

of the transmission factor. For an electron with energy ϵ, an effective barrier Φ_{eff} can be defined,

$$\Phi_{eff} = \frac{\Phi_{tip} + \Phi_{sample}}{2} + \frac{eV}{2} - \epsilon. \tag{1.24}$$

Incorporating this effective barrier height into the equation for the transmission factor gives,

$$T(\epsilon, V, d) \propto \exp\left[-2d\sqrt{\frac{2m}{\hbar^2}\left(\frac{\Phi_{tip} + \Phi_{sample}}{2} + \frac{eV}{2} - \epsilon\right)}\right]. \tag{1.25}$$

Figure 1.8b incorporates many of the components of Equation 1.25 and presents a more complete picture of the tunneling problem in STM. The block energy diagram on the left corresponds to the density of states of the tip, ρ_t, while that on the right represents the density of states of the sample ρ_s. As depicted, the density of states of both the tip and the sample are not constant but vary with energy. As a bias voltage is applied, the sample states are shifted by eV. Elastic tunneling occurs between occupied states in the tip and

unoccupied states in the sample. The magnitude of the tunneling current is dependent on the transmission factor, represented by the horizontal green arrows, with states close to E_F having a larger transmission factor compared to states far from E_F (Equation 1.18). The shape of the potential barrier is determined by the work functions of the tip and the sample, and by the applied bias.

The transmission factor depends not only upon the width of the barrier, but also on the magnitude of the bias voltage and the energy of the tunneling electrons. If the bias voltage is sufficiently small, $eV \ll \Phi$, the energy dependence of the transmission factor can be replaced by a constant average energy, $\bar{\epsilon} = E_{F,tip} + E_{F,sample}/2 = eV/2$, and thus in Equation 1.23, T can be moved outside of the integral. Furthermore, if the density of states of the tip is assumed to be constant, then ρ_{tip} can also be moved in front of the integral, leaving the tunneling current proportional to the voltage V and the density of states of the sample. Consequently, when low bias voltages are used, the tunneling current measured in STM is considered to be a probe of the surface density of states.

Constant current mode

The most common mode of STM operation, and the mode utilized throughout the thesis, is the constant current mode. During STM imaging a bias voltage is applied to a metallic tip relative to the sample being studied, and the tip is rastered across the surface of the sample as the tunneling current is measured (Figure 1.9a). The movement of the tip is facilitated by applying control voltages to a piezoelectric crystal on which the tip is mounted. In the constant current experiment, a current setpoint is fixed and a feedback loop is engaged in order to maintain the measured tunneling current at the setpoint by continuously adjusting the height of the tip as it is rastered. The experiment begins by approaching the sample with the biased tip until a tunneling current is detected, typically when the tip is within a few Ångstroms of the surface. For a homogeneous metallic system, the LDOS is expected to oscillate with the periodicity of the underlying atomic lattice. Due to the oscillating LDOS, engaging the feedback loop will result in the oscillatory motion of the tip at the same periodicity of the lattice in order to maintain the tunneling current setpoint. In this fashion, information about the LDOS is translated into topographic data. A schematic of this procedure is outlined in Figure 1.9b.[7]

[7]The schematic in Figure 1.9b includes a scan taken of the Si (111) (2×1) reconstruction. For information pertaining to this sample and the experimental technique used to prepare it, see Appendix B.

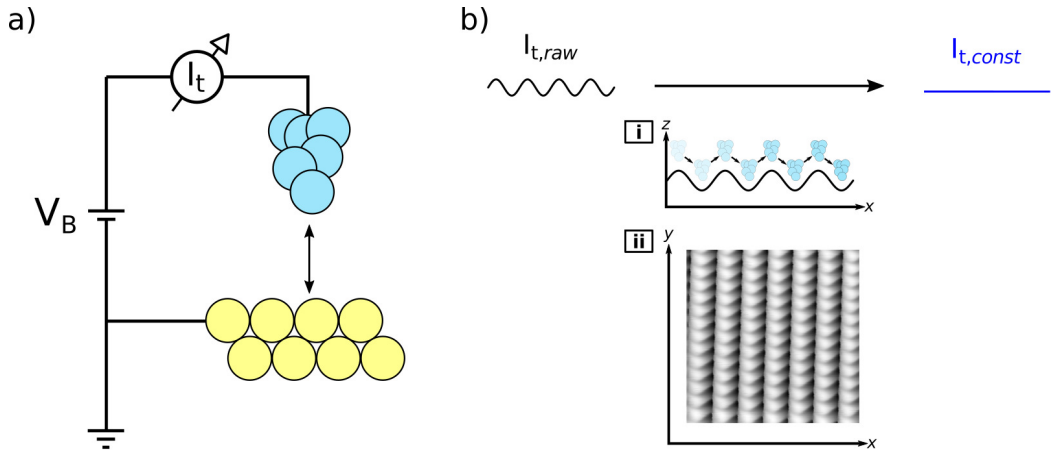

Figure 1.9: (a) A schematic of the circuit diagram for the measurement of the tunneling current. The bias is applied between the tip and the sample. (b) The constant current mode of operation in STM. Based on the measurement of the raw tunneling current, the height of the tip is adjusted in order that the current is fixed at a constant value. In this fashion, the current is translated into topographic information, as illustrated for one and two dimensions in (i) and (ii). (ii) presents an STM scan taken of the Si (111) (2×1) reconstruction.

Chapter 2

Scanning tunneling microscopy of 1 T−TaS_2

2.1 Introduction

Since its development in 1982 [51], scanning tunneling microscopy (STM) has proven to be an invaluable tool for probing the electronic structure of conductive materials. The formation of a charge density wave (CDW) in a compound has a profound effect on both the molecular structure and the electronic spectrum of the system. Therefore, STM, in combination with other structural probes such as x-ray diffraction (XRD) and transmission electron microscopy (TEM), enables a full structural characterization of the CDW phases of many different compounds.

STM has been particularly useful in clarifying the nature of the CDW phases in 1T-TaS_2. For example, the domain-like structure observed in the nearly commensurate phase was only clarified through STM experiments. While the basic structural properties of the phase could be determined by both TEM and XRD, both the symmetries and the amplitude of the modulation envelope that exists on top of the CDW phase could only be observed by a technique that probed the electronic structure with nanoscopic resolution. Furthermore, through scanning tunneling spectroscopy (STS) experiments, which allow for both energy and spatial resolution, the density of states within topological features present in the different phases could be measured. These experiments provided an understanding as to the role of domain walls in determining the conductivity of the different phases.

In this chapter we present STM data of the bulk equilibrium phases of 1T-TaS_2, specifically focussing on the nearly commensurate (NC) and commensurate (C) phases. Starting

with a description of the different phases in the context of Ginzburg-Landau theory, we then discuss the differences between the two states, and how these differences manifest themselves in STM images. Through analyzing the STM images of the bulk phases, we introduce the reader to the techniques utilized throughout this thesis for interpreting STM data. After describing how the bulk equilibrium phases appear in STM, we shift our focus to experiments on ultrathin flakes of 1T-TaS_2. We introduce the challenges associated with imaging exfoliated ultrathin flakes of 1T-TaS_2 and then conclude the chapter with a description of a device design that facilitates the measurement of both STM topography and the electrical properties of a sample *in situ*.

2.2 Charge ordering in 1 T$-TaS_2$

The phase diagram of 1 T$-TaS_2$ comprises multiple CDW phases, each possessing characteristic charge ordering in real-space. In the previous chapter of this thesis, we introduced the different CDW phases of 1T-TaS_2, describing the nature and origin of both the lattice distortion and the charge modulation. In this section, we describe the features of the equilibrium CDW phases in more detail, focusing on how these features are observed using STM. In particular, we provide a more complete description of the commensurate (C) and nearly commensurate (NC) phases using the notation and framework established by the Ginzburg-Landau theory of CDWs.

2.2.1 Ginzburg-Landau theory and charge density wave phase transitions

In 1975, McMillan applied the phenomenological Ginzburg-Landau (GL) theory to the study of phase transitions in CDW materials [52]. After writing a Landau free energy describing the system, this seminal work explored the incommensurate (IC)-commensurate (C) phase transitions observed in both the 1T and 2H polytypes of the Ta dichalcogenides. The theory was applied for different potential CDW configurations, including a single incommensurate CDW, a single commensurate CDW, and triple CDWs of both types. This description of the different CDW phases did not include the effect of higher order harmonic modes in the charge density, which were subsequently taken into account for triple CDWs by Nakanishi and Shiba [53, 54]. Only after including higher order harmonics was the free energy minimum corresponding to the NC phase recovered, and the IC-C phase transition in the Ta dichalcogenides correctly predicted to be first-order as opposed to second-order.

To describe the CDW phase transitions in 1T-TaS_2 an appropriate order parameter is the charge density of the conduction electrons. The GL free energy is written as an expansion of powers of this order parameter,[1]

$$F = \int d^2r \Big[a(\boldsymbol{r})\,\alpha^2(\boldsymbol{r}) - b(\boldsymbol{r})\,\alpha^3(\boldsymbol{r}) + c(\boldsymbol{r})\,\alpha^4(\boldsymbol{r}) + d(\boldsymbol{r}) \left(|\psi_1(\boldsymbol{r})\,\psi_2(\boldsymbol{r})|^2 + |\psi_2(\boldsymbol{r})\,\psi_3(\boldsymbol{r})|^2 + |\psi_3(\boldsymbol{r})\,\psi_1(\boldsymbol{r})|^2 \right) + \sum_{i=1,2,3} \psi_i^*(\boldsymbol{r})\, e_i(-i\boldsymbol{\nabla})\, \psi_i(\boldsymbol{r}) \Big], \quad (2.1)$$

where the coefficients $a(\boldsymbol{r})$, $b(\boldsymbol{r})$, $c(\boldsymbol{r})$, and $d(\boldsymbol{r})$ have the same periodicity of the lattice and thus can be written as

$$c(\boldsymbol{r}) = c_0 + c_1 \sum_i \mathrm{e}^{\mathrm{i}\boldsymbol{G}_i\cdot\boldsymbol{r}}. \quad (2.2)$$

It is assumed that only $a(\boldsymbol{r})$ has a temperature dependence. The order parameter used in the above expression, $\alpha(\boldsymbol{r})$, consists of a sum of three complex order parameters, $\psi_{1,2,3}$, the three components of the triple CDW,

$$\alpha(\boldsymbol{r}) = \mathrm{Re}\left[\psi_1(\boldsymbol{r}) + \psi_2(\boldsymbol{r}) + \psi_3(\boldsymbol{r})\right]. \quad (2.3)$$

This composite order parameter is related to the charge density of the system by:

$$\rho(\boldsymbol{r}) = \rho_0(\boldsymbol{r})\left[1 + \alpha(\boldsymbol{r})\right],^2 \quad (2.4)$$

where $\rho_0(\boldsymbol{r})$ represents the unmodulated density. In solving the integral in Equation 2.1, it is convenient to express the order parameters, $\psi_i(\boldsymbol{r})$, as:

$$\psi_i(\boldsymbol{r}) = \phi_i(\boldsymbol{r})\,\mathrm{e}^{\boldsymbol{Q^{(i)}}\cdot\boldsymbol{r}}. \quad (2.5)$$

In this expression, any superstructure present in the CDW is captured by the modulation envelope $\phi_i(\boldsymbol{r})$, while the phase and orientation of the CDW is given by the exponential term. For the case where a CDW phase has a constant amplitude, $\phi_i(\boldsymbol{r})$ does not vary spatially, giving

$$\psi_i(\boldsymbol{r}) = \phi_0 \mathrm{e}^{\boldsymbol{Q^{(i)}}\cdot\boldsymbol{r}}. \quad (2.6)$$

[1] In this chapter we will only consider the free energy within a single layer of the material. For a treatment of interlayer coupling see, for example, [55].

[2] Note the similarity between Equation 2.4 and Equation 1.1 in Chapter 1 of this thesis.

In Landau theory, the free energy is minimized for the order parameters $\psi_i(\boldsymbol{r})$ to determine the equilibrium phases. A simple illustrative example from McMillan is given in the footnote below to demonstrate the mechanics of the theory.[3] We refer the reader to the original works by McMillan and Nakanishi and Shiba for more detailed derivations of the application of GL theory to the determination of equilibrium CDW phases in the layered Ta dichalcogenides. However, in subsequent sections we discuss some of the consequences of these works, with an emphasis on the information that can be gleaned by drawing the connection between some of the details of the theory and what is observed in the STM of CDW materials.

2.2.2 The commensurate phase

In a commensurate CDW, the wave vectors of the charge modulation can be expressed as integer multiples of the underlying atomic lattice vectors:

$$\mu \boldsymbol{Q}_C^{(i)} - \nu \boldsymbol{Q}_C^{(i+1)} = \boldsymbol{G_i}\,(i = 1, 2, 3)\,, \tag{2.11}$$

for a triple CDW. The above equation is written in reciprocal space: $\boldsymbol{Q}_C^{(i)}\,(i = 1, 2, 3)$ is the ith component of the reciprocal CDW wave vector, $\boldsymbol{G_i}$ are the reciprocal atomic lattice

[3] We present the minimization for the transition from a normal state to a single incommensurate CDW. For an incommensurate CDW the order parameters defined in Equation 2.5 become,

$$\psi_1(\boldsymbol{r}) = \phi_0 \mathrm{e}^{\boldsymbol{Q}_I^{(1)} \cdot \boldsymbol{r}}, \psi_2 = \psi_3 = 0. \tag{2.7}$$

The free energy defined in Equation 2.1 is integrated over a plane of unit area giving,

$$F = \frac{1}{2} a_0 \phi_0^2 + \frac{3}{8} c_0 \phi_0^4. \tag{2.8}$$

The minima of this equation correspond to,

$$\phi_0 = \begin{cases} 0 & T > T^\star, \ \textit{the normal state} \\ (-2a_0/3c_0)^{1/2} & T < T^\star, \ \textit{the incommensurate state.} \end{cases} \tag{2.9}$$

where the transition temperature is defined to be $T^\star$. With the above dependency of the order parameter on temperature, the transition from a normal state to a single incommensurate CDW is found to be second order, and the free energy in the incommensurate phase is calculated as,

$$F = \frac{1}{2} a_0 \phi_{0,I}^2 + \frac{3}{8} c_0 \phi_{0,I}^4 = \frac{-a_0^2}{6c_0}. \tag{2.10}$$

This simple example demonstrates the utility of Ginzburg-Landau theory in predicting the temperatures, free energies, and orders of different CDW phase transitions.

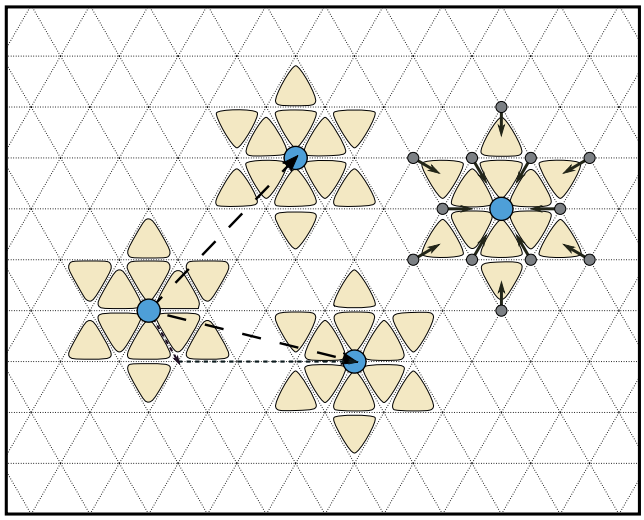

Figure 2.1: Characteristic features of the CDW in 1T-TaS_2. The periodic lattice distortion accompanying the charge modulation forms a star-shaped cluster, as indicated by the grey vectors in the rightmost pattern. The dotted and dashed vectors illustrate the commensurability condition for 1T-TaS_2 and the resulting CDW wave vectors, respectively.

vectors, and μ and ν are integers. In 1T-TaS_2, a commensurate CDW phase is observed satisfying the commensurability condition in Equation 2.11 with $\mu = 3$ and $\nu = 1$. In this phase, the CDW wave vector is not aligned with the atomic lattice wave vector but is rotated at an angle of 13.9° relative to the underlying lattice, and the magnitude of the CDW wavelength is equal to $\sqrt{13}a$, where a is the magnitude of the atomic lattice vector:

$$|\boldsymbol{Q}_{\boldsymbol{C}}^{(i)}| = \boldsymbol{G_i}/\sqrt{\mu^2 + \mu\nu + \nu^2}. \tag{2.12}$$

Figure 2.1 illustrates many of the observed features in real-space of the commensurate CDW in $1\,\mathrm{T}{-}TaS_2$. The underlying, hexagonal lattice corresponds to the network of Ta atoms in a single layer of the material. The star pattern overlaid on the lattice illustrates the lattice distortion that accompanies the commensurate CDW formation. This distortion was previously discussed in Section 1.2.2 of this thesis. The orientation of the specific distortion vectors for each atom are given in grey in the rightmost pattern. The maximum of the CDW is indicated by the blue circles at the centre of each star. In STM images of all of the equilibrium phases of $1\,\mathrm{T}{-}TaS_2$, it is the symmetry associated with these star-shaped clusters that is reflected in the features with the largest amplitude (Figure 2.2). The commensurability condition satisfied in 1T-TaS_2 and the resulting CDW wave vectors are represented in Figure 2.1 by the dotted and dashed vectors respectively.

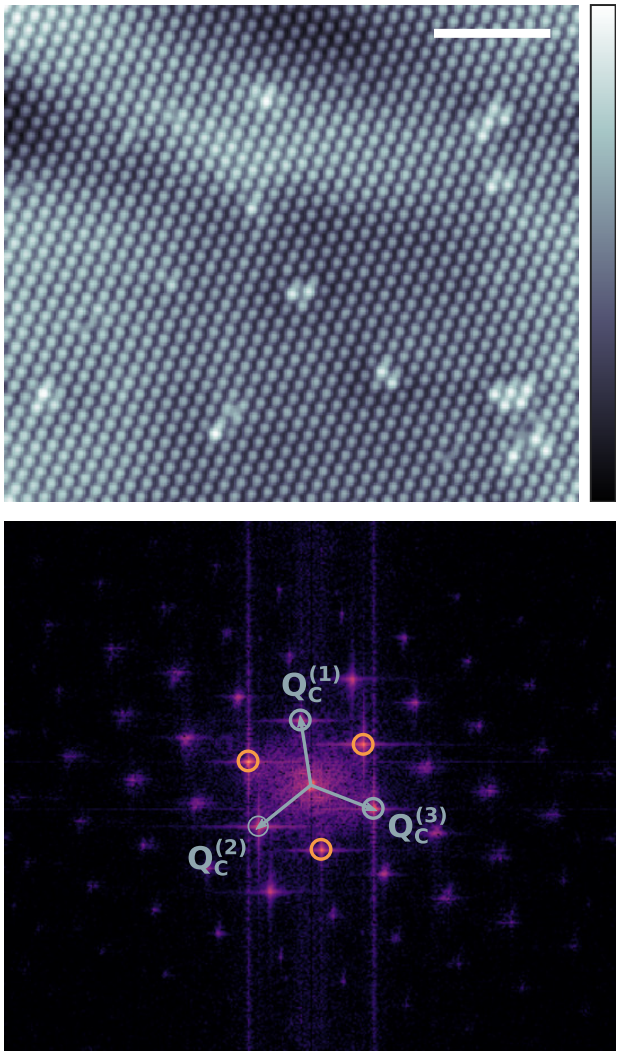

Figure 2.2: The C CDW phase in bulk 1 T−TaS_2 taken at 77 K. The FFT of the scan is also given. The peaks circled in grey correspond to the fundamental CDW modes, while those circled in orange correspond to the negative Fourier components of the fundamental modes. Scale bar = 7 nm, $V_t = 0.57$ V, $I_{set} = 0.19$ nA.

The relation between the wave vectors of the commensurate CDW and the reciprocal lattice wave vectors is clearly evident in a fast Fourier Transform (FFT) of an STM image of the commensurate phase that resolves the atomic lattice in addition to the charge modulation.[4] Figure 2.3 presents an STM scan of the C phase in 1T-TaS_2 with atomic resolution. In this particular scan, the tip is irregular, distorting the appearance of the CDW maximum (Section 2.3.1). The reciprocal CDW wave vectors and the reciprocal lattice vectors are labelled in blue and red respectively in the FFT given in Figure 2.3b. The commensurability condition is directly represented in the FFT: for example, one can see that $\boldsymbol{G_2} = 3\boldsymbol{Q_C^{(2)}} - \boldsymbol{Q_C^{(3)}}$.

Discommensurations are observed in both the C and NC phases of 1T-TaS_2 and play an

[4]The Fourier transform (FT) is an effective technique for analyzing periodic information that converts temporal or spatial data into an equivalent representation in the frequency domain. While a detailed treatment of the FT is not required given the scope of this thesis, we introduce some of the basic concepts to facilitate an understanding of the FTs presented in this work. Throughout this thesis, fast Fourier transforms (FFTs) will be used to analyze and discuss a variety of STM images.

The FFT is an algorithm that implements the discrete Fourier transform (DFT) efficiently. A DFT will produce of series of N complex numbers, X_k, from a series of N equally spaced samples of a function, $\{x_0, x_1, \cdots, x_{N-1}\}$,

$$X_k = \sum_{n=0}^{N-1} x_n \mathrm{e}^{-i2\pi kn/N}, k = 0, 1, \cdots, N-1. \tag{2.13}$$

The inverse transformation is given by,

$$x_n = \frac{1}{N} \sum_{k=0}^{N-1} X_k \mathrm{e}^{i2\pi kn/N}. \tag{2.14}$$

Comparing this transformation with that corresponding to the continuous complex Fourier series,

$$x\left(t\right) = \int_{-\infty}^{\infty} c_n \mathrm{e}^{in\omega_0 t}, \tag{2.15}$$

one can see that the DFT represents a discretization of the continuous transform into N equally spaced bins in the interval $[0, 2\pi)$, each bin separated by the angle $(\omega_0 t) = 2\pi \frac{k}{N}$.

The STM measures variations in the electronic structure of a material in real-space. A FT of a function in space transforms the data into reciprocal space. Most of the samples measured in this thesis possess a hexagonal lattice. The reciprocal lattice of a hexagonal lattice is also hexagonal, rotated by 60° from the original lattice basis vectors. Consequently, the FFT of a hexagonal lattice will produce a hexagonal pattern (see, for example, Figure 2.2). By interconverting between the amplitudes in the FFT and the real-space domain one can calculate the wave vectors of the lattice represented by the FFT. Interconversion between the FFT domain and real-space requires knowledge of parameters related to the image resolution (i.e. the number of data points taken for each row and each column).

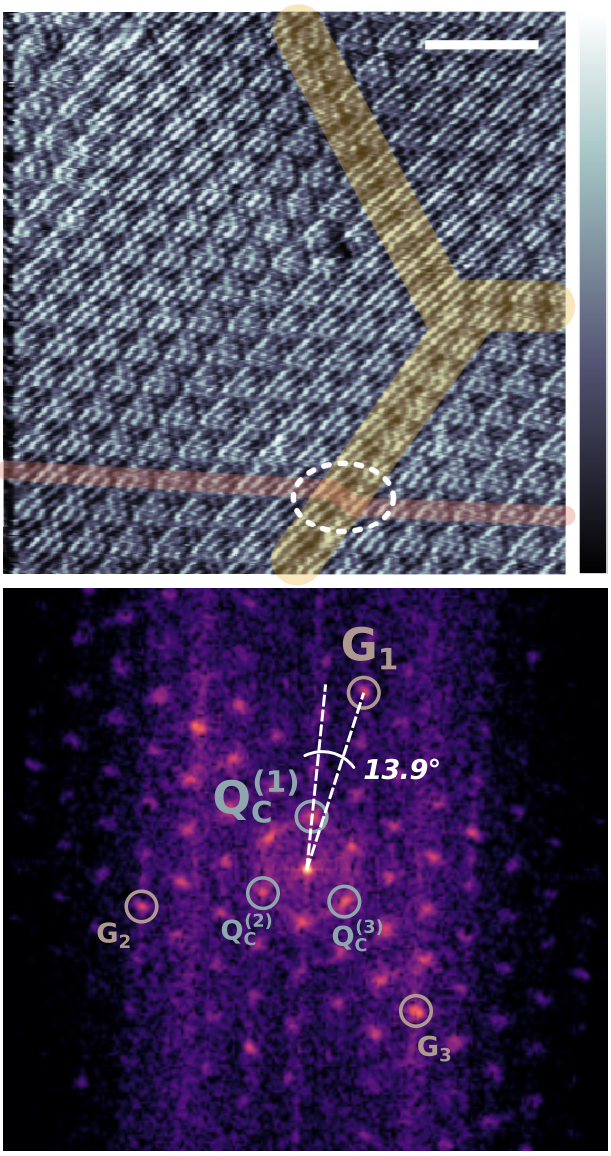

Figure 2.3: The C CDW phase in bulk 1 T−TaS_2 with atomic resolution, taken at 77 K with a PtIr tip. In this particular scan the tip is asymmetric, giving a distorted appearance to the CDW maxima (see Section 2.3.1). The FFT of the STM scan is also given. Scale bar = 3.3 nm, $V_t = -1.00$ V, $I_{set} = 0.60$ nA.

important role in determining the bulk electrical properties of each state [56–58].[5] In both phases, the discommensurations consist of a phase slip along at least one of the components of the CDW; at the discommensuration the CDW is offset by an atomic lattice vector. Such a topological defect is observed in Figure 2.3 and is highlighted in yellow. The phase slip is most easily seen by looking along a line of CDW maxima, as highlighted in red. When the line hits the discommensuration, the maxima of the CDW shift. Furthermore, within the discommensurations the amplitude of the CDW is less than what is seen throughout the rest of the phase. While the discommensurations in both phases are superficially similar, electronically the local density of states (LDOS) within these features differ substantially, as revealed by STS experiments [56, 57]. In the C phase, electron correlations result in a gap in the LDOS localized at the center of the discommensurations. On the other hand, in the more conductive NC phase, it is believed that the discommensurations themselves contain the charge carrying states.

2.2.3 The nearly commensurate phase

McMillan's seminal work describing the triple CDW found in 1T-TaS_2 correctly predicted the ground state commensurate CDW phase, but found the IC-C phase transition to be second-order. This result contradicted the existing experimental evidence that indicated the transition was in first-order in nature. Nakanishi and Shiba, starting from the description of the CDW given by McMillan, incorporated harmonics that arise when the CDW wave vectors are nearly commensurate but do not perfectly satisfy the commensurability condition. With the inclusion of these harmonics, the theory correctly predicts both the equilibrium NC CDW phase and the correct order for the IC-C phase transition.

When the wave vector of the CDW phase is incommensurate with the underlying lattice but still close to the commensurate wave vector, then higher order harmonics are induced by the fundamental mode. Rewriting Equation 2.5, one can expand the modulation function $\phi(\boldsymbol{r})$ in terms of the difference vectors $\boldsymbol{q}^{(i)} = \boldsymbol{Q}^{(i)} - \boldsymbol{Q}_C^{(i)}$ (Figure 2.4a),

$$\phi(\boldsymbol{r}) \propto \mathrm{e}^{\boldsymbol{q}^{(i)} \cdot \boldsymbol{r}}. \tag{2.16}$$

These harmonics form a hexagonal lattice themselves, with the lattice points written as

$$\boldsymbol{q}_{lmn}^{(i)} = l\boldsymbol{k}^{(i)} + m\boldsymbol{k}^{(i+1)} + n\boldsymbol{k}^{(i+2)} + \boldsymbol{q}^{(i)}, \tag{2.17}$$

[5] Regarding terminology, throughout this thesis "discommensurations" and "domain walls" will generally be used interchangeably, though when describing the C phase we will exclusively refer to these features as discommensurations.

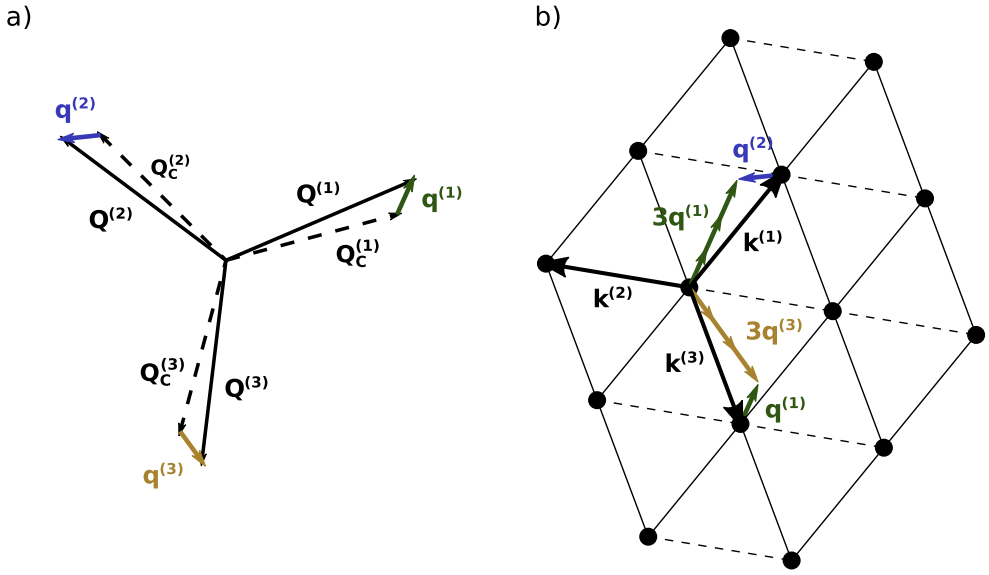

Figure 2.4: Relations between the wave vectors of an arbitrary CDW phase. (a) The displacement vectors are defined as the difference between the measured fundamental CDW wave vector and the expected fundamental wave vector of the commensurate state. (b) Harmonics arise when the CDW wave vector is nearly commensurate that result in the appearance of domains. These modes can be defined using $q^{(i)}$ and form a regular lattice.

where $\boldsymbol{k}^{(i)} = 3\boldsymbol{q}^{(i)} - \boldsymbol{q}^{(i+1)}$, and $\boldsymbol{q}^{(i)}$ is defined as above (Figure 2.4c). Note that in the definition of $\boldsymbol{k}^{(i)}$, the linear coefficients for the difference vectors are equivalent to the factors in the commensurability condition for 1T-TaS_2 ($\mu = 3$, $\nu = 1$). The complete sequence of $\boldsymbol{k}^{(i)}$ and $\boldsymbol{q}^{(i)}_{lmn}$ $(i = 1, 2, 3)$ are generated with the cyclic replacement of the indices. Using this notation, a general CDW phase, as defined by the modulation function $\phi_i(\boldsymbol{r})$, is given by

$$\phi_i(\boldsymbol{r}) = \sum_{\substack{l,m,n\geq 0 \\ l\cdot m\cdot n=0}} \Delta^{(i)}_{lmn} \mathrm{e}^{i\boldsymbol{q}^{(i)}_{lmn}\cdot\boldsymbol{r}}. \tag{2.18}$$

The harmonics are indexed by the integers l, m, and n, and the point $\Delta^{(i)}_{000}$ corresponds to the fundamental wave vector of the ith component of the triple CDW. To determine the equilibrium phase of the system, i.e. the absolute minimum of the free energy, the non-linear coupled equations,

$$\frac{\partial F}{\partial \Delta^{(i)}_{lmn}} = 0, \tag{2.19}$$

are solved for different values of $\boldsymbol{q}^{(i)}$. By taking into account a suitably large number of harmonics, Nakanishi and Shiba corrected recovered the successive first-order phase transitions in 1T-TaS_2 and predicted the wave vector of the NC state as $\boldsymbol{Q}_{\boldsymbol{NC}}^{(\boldsymbol{i})} \simeq 0.248\boldsymbol{G}_{\boldsymbol{i}} - 0.060\boldsymbol{G}_{\boldsymbol{i+2}}$.

From the calculated modulation envelope, the NC phase is predicted to have a domain-like structure. Figure 2.5 presents an STM image of the NC CDW phase of 1T-TaS_2 measured on a bulk sample. The characteristic feature of the NC phase is the appearance of domains, arranged in an approximately hexagonal lattice. These domains result in a "textured" superstructure, as evident in the STM image given in Figure 2.5. The FFT of the STM image contains satellite peaks surrounding the fundamental modes of the CDW. These satellite peaks have a correspondence with the harmonics discussed above. The orientation of the satellite peaks relative to the fundamental wave vectors determines the size and symmetry of the domains.

Figure 2.6 presents an STM of the NC phase with atomic resolution. As discussed, in the NC phase, the CDW wave vectors do not satisfy commensurability; the magnitude and angle of the wave vectors are such that there does not exist a pair (μ, ν) such that $\mu\boldsymbol{Q}_{\boldsymbol{C}}^{(\boldsymbol{i})} - \nu\boldsymbol{Q}_{\boldsymbol{C}}^{(\boldsymbol{i+1})} = \boldsymbol{G}_{\boldsymbol{i}}\,(i = 1, 2, 3)$. The FFT of the STM image corroborates this result. Using the analysis pipeline described later in this thesis (Section 2.3), the magnitude of the CDW wave vector was measured to be 1.179 nm, in agreement with the value reported in the literature (1.173 ± 0.11 nm [59]). Furthermore, the angle of the CDW wave vector to the lattice wave vector was measured to be 12.3°, also in agreement with what is expected for the NC phase.

Chiral orientations of the commensurate phase

When 1T-TaS_2 undergoes a phase transition from the IC phase to the NC phase, two chiral orientations are possible. As discussed in Section 1.2.2, in the IC phase the CDW wave vector is oriented along the same direction as the atomic lattice wave vector, while in the NC phase, the CDW is rotated away from the atomic lattice at an angle that is dependent on the temperature of the system ($\sim 11° - 13°$). There are two possible chiral orientations, designated as α and β in the literature, corresponding to whether the CDW is rotated either clockwise or counterclockwise. Figure 2.7 schematically illustrates the two different chiral phases. In Figure 2.7a, the atomic and CDW lattice are pictured in reciprocal space, with the CDW lattice corresponding to the inner hexagon, and the atomic lattice represented by the outer hexagon. In the IC phase, the two lattices are aligned. When the CDW is oriented at an angle to the atomic lattice, two different chiral representations are possible,

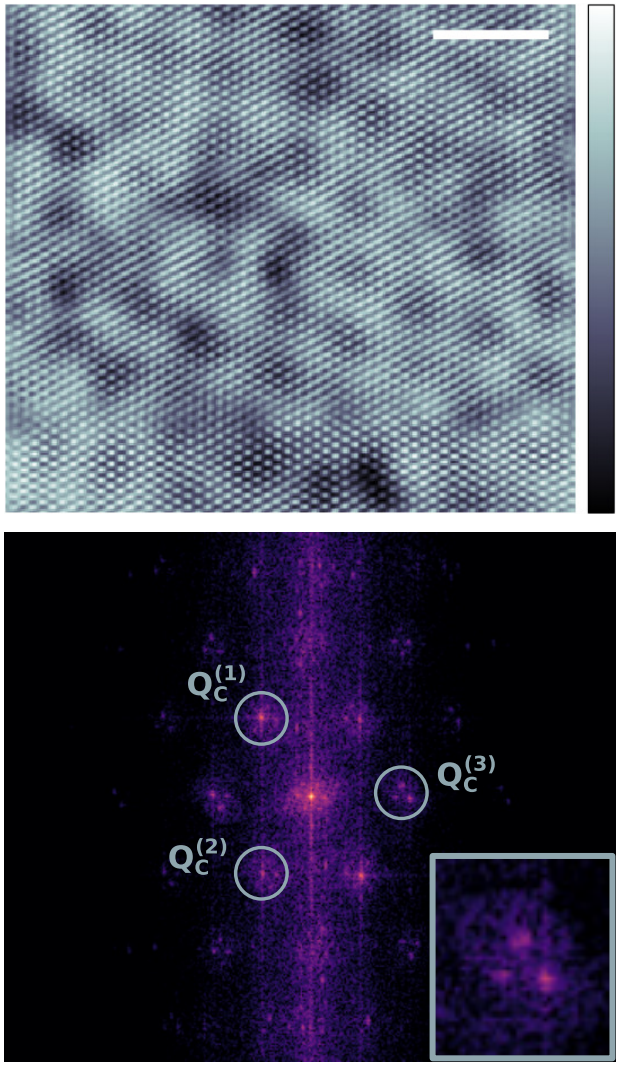

Figure 2.5: The NC CDW phase in bulk 1 T−TaS_2, taken at 240 K with a PtIr tip. The FFT of the scan is also given. Scale bar = 11 nm, $V_t = 5$ mV, $I_{set} = 1.50$ nA.

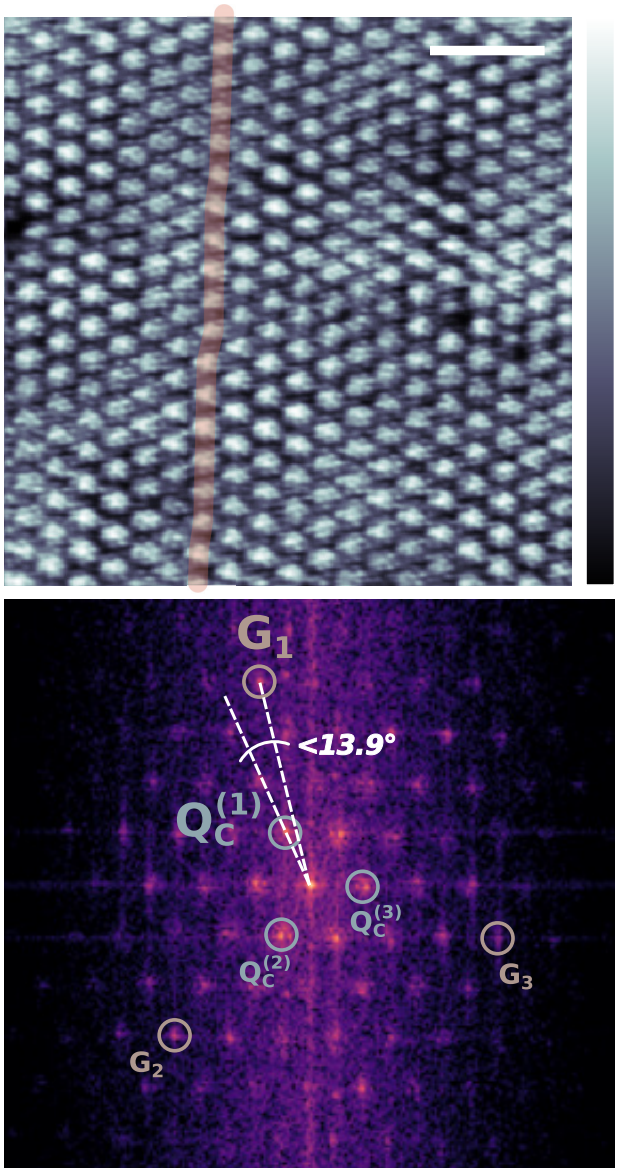

Figure 2.6: The NC CDW phase in bulk 1 T$-TaS_2$ with atomic resolution, taken at 240 K with a PtIr tip. The FFT of the scan is also given. Scale bar = 3.8 nm, V_t = 10 mV, I_{set} = 1.95 nA.

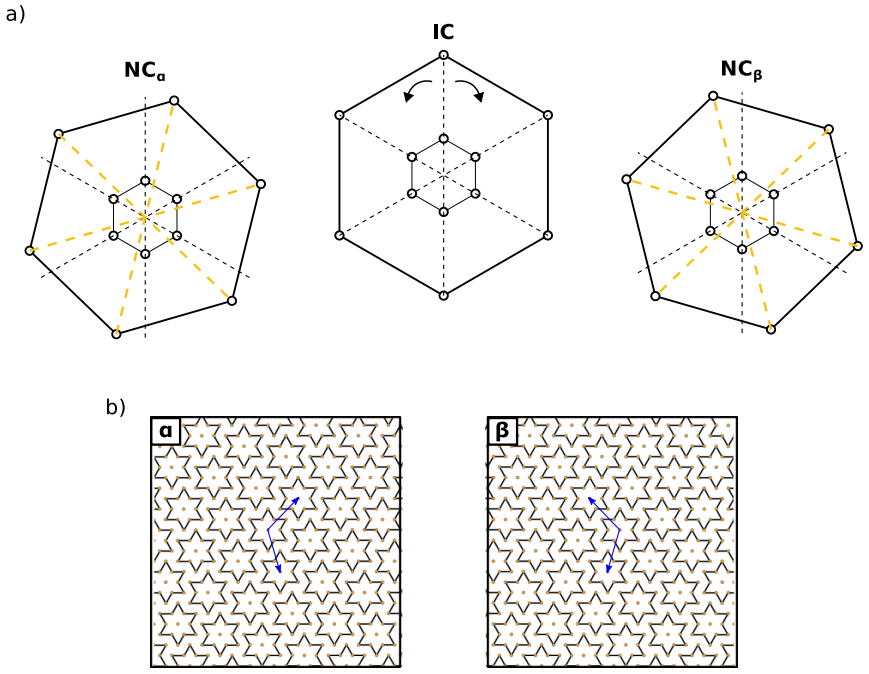

Figure 2.7: Chiral orientations in 1T-TaS_2. Starting from the IC phase, where the CDW components are aligned with the lattice vectors, there are two possible orientations of the NC and C phase depending on whether the CDW wave vector is rotated clockwise (β) or counterclockwise (α). In the top portion of the figure, the relation between the CDW and the atomic lattices are given in reciprocal space, while in the bottom, the two resulting CDW states are pictured.

as illustrated by the two distinct star cluster tiling (Figure 2.7b). Both chiral orientations are energetically equivalent, and have been previously observed to exist within the same sample [60, 61]. Furthermore, interconversion between the two different orientations has been shown via femtosecond laser pulses [60].

2.3 Analyzing STM images of a layered material

Qualitative analysis of STM images and their corresponding FFTs yield specific information related to the system. Symmetries present within the lattice, as well as certain characteristics of the phase being studied, such as the presence or absence of a domain superstructure, are readily determined from a qualitative analysis. For most of the discussion in this thesis, this level of analysis is sufficient, but occasionally quantitative details are required. In this section we discuss some additional techniques used to analyze STM images of layered materials.

Figure 2.8 presents a common analysis pipeline utilized throughout this thesis. In this pipeline, the following operations are performed: filtering, windowing, calibration and padding.

Filtering

Filtering is a helpful tool for removing certain artifacts from the image or for isolating certain components in the Fourier analysis. In the pipeline depicted, a low pass Butterworth filter is used to remove high frequency noise from the image. Given the diameter of the filter d, the value of the filter at the pixel (x, y) is defined as:

$$f\left((x,y)\right) = \frac{1}{1+\left(\frac{r}{d}\right)^{2n}}, \tag{2.20}$$

for some value of n, where r is the distance from the pixel (x, y) to the centre of the filter. This form of filter produces the mask depicted in Figure 2.9a.

Windowing

The discrete Fourier transfrom (DFT) assumes the input function is periodic. In the event the input is aperiodic, the DFT algorithm imposes periodic boundary conditions which

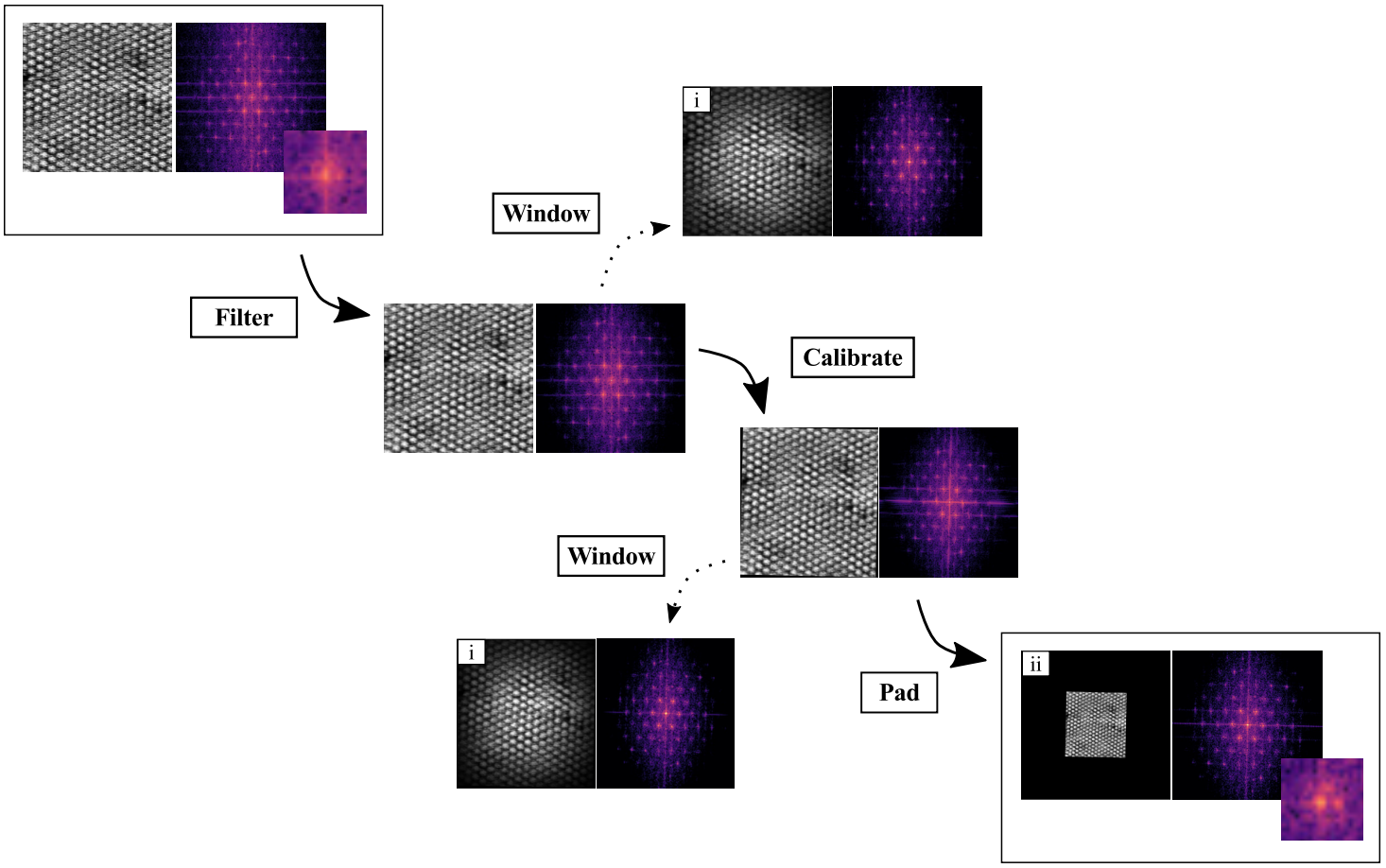

Figure 2.8: An example of a data analysis pipeline demonstrating the effects of the some of the tools used to analyze STM images. Filtering, windowing, and padding operations are demonstrated. The effects of applying an affine transformation to calibrate the STM scanner are given.

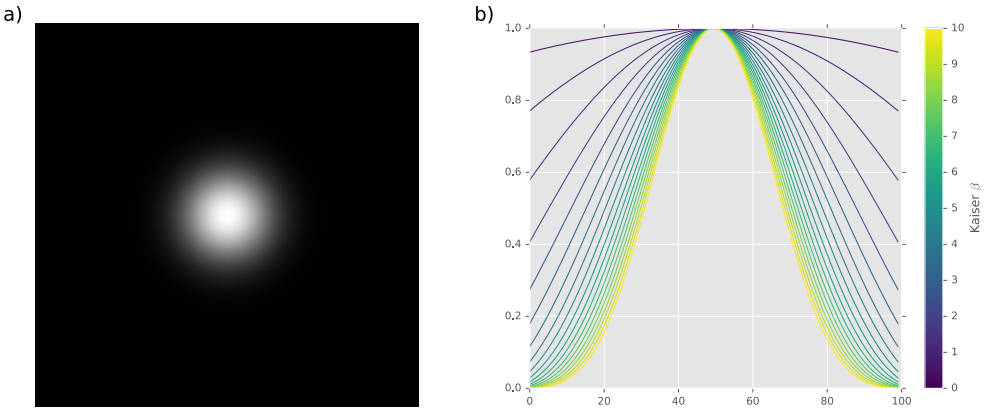

Figure 2.9: Tools for analysing the Fourier transform. (a) The Butterworth filter given by Equation 2.20. (b) The Kaiser windowing function defined for different values of β.

can result in discrete jumps in the input signal at the edges. These discontinuities give rise to artifacts that can obscure the desired information in the measured FFT. In order to remove these artifacts, a windowing function is used. The goal of the windowing function is to smoothly bring the value of the input signal to 0 at the edges, thus removing any discontinuities when the DFT is applied. A common windowing function is the Kaiser window, given by

$$w(n) = I_0\left(\beta\sqrt{1-\frac{4n^2}{(M-1)^2}}\right)/I_0(\beta), \tag{2.21}$$

where I_0 is the modified zeroth-order Bessel function and $-\frac{M-1}{2} \leq n \leq \frac{M-1}{2}$. A plot of the one-dimensional Kaiser window for different values of β is given in Figure 2.9a. As the value of β is increased the amplitude of the window goes to 0 at the edges. An example of the effect of applying the Kaiser window to an STM scan and the resulting improvements in the FFT is given in Figure 2.8 panel (i).

Calibration

There are numerous external parameters in STM experiments that can lead to a distortion in the measured image. Numerous techniques exist for both correcting for distortion in real-time as the data is being collected, and for removing the distortion during post-processing [62–65]. One of the simplest forms of calibration involves modifying an image by applying a transformation determined from scanning the lattice of a reference sample. Based upon

the deviation of the measured reference lattice constants from the known values in the literature, the required Affine transformation for correcting the scan is calculated.

In STM scans in this work where both the CDW superlattice and the underlying atomic lattice are resolved, the atomic lattice itself can be used as the reference standard. The distortions associated with CDW formation are sufficiently small compared to the atomic lattice parameters, that in images where the atomic lattice is resolved, one can use the lattice to find the transformation required to reproduce the expected wave vectors. After applying this transformation to the entire image, the CDW wave vectors can be accurately measured. In the event that the atomic lattice is not resolved, a transformation can be determined through a separate measurement of a reference sample such as highly oriented pyrolytic graphite (HOPG) or gold. This calibration amounts to correcting for linear asymmetries present in the experimental set up (for example, asymmetries in the STM scanner) when the measurements were conducted.

Padding

Ultimately, the resolution of the Fourier transform is given by the width of each bin in the DFT. In order to distinguish one peak from a second they need to be one bin apart. However, when determining the location of a single peak in the FFT, interpolation can be used to provide a more exact location of the maximum. This is accomplished during the transform itself by padding the signal with zeroes (see Figure 2.8 panel (ii)).

2.3.1 Image distortions

Amplitude and phase variations

When measuring layered materials with a lattice structure dominated by three Fourier components, an irregular tip can dramatically affect the appearance of the surface electronic state [65, 66]. A layered material with a hexagonal lattice can be viewed as the superposition of three sinusoidal waves oriented 120° apart, with the maxima in the lattice occurring at the intersections of the waves. When the tip is irregular, the convolution of the tip and the sample deviates from the simple three-fold structure observed in the ideal case. In the event the tip is doubled, the resulting STM image consists of the superposition of two scans of the surface with different phases and amplitudes. The image will still be dominated by three Fourier components, but unlike in the ideal case, the phases and amplitudes of the different Fourier modes can vary.

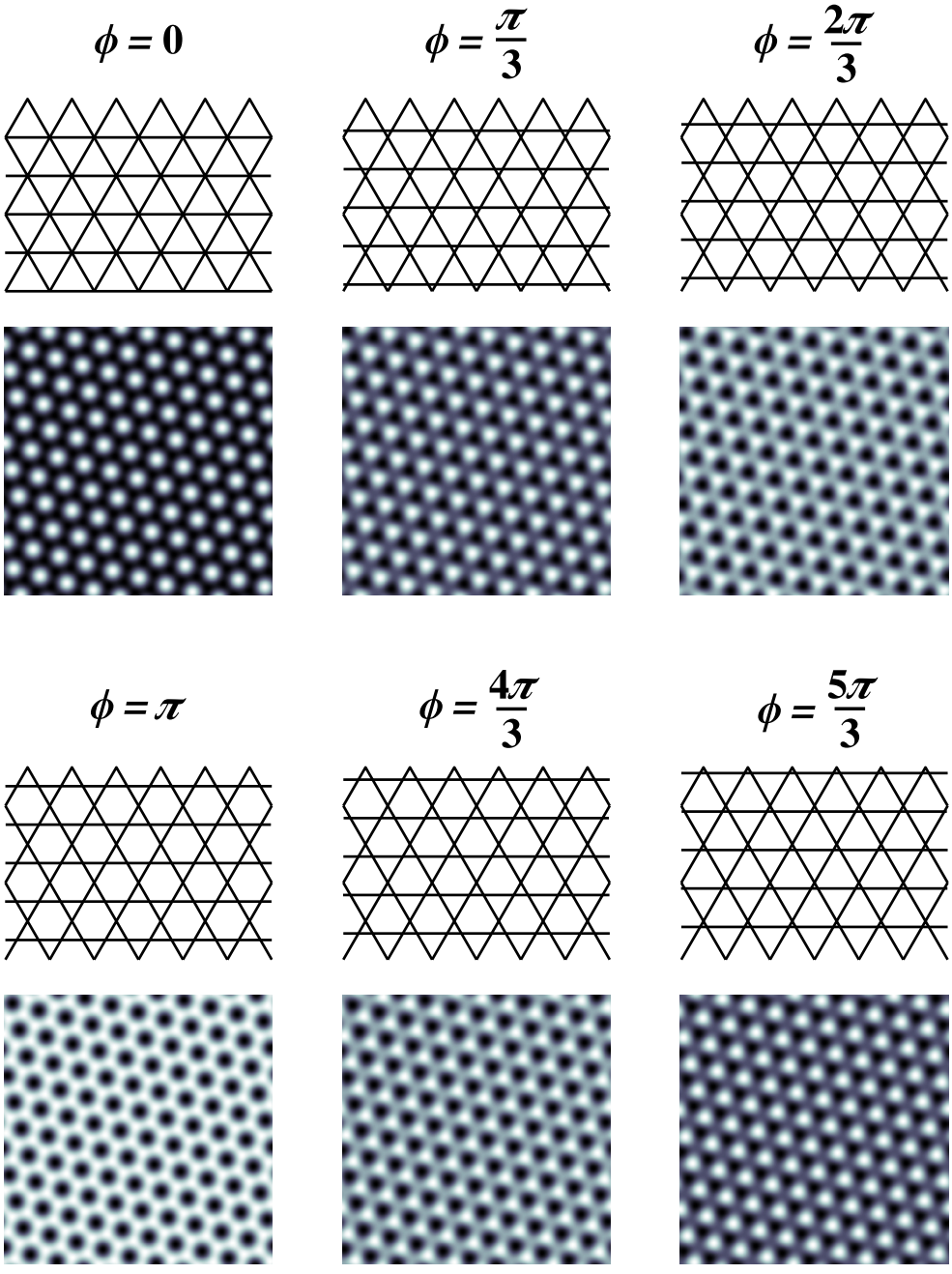

Figure 2.10: Phasing effects in systems with threefold symmetry.

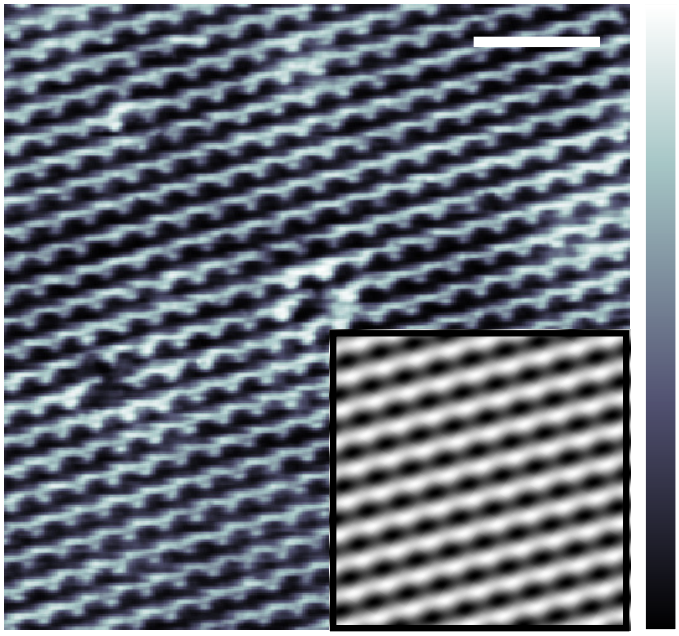

Figure 2.11: Amplitude variation that arises from an irregular tip. If one Fourier component has a larger amplitude compared to the other, the CDW lattice will be superimposed on lines oriented perpendicular to the norm of the wave front of the amplified Fourier mode. Scale bar = 4 nm, $V_t = -0.55$ V, $I_{set} = 0.27$ nA.

The effect described above is demonstrated in Figure 2.10. The lattice depicted consists of three sin waves oriented 120° apart. When all of the phases are equal, the resulting STM image consist of spherically symmetric maxima at the intersections of the waves. If we allow the phase of one of the waves to vary (in Figure 2.10 the phase of the wave with a horizontal wave front), the appearance of the lattice changes. Similarly, if the amplitude of one of the Fourier components is adjusted, the character of the resulting STM scan becomes more linear, oriented perpendicular to the wave vector of the dominant mode (Figure 2.11).

Thermal drift

In the Omicron LT-STM used throughout this thesis, there is a heater attached to the sample stage allowing for experiments to be conducted in a wide range of temperatures. When in measurement mode, the sample stage is not in strong thermal contact with the cryostat, and with the heating element turned on, there is a potential for the existence of thermal gradients. These gradients can cause a slight motion of the system components,

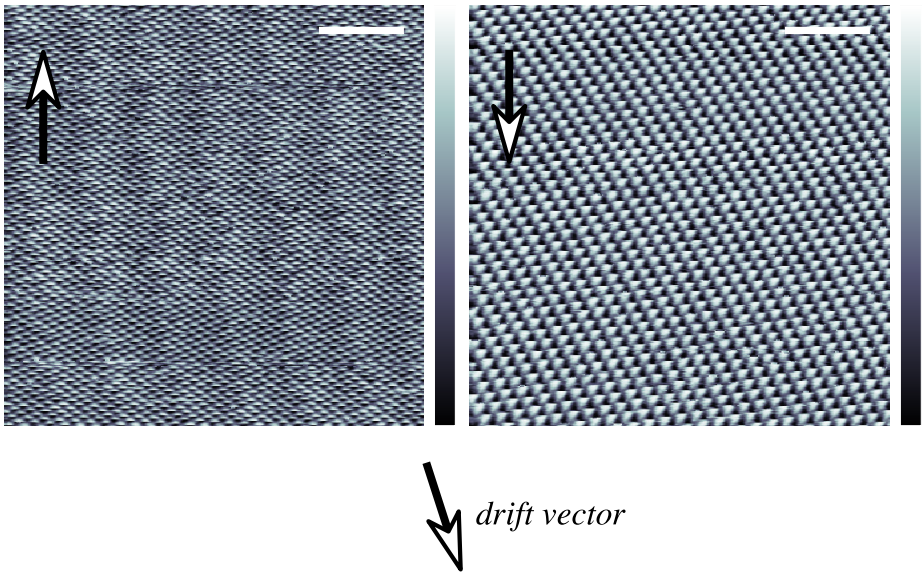

Figure 2.12: The effects of thermal drift. Scans will appear either compressed or elongated depending on the alignment of the scan direction relative to the thermal drift vector. The arrows overlaid on the images correspond to the scan directions. Scale bar = 1.25 nm, $V_t = -0.50$ V, $I_{set} = 0.05$ nA. These scans were taken with a PtIr tip at 190 K.

called thermal drift. Given that STM scans are being conducted at the nanoscale, this thermal drift will manifest itself as a distortion in the captured image. Scans are performed in both the up and down directions, and by comparing the two images one can approximate the direction of the thermal drift vector. When the scan direction is oriented along the same axis as the drift vector the lattice will appear elongated, while when the scan direction is opposite that of the vector, the lattice will be compressed. Figure 2.12 demonstrates this effect. Thermal drift can be corrected both in real-time and also through post-processing [62–64], but in most cases it is best to simply wait for the system to fully thermalize prior to conducting any experiments.

2.4 Scanning tunneling microscopy of 1 T$-TaS_2$ in the ultrathin limit

With an understanding of the features associated with the different bulk equilibrium phases of 1T-TaS_2, and how these features appear when imaged using STM, we now turn our

attention to examining flakes of this particular Ta dichalcogenide in the ultrathin limit. We define the ultrathin limit as flakes that are less than 10 nm thick ($\sim$ 20 TaS_2 layers). Imaging exfoliated flakes presents its own challenges that have been tackled in the literature in various ways. In this section we start by briefly commenting on the motivation for probing the properties of ultrathin 1T-TaS_2 and then survey some of the challenges observed in the literature for performing STM on exfoliated, ultrathin flakes. Lastly, we present a device design that facilitates both the imaging of an exfoliated flake and the measurement of the flake's bulk electrical properties *in situ*.

The characteristics of the charge ordering along the *c*-axis in 1T-TaS_2 (the axis perpendicular to the plane of the 2D sheets), have been studied both experimentally and using a modification of the GL theory introduced in Section 2.2.1 [23, 55, 67, 68]. It is found that in the low temperature phase, dimerization occurs, where within a given bilayer the CDW are stacked such that the maxima in each star cluster are aligned along the *c*-axis. The bilayers themselves stack in one of three possible orientations, randomly selected. In the NC phase, where the discommensurations form a hexagonal lattice, the three-dimensional unit cell is found to encompass thirteen layers of the material [55]. It is important to note that even in its most basic form, without including any interlayer interactions, GL theory predicts each of the different superstructures that define the bulk phases in 1T-TaS_2. While the theory fails to find distinctions between bulk phases and phases found in a monolayer of 1T-TaS_2, results exist that demonstrate the importance of considering the three-dimensional charge ordering [21, 22, 33, 69, 70]. Consequently, thinning 1T-TaS_2 towards the 2D limit is expected to modify the behaviours of the system and potentially alter its phase diagram.

2.4.1 Isolating and imaging van der Waals materials

Imaging exfoliated van der Waals materials using STM presents several challenges. The cleanliness of the sample is paramount to successful imaging, and the exfoliation procedure has the tendency to introduce contaminants to the surface of the material. Consequently, throughout the literature, the majority of the STM experiments on van der Waals materials have been conducted on samples that are capable of being cleaned. For example, graphene flakes can be successfully imaged following heating at 623 K for three hours under an argon and hydrogen atmosphere [71], a process that can be accomplished in a standard preparation chamber connected to an STM in ultrahigh vacuum.

The condition of the surface also deteriorates if the sample is air sensitive. 1T-TaS_2 is known to oxidize when exposed to atmosphere. Consequently, a sample that has been

fabricated in ambient conditions is impossible to STM successfully [72]. Therefore, to image ultrathin flakes of 1T-TaS_2, the samples must be fabricated under an inert and dry atmosphere and must be measured under ultrahigh vacuum. For van der Waals materials that are air sensitive, another technique for preserving the integrity of the sample is to cap the exfoliated flake with another material, often a second van der Waals system. This method has been used successfully to fabricate samples for transport experiments. Furthermore, assembling complex heterostructures out of multiple van der Waals systems has been shown to produce devices that can exhibit exotic physics [6, 7]. While capping the material of interest would seem to preclude the possibility of imaging the sample using STM, if the capping flake is a monolayer, tunneling electrons can probe the structure beneath the topmost layer [73, 74].

In order to integrate an exfoliated flake into a device geometry that allows for transport measurements to be performed, additional considerations need to be taken into account. As mentioned above, the assembly of van der Waals systems into heterostructures is a promising field in its own right, and the methodologies applied to create these samples can be used to transfer an exfoliated flake into a previously fabricated electrode configuration. It is difficult to exfoliate ultrathin flakes that are of lateral dimensions larger than a few microns in area, limiting the possibilities for electrode design and creating the added challenge of locating the flake once it transferred. Furthermore, in order to be able to perform transport experiments *in situ*, a conduction channel through the flake needs to be clearly defined. This requirement entails incorporating an insulating substrate in the device geometry. The presence of an insulating surface creates a hazard for the STM tip as the sample is scanned and necessitates a device geometry that allows for fine control over navigation of the tip to regions of interest.

Lastly, it is important to note again that STM is a surface probe. Therefore, in order to correlate bulk properties with data collected using STM, the surface topography needs to reflect the bulk composition of the material. Of particular importance regarding STM experiments of 1T-TaS_2 are the effects of surface pinning on the equilibrium CDW phases and whether distinct surface and bulk CDW phases can coexist. While some experiments addressing this question have been performed on bulk samples of 1T-TaS_2 ([21, 75]), no studies have been conducted on ultrathin flakes.

2.4.2 Device design

In this section we present a device design that addresses the difficulties discussed in the preceding section and thus facilitates the imaging of exfoliated ultrathin flakes of 1T-TaS_2.

As previously mentioned, ultrathin flakes of 1T-TaS_2 are difficult to image with STM due to the instability of the material in air. Furthermore, 1T-TaS_2 samples cannot be cleaned *in situ*. It was observed that the material will undergo a structural phase transition to the 2H polytype when heated above 500 K. Consequently, previous STM experiments on bulk 1T-TaS_2 have typically relied upon either *in situ* cleaving of crystals to expose a clean surface [59, 76–78] or capping the material with graphene [73]. In this work, in order to maintain the integrity of the surface of the flake, the 1T-TaS_2 samples studied are fabricated using a polymer transfer technique under an inert atmosphere. Furthermore, all STM experiments are performed with a commercial Omicron low-temperature-STM in ultrahigh vacuum. Consequently, the samples are only exposed to air during wire bonding, prior to being loaded into the STM ($\sim$ 5 min).[6]

To facilitate coarse navigation to the flake, we utilize a telescope attached to an optical port of the STM. In the initial device design for measuring the CDW phases of exfoliated flakes, a gold pad was lithographically written with a hole in its centre. While thin micron sized flakes are not visible using any optical tools situated outside the STM, the contrast between the hole and the gold can be discerned with the attached telescope. An exfoliated flake was then transferred such that it spanned the hole in the contact pad. Consequently, when the tip was aligned with the hole, the flake could be approached with no chance of crashing into the insulating substrate (Figure 2.13). Future iterations of devices maintained this general concept of using optical contrast in order to approach with the STM tip within a few microns of a region of interest.

In the initial device design described above there did not exist a conduction channel that would allow for transport measurements to be performed on the transferred flake. A modified electrode design that facilitates measuring the electrical properties of the flake is given in Figure 2.14b. Gold contacts that are separated by a 2 μm wide gap are lithographically defined on a SiO_2/Si substrate. Hexagonal boron nitride (hBN) is transferred first, spanning the gap, followed by an ultrathin flake of 1T-TaS_2 that makes contact with the gold pads on either side of the gap. The hBN provides a more electronically clean and atomically flat substrate compared to the SiO_2 surface. Markers written on the gold contact pads using electron beam lithography are visible underneath the transferred flake and allow for fine navigation to regions of interest. With this electrode design, initial contact in the vicinity of the flake is facilitated by patterning gold regions with different thicknesses such that the contrast between the two gold layers can be used for coarse navigation. Figure 2.14a presents an atomic force microscopy scan depicting the basic electrode design. The array of navigation markers, comprised of single and double headed arrows as well

[6] A recent result in the literature, [73], found that the oxidation of the 1T-TaS_2 surface occurs on a timescale of around 47 minutes.

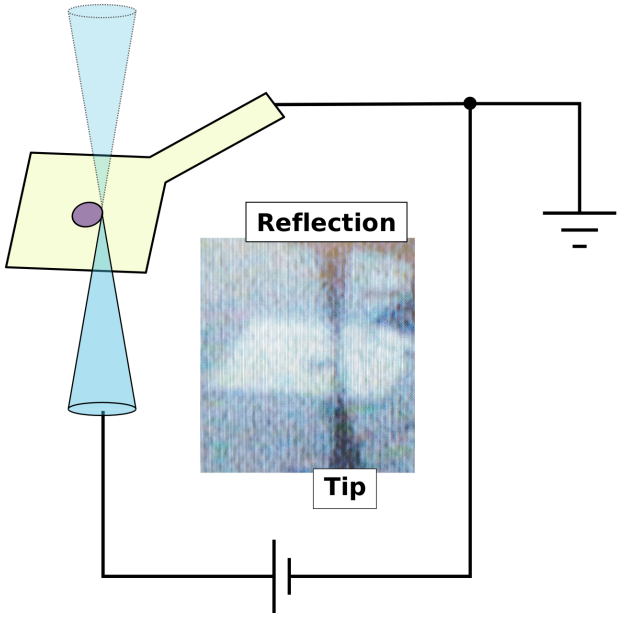

Figure 2.13: Coarse navigation in the STM. The tip is aligned with a hole in the gold pad. Once a flake is transferred such that it spans the hole, the device can be approached safely.

as plus symbols and squares, is visible on the thin portion of the gold contact pads. The contrast between the thick and thin gold regions is clearly visible in the optical images provided in Figure 2.14b panels (II) and (III).

The general procedure for the exfoliation and transfer of van der Waals materials is given below. Single crystals of 1T-TaS_2 are grown by chemical vapor transport with iodine as the transport agent . The exfoliation and transfer of all 2D materials is performed inside a N_2 filled glovebox with O_2 and H_2O partial pressures below 0.1 ppm. The materials are exfoliated using Scotch tape and transferred on top of each other. In the transfer procedure, the piece of tape with the exfoliated flakes is first pressed onto a thin film of polypropylene carbonate (PPC). The PPC film with the exfoliated flakes is then transferred onto a polydimethylsiloxane (PDMS) stamp on a glass slide. After locating a suitable flake on the film, the selected flake is aligned with its desired location on the device electrodes using a home-built microscope set-up, and then brought into contact with the substrate. The substrate is then heated, causing the PPC to peal off the glass slide, transferring the flake and the polymer to the device. The PPC is then removed using chloroform. A schematic depicting this procedure is given in Figure 2.14b. With this procedure any combination of van der Waals materials can be sequentially transferred. For example, as

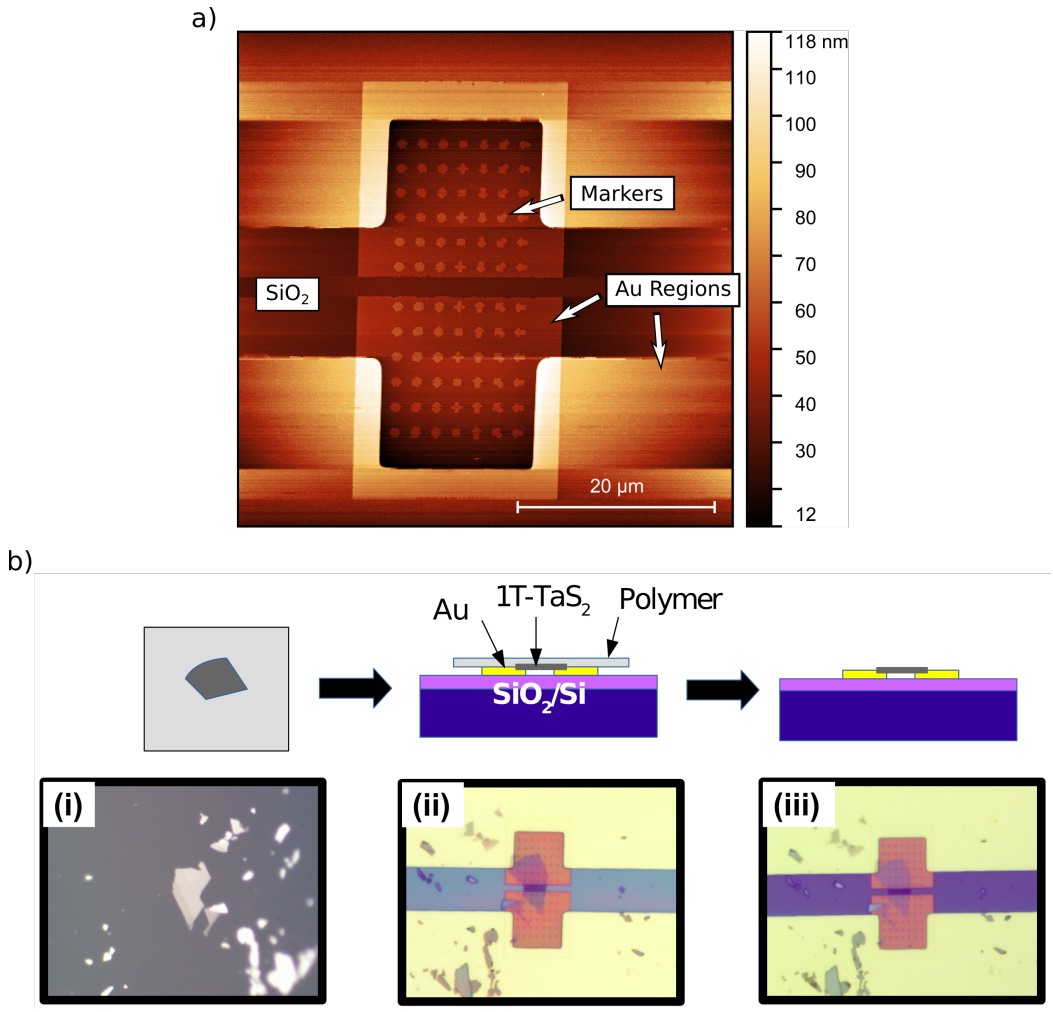

Figure 2.14: Basic device design and fabrication procedure. (a) An atomic force microscopy image illustrating the navigation markers written with electron beam lithography and the gold pads of different thicknesses. (b) A schematic of the polymer transfer procedure described in the main text. Hexagonal boron nitride was not used as the substrate in the sample pictured in the optical images in panels (I)-(III).

previously mentioned, hBN can be used to provide for a more ideal substrate. Additionally, few-layer graphite flakes can be transferred on either side of the conduction channel to serve as contacts for the 1T-TaS_2 flakes. For a more detailed step-by-step procedure of all of the steps in the fabrication process see Appendix A.

Figure 2.15 illustrates the basic navigation methodology used for imaging regions of interest on the transferred flake. After the initial approach with the tip, wide STM scans are taken until a marker is identified. Subsequent scans serve to chart out a route to the conduction channel. Once the channel has been located, imaging of the CDW phase commences. Despite the processing difficulties described throughout this section, and the exposure of the samples to various chemicals during fabrication, the exfoliated flakes are sufficiently free of contaminants to resolve the CDW superstructures characteristic of the bulk phases of 1T-TaS_2. While every attempt is made to avoid surface contamination, the non-ideal conditions make it challenging to maintain a stable tunneling junction with the tip. Applying a voltage pulse to the STM tip is a standard procedure for ridding the tip of contaminants and for achieving a stable imaging condition. Unfortunately, pulsing the tip over 1T-TaS_2 results in the violent creation of non-uniform pits in the topmost layers of the flake directly underneath the tip. While this technique has the potential to expose a clean surface, it is difficult to control, and is ultimately too destructive. Consequently, success is only achieved by preparing the tip prior to imaging the 1T-TaS_2 flake (e.g. by pulsing the tip over a region with no interest) and by then mapping out a navigational path that avoids existing surface contamination.

2.5 Conclusion

In summary, we have described the features of the commensurate and nearly commensurate CDW phases in 1T-TaS_2 observed using STM. Starting from the GL theory of CDW phase transitions, we have discussed how the appearance of satellite peaks surrounding the fundamental CDW modes in the fast Fourier transform of an STM image of 1T-TaS_2 can serve as a signature of the nearly commensurate phase. Additionally, we have presented a device design that allows for the measurement of both the topography of an exfoliated ultrathin flake of 1T-TaS_2 and the electrical properties of the flake *in situ*. With this device design, we have demonstrated the ability to repeatedly navigate to specific regions of interest on the flake, allowing for the measurement of the flake topography before and after electrical signals are applied to the device.

Ideally one would be able to perform spectroscopy on the ultrathin samples to obtain information regarding the local density of states of the material. However, we observed

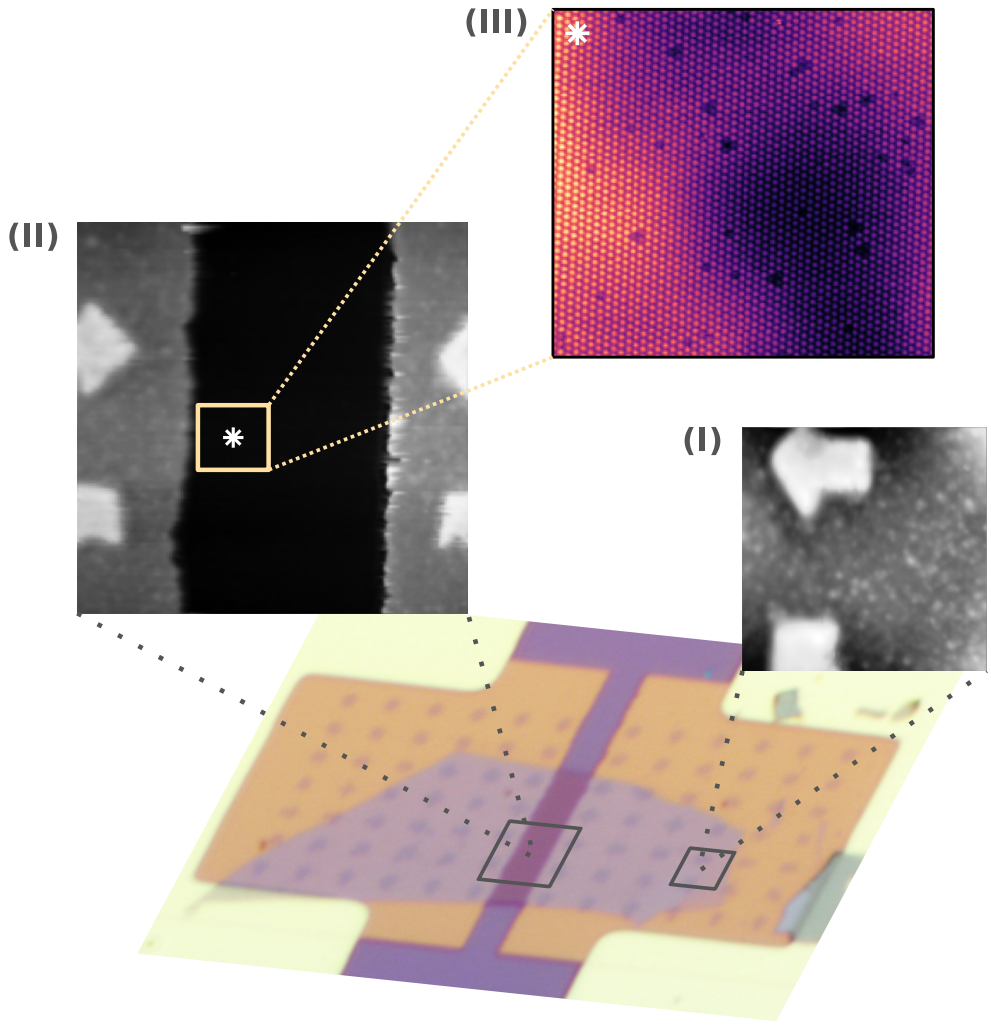

Figure 2.15: Fine navigation in the STM. After the initial approach with the STM tip, a wide scan is taken to orient where on the flake the tip has made contact (I). Markers written on the gold pads are visible in the topographic scan. Once a marker is identified, a course is charted to the conduction channel, the edges of which are also visible through the flake (II). A specific area within the conduction channel can be continuously imaged over the lifetime of the sample (III), by identifying the location of the area of interest relative to the markers nearest to the channel. (I) and (II) were taken at 260 K while scan (III) was taken at 77 K. (I) $V_t = 0.75$ V, $I_{set} = 0.20$ nA. (II) $V_t = 0.75$ V, $I_{set} = 0.20$ nA. (III) $V_t = -2.04$ V, $I_{set} = 1.11$ nA.

that the condition of the exfoliated flakes we studied prevented us from maintaining the tip stability required for such an experiment. Navigation would typically consist of finding a path relatively free of contaminants and taking as few scans as possible while maneuvering towards the conduction channel. While we were unable to conduct energy resolved experiments, as demonstrated in this chapter, a large amount of information can be obtained based solely on topography. Utilizing the language of GL theory, the symmetries of an arbitrary CDW phase can be enumerated and discussed. 1 T$-TaS_2$ has long been studied due to the variety of CDW phases exhibited and identifying the characteristic superstructures associated with each phase provides valuable insight into the state of the material.

Chapter 3

Observation and manipulation of an electronically inhomogeneous state in ultrathin 1 T$-TaS_2$

3.1 Introduction

The phase diagrams of systems exhibiting strong electron correlations are typically comprised of many possible equilibrium states, whose origins and properties are often surprising. One classic example is the perovskite manganites, where competition between different magnetic states, in the presence of quenched disorder, gives rise to a phase separated state where percolative physics is integral in explaining observed colossal magnetoresistance [11, 79–81]. In manganites there exists two competing phases separated by a first-order phase transition: a ferromagnetic metallic phase (FM), and an antiferromagnetic insulating phase (AFI). In the presence of quenched disorder, the hysteresis region associated with the FM-AFI transition is modified and inhomogeneity is observed [82, 83]. While short-length correlations still exist, the global phase is glassy in nature, exhibiting both FM and AFI regions. As a result of this mixture of metallic and insulating domains, the electrical bulk behaviour of the system can be described via percolation theory [84, 85]. Furthermore, it is observed that small perturbations, such as magnetic fields, can result in large changes in the electrical properties of the system, as only small fields are required to align the magnetic moments in nano-sized clusters. Consequently, as a function of these perturbations, colossal magnetoresistance is observed.

The phase diagram of 1T-TaS_2, exhibits some similarities to that of manganites. As dis-

cussed in detail in Chapters 1 and 2 of this thesis, this Ta dichalcogenide has a particularly rich phase diagram with multiple CDW equilibrium phases, each possessing different electrical characteristics. When the material is cooled it transitions from a normal metal to an incommensurate CDW (IC) at $\sim$ 545 K, a nearly commensurate CDW (NC) at $\sim$ 355 K, and a commensurate CDW (C) at $\sim$ 185 K, becoming more insulating with each phase transition. While much of the research in the literature concerning 1T-TaS_2 has focussed on bulk crystals of the material, the phase diagram is further expanded when the material is thinned to the ultrathin limit ($<$ 10 nm thick). Previous work in ultrathin flakes of 1T-TaS_2 have focussed on the electrical behaviour of the material within the hysteresis region of the NC-C transition. It was found that the resistivity of the material can be bidirectionally switched, driven reversibly through intermediate states whose resistivities lie between the extrema values associated with the NC and C states [30, 86–88]. The microscopic nature of these non-equilibrium intermediate phases remains an open question, with some debate persisting whether these states are unique metastable states, possessing electronic and structural order characteristically different than bulk 1T-TaS_2 phases, or instead whether they are composed of domains of bulk equilibrium states. Experiments in the literature have attempted to elucidate the spatial characteristics of these non-equilibrium states [86, 89, 90], but no experiment has probed the electronic structure at the nanoscale.

Sections 1.2.2 and 2.4 of this thesis briefly introduced the role stacking plays in the formation of the equilibrium CDW phases. In this chapter, we expand on this discussion as we aim to clarify the microscopic nature of the CDW states in the hysteresis region of the NC-C phase transition of ultrathin 1T-TaS_2. After describing the electrical behaviour of ultrathin devices, we then attempt to correlate this behaviour with changes in electronic structure. Exfoliated flakes are imaged with scanning tunneling microscopy (STM), utilizing the device design presented in Section 2.4.2. Additionally, we image changes in the measured electronic structure after the application of lateral electrical signals and after repeated rastering of the STM tip.

3.2 Electrical properties of ultrathin 1 T$-TaS_2$

In bulk flakes of 1T-TaS_2, measurements of the temperature dependent resistivity through the NC-C transition are hysteretic. As the material is thinned, the hysteresis region exhibits marked changes. In the ultrathin regime, stepwise transitions are observed (Figure 3.1), and, as the 2D limit is approached, the region widens until at a thickness of $\sim$ 2 nm ($\sim$ 4 atomic layers), the jump in the resistivity disappears altogether [31]. Within the NC-C transition region, it has been observed that phase transitions can be induced by applying

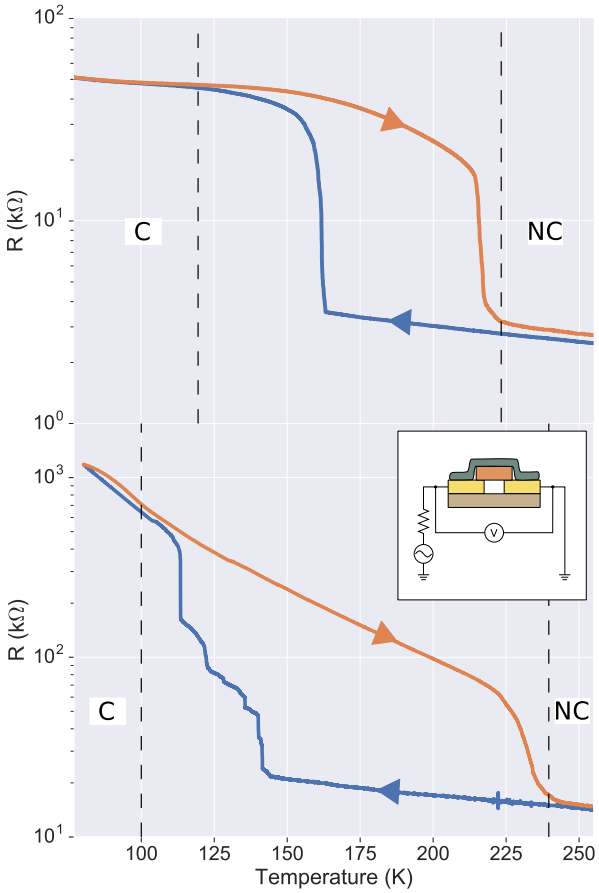

Figure 3.1: Temperature dependent resistance of a bulk flake of 1T-TaS_2 (top) and of an ultrathin flake of 1T-TaS_2 (bottom). The inset shows a schematic of the circuit used to measure the resistance. The material stack consists of 1T-TaS_2 (green)-hBN (orange)-Au (gold)-SiO_2 (brown).

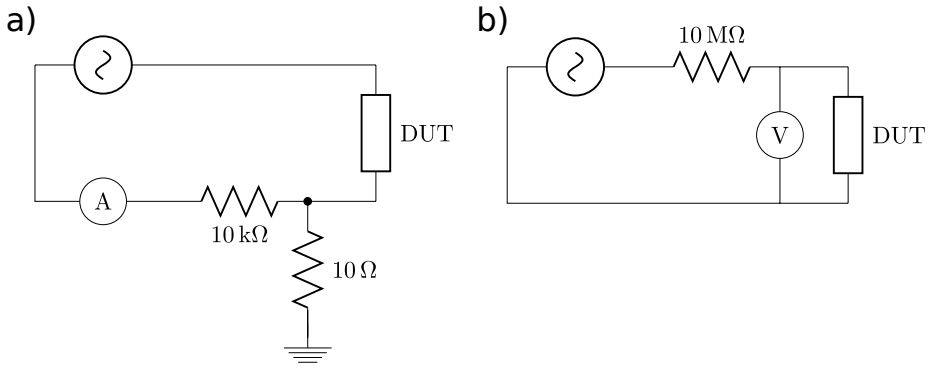

Figure 3.2: (a) AC driving measurement circuit. (b) Circuit for measuring the resistance of the device.

lateral voltage signals across the sample. In the case of bulk flakes, this electrical driving is volatile in nature and unidirectional. By applying a lateral voltage to the high-resistance C phase, a transition can be induced into the NC phase, but in order to recover the initial C state, the temperature of the sample needs to be adjusted. On the other hand, it has been demonstrated that by thinning the material to the ultrathin limit, bidirectional, non-volatile switching of 1T-TaS_2 is possible. Furthermore, non-equilibrium phases, with resistances that lie between that of the extrema associated with the NC and C phases, can be accessed that are metastable [86].

In this section, transport measurements are presented that are representative of the electrical behaviour of ultrathin 1T-TaS_2 described above. The data was collected from an ultrathin sample with a thickness of ~ 8 nm. The electrode geometry utilized was the same as that described in Section 2.4.2, with graphite flakes transferred to serve as contacts to the 1T-TaS_2 flake. After cooling the sample from above the NC-C phase transition to 170 K, non-equilibrium resistance states are driven to by applying a series of linear sweeps of a lateral voltage signal across the sample. At 170 K the ground state of the system is the C phase, with the NC phase being metastable.[1] The maximum voltage applied during the driving was ramped up as the resistance of the material increased. The resistance of the device was measured using a four-terminal constant current circuit that does not exclude the contact resistance (Figure 3.2b). Driving the sample was attempted with both DC and AC signals. For all DC voltage sweeps, a Keithley Source Measurement Unit (Keithley 2401 or Keithley 2450) was used to apply the bias voltage and to measure the

[1]See Section 4.2 for a more detailed discussion of the thermodynamics of ultrathin 1T-TaS_2 in this temperature range.

resulting current. For the traces plotted in Figure 3.3, the DC sweep rate was 0.05 V/s. AC measurements were performed with an SR830 lockin, with a signal frequency of 17.8 Hz. The circuit included a current divider in order to protect the lockin from excessive current (Figure 3.2a).

Figure 3.3 presents two different driving experiments. In Figure 3.3a the sample was driven with multiple DC sweeps, while in Figure 3.3b, lateral AC sweeps were applied. In general, the electrical behaviour observed reproduces that seen in the literature for ultrathin flakes of 1T-TaS_2. As the voltage is increased within a single sweep, drops in the current (i.e. jumps in the resistance) are observed. The driving process appears stochastic, in the sense that for some sweeps the resistance remains constant, while for others it changes more dramatically in a manner not obviously correlated to the voltage applied. At a certain critical value the resistance saturates. Once the resistance no longer increases and the voltage is ramped to larger values, the resistance in the sample eventually drops, and under the right conditions the material returns to a lower resistance state (drives 8 and 9). Between drives 7 and 8 the sample sat overnight and the bulk resistance of the device increased, indicative of the metastability of the intermediate states.

The AC driving presented in Figure 3.3b displays many of the same features observed with the DC driving. As the AC voltage sweeps are applied, the resistance increases until it saturates at an intermediate resistance state. In Figure 3.3b, the solid lines represent sequential sweeps, and the sample sat overnight between sweeps 4 and 5. The dashed pink trace represents a single sweep, in which the maximum voltage was immediately set to 5 V. The maximum resistance reached using a single AC sweep is approximately the same as that obtained using multiple sweeps, and is also the same resistance value driven to using a DC signal. The same single sweep pink trace is displayed in Figure 3.3a in blue. However, using an AC voltage, the saturated state is reached at a lower maximum voltage value, and with less stochastic variability.

Figure 3.4 demonstrates repeated toggling between the low-resistance state and the intermediate resistance state. When driving towards the intermediate resistance state, an AC signal is applied, while when driving back to the low-resistance state a DC signal is used. This data clearly demonstrates the saturation of the bulk resistivity as the flake is driven towards the C state, at a value calculated to be 70.9 ± 3.4 kΩ. In the measurements displayed in Figure 3.4a, a maximum AC voltage of 5 V was applied to the device. However, in Figure 3.4c the voltage was ramped to 7 V. Despite the increased voltage, the resistivity of the sample remained fixed at the saturation value. In previous results from the literature [86], the authors were unable to drive the flake entirely back to the low-resistance state, no matter what voltage was applied, as the sample transitioned again to a higher resistivity as the voltage was swept back to 0 V (Figure 3.5b and c). However,

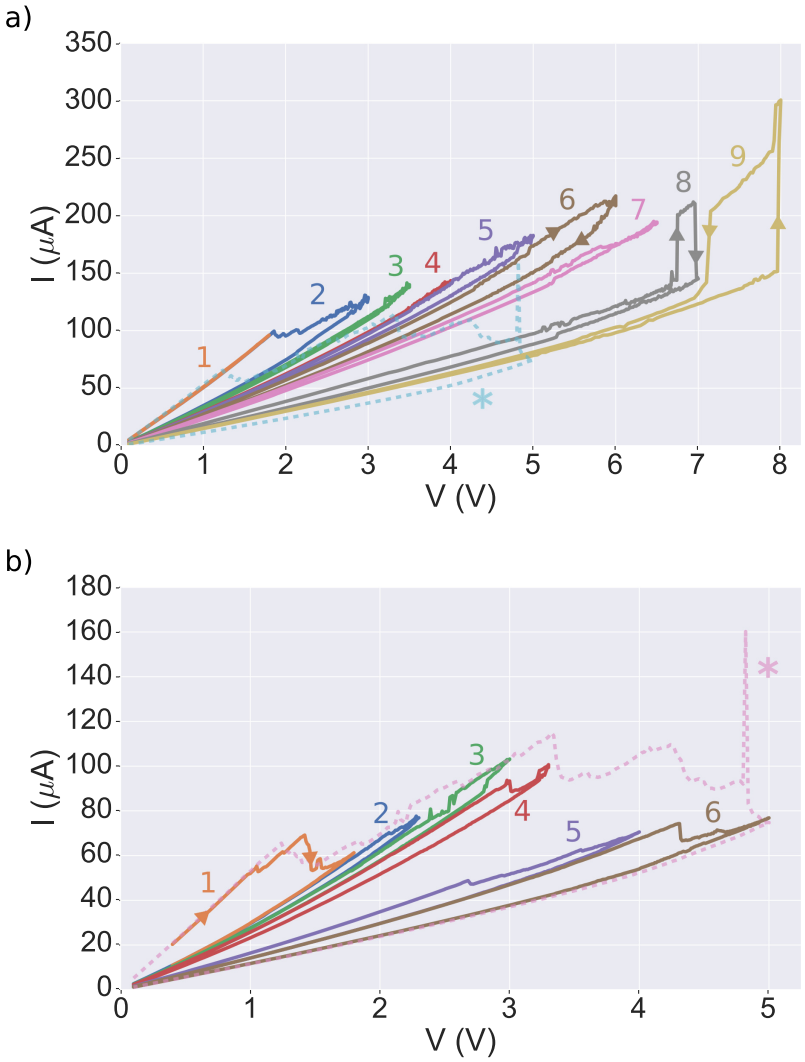

Figure 3.3: (a) Driving by applying a lateral DC bias. The sample sat overnight between drive 7 and drive 8. The blue trace, labelled with an asterisk, is a drive performed by applying a lateral AC bias (see Figure 3.4b panel i) and indicates the high and low-resistance states of the sample. (b) Driving by applying a lateral AC bias ($V = V_{rms}$). The sample sat overnight between drive 4 and drive 5. The pink trace, labelled with an asterisk, is the same as the AC drive in (a) illustrating how the high and low-resistance states do not vary whether a DC or AC bias is used. In all plots, the direction of the voltage sweep coincides with a transition from a low to a high-resistance state (e.g. as illustrated in Drive 1 of (b)), unless otherwise indicated by arrows.

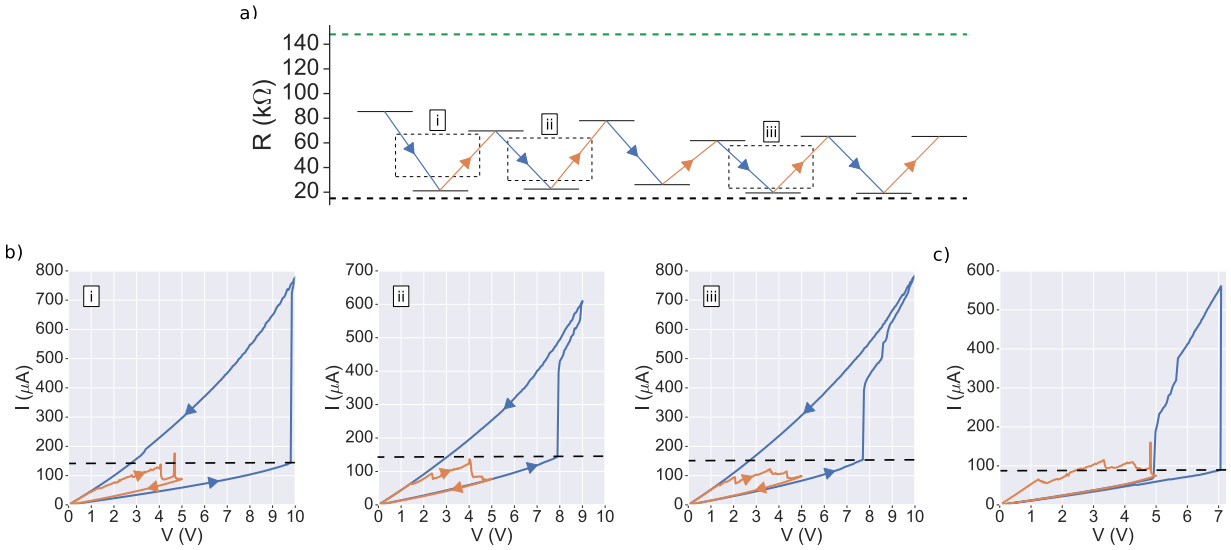

Figure 3.4: (a) Experimental data demonstrating bidirectional switching of the bulk resistance. The resistance is repeatedly toggled between a low-resistance state comparable to that obtained when cooling the sample from above the NC-C phase transition (black dashed line), and a high-resistance intermediate state. The resistance of the state reached by warming the sample from 77 K is given by the green dashed line. (b) The individual traces outlined in the dashed boxes in (a). Driving to the high-resistance states (orange curves) was performed by applying an AC bias while driving to the low-resistance state (blue curves) was performed by applying a DC bias. The critical current at which the transition from the high to the low-resistance state occurs is approximately equal in all three plots, as indicated by the dashed black line. (c) Attempting to drive the device further by going to a greater AC voltage. Using only a lateral AC bias, we were unable to drive the sample from the high-resistance state to the low-resistance state. As the voltage was swept back to 0 V the sample returned to the high-resistance state.

Figure 3.4a demonstrates the ability to repeatedly drive to the saturation resistivity and then back to the low-resistance state. Driving completely to the low-resistance state was accomplished by sweeping the DC signal to a higher voltage and at a faster rate (0.50 V/s), compared to the experiment presented in Figure 3.3a. A detailed study of the dynamics of the driving process is beyond the scope of the experiments described in this section, but these results indicate that such a study is potentially an avenue worth pursuing.

3.2.1 Non-equilibrium resistance states

Previous scanning optoelectronic measurements of both bulk and ultrathin samples of 1T-TaS_2, taken within the hysteresis region of the NC-C transition, have demonstrated spatial inhomogeneity at the micron length scale [86, 89, 90]. Upon both cooling and warming the sample, optoelectronic maps indicate the presence of mixed states, revealing that different regions of the sample transition at different temperatures. This result is not uncommon for first-order phase transitions, where nucleation can depend strongly on the local environment, and long-lasting metastable states are observed.

Patel et al. (2020) were the first to attempt to correlate electrical behaviour of ultrathin 1T-TaS_2 within the NC-C transition region with structural information regarding the phases of the material at the microscopic scale [86]. The device measured in those experiments consisted of the stacked heterostructure (1T-TaS_2)-(WSe_2)-(graphene), ordered from top to bottom. When this structure is illuminated with a laser, a vertical photocurrent is generated underneath the laser spot. The magnitude of the current depends on the phase of 1T-TaS_2, and thus the state of the ultrathin flake can be mapped by rastering the laser across the heterostructure, with the resolution of the map determined by the laser spot size. An ultrathin flake of 1T-TaS_2 was mapped as the temperature of the sample was varied and as electrical signals were applied across the device in a manner similar to what was described above. Figure 3.5 presents data showing optoelectronic maps taken as the flake was bidirectionally driven. The red in the maps corresponds to regions of the flake in the low-resistance state while the blue corresponds to high-resistance areas. Figures 3.5a and b corresponds to the applied voltage sweeps, while Figure 3.5c presents how the bulk resistivity of the sample changed after each individual voltage ramp. In general, the authors found that the flake transitioned from the NC phase to the C phase unevenly as a function of temperature, but relatively uniformly as the flake was driven electrically. Ultimately, these experiments were limited by the resolution of the scanning laser set up. In the subsequent section we present data collected using STM that aims to clarify the nanoscopic nature of the CDW states in the hysteresis region of the NC-C phase transition of ultrathin 1T-TaS_2, and how these CDW states evolve as electrical signals are applied.

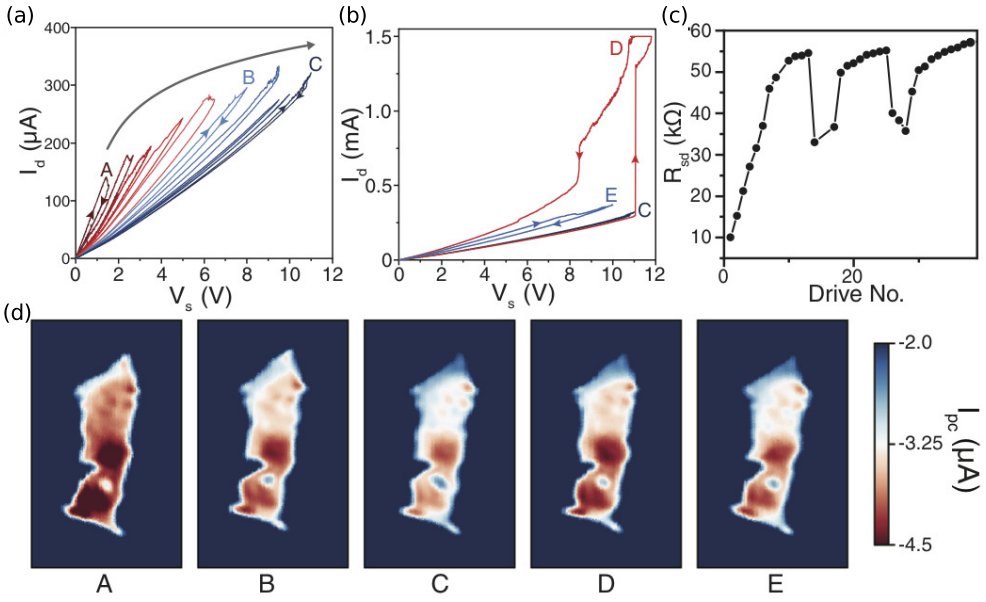

Figure 3.5: (a) Lateral voltage sweeps with a DC signal. As the voltage is increased, the material transitions to states with higher resistivities, resulting in drops in the current measured. (b) Driving in the opposite direction. At a certain critical voltage, the flake is driven towards the low-resistance state. When the voltage is swept back towards 0 there is a partial transition back to a higher resistance state. (c) Multiple driving runs indicating how the material is toggled between two intermediate states. (d) Scanning photocurrent maps demonstrating the spatial evolution of the flake during driving. This figure was taken from personal correspondence (T. Patel). A modified version of this figure was presented in [86].

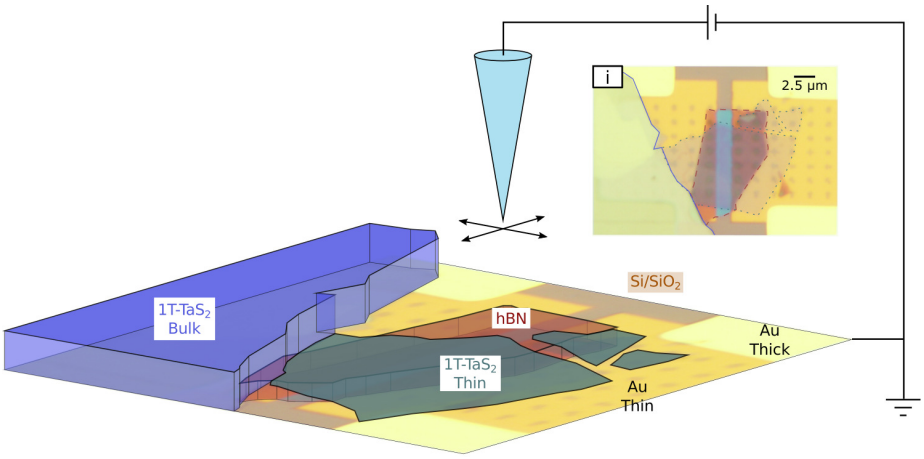

Figure 3.6: Measuring the topography of an ultrathin flake of 1T-TaS_2. The different van der Waals materials are overlayed on an optical image of the device. In this sample a bulk flake of 1T-TaS_2 was transferred along with the thin flake, though only the thin flake spans the gap in the gold electrodes. (i) Top-down optical view of the device.

3.3 Electronic inhomogeneity in ultrathin $1\,T-TaS_2$

The STM data presented throughout this section was taken from an approximately 8 nm thick flake with lateral dimensions of 5 μm by 10 μm. The sample was cooled from 260 K, where it is in an incommensurate state, to 170 K, within the NC-C transition hysteresis region. Figure 3.6 illustrates the geometry of the device. In this particular sample, a bulk flake of 1T-TaS_2 was transferred along with the thin flake, though the bulk flake did not encroach upon the conductance channel.

Topography was measured both where the flake lies on the gold contact pad (Figure 3.7) and also within the conductance channel where the flake lies on hBN (Figure 3.9).[2] On both the contact pad and the hBN, the imaged topography exhibits spatial inhomogeneity with two distinct region types, distinguishable by the presence or absence of bright, characteristic

[2]The image in the centre panel of Figure 3.7 was generated by applying a Sobel filter to the raw data (the left panel). Applying a two dimensional Sobel filter amounts to taking the gradient of the image, and is useful for identifying edges. In figure Figure 3.7, only a vertical Sobel filter, given by the kernal

$$\begin{pmatrix} 1 & 0 & -1 \\ 2 & 0 & -2 \\ 1 & 0 & -1 \end{pmatrix} \tag{3.1}$$

was applied to produce the centre panel.

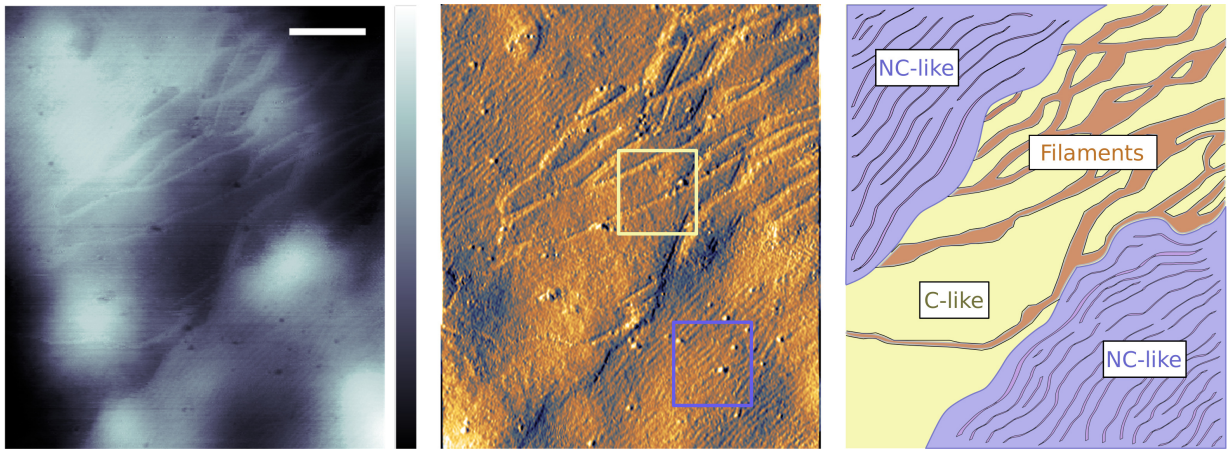

Figure 3.7: (Left) A wide STM scan comprised of two distinct region types. In the top left and bottom right there are NC-like regions with visible striations, while a C-like region with no striations runs from the bottom left to the top right. The C region also contains filaments. Scale bar = 70 nm, $V_t = 0.30$ V, $I_{set} = 1.40$ nA. (Middle) The image generated by applying a horizontal Sobel filter to the flattened, raw data to extract the gradient of the scan along the horizontal axis. (Right) A schematic delineating the different regions visible in the STM scan.

striations. These striations are reminiscent of the domain walls present in the bulk NC phase of 1T-TaS_2 [59, 76], and thus, throughout this work, we use the label "NC-like" to identify the regions where striations are observed, and "C-like" to identify the other region type. It is important to note that the observed state is not simply an NC state with asymmetrically arranged domain walls nor is it an NC state with a domain wall period different from the equilibrium NC value as has been previously suggested [86, 88], but rather the state is specifically composed of defined, irregularly shaped NC-like and C-like domains. With the STM scans indicating the presence of domains on a nanoscopic length scale, the optoelectronic maps with micron resolution discussed in the previous section can be interpreted as presenting an average of the NC-like and C-like volume fractions present within the laser spot size. Within the C-like region in Figure 3.7 filament structures are also observed that are irregularly arranged.

In the top left and bottom right of each panel of Figure 3.7, NC-like regions exist containing striations, while running from the bottom left of the image to the top right, a C-like region is observed. Fast Fourier transforms (FFTs) of each region (Figure 3.8) support this identification. The FFTs of the NC-like regions contain satellite peaks in addition to the fundamental CDW modes. The presence of satellite peaks is indicative of domains, and is consistent with what is observed in the bulk NC phase of 1T-TaS_2 [59]. In the FFT of the C-like region only the fundamental, 3-fold symmetric CDW modes are observed.

To properly reset 1T-TaS_2 such that it is definitively in the NC state, the sample needs to be heated above the NC-IC transition temperature. However, we only heated the material to 260 K due to limitations in our experimental set-up. Therefore, for the data collected when the system was cooled to 170 K from 260 K, it is reasonable to expect some residues of the T phase to be present. The domain walls in the NC-like region in Figure 3.8 lack three-fold symmetry and are instead similar to the discommensurations observed in the bulk T phase [68, 91]. Ginzburg-Landau theory is often used for describing a triple CDW material, like 1T-TaS_2, with wave vectors $Q^{(i)}$, $i = (1, 2, 3)$ [54, 92]. All of the bulk phases of 1T-TaS_2 are known to satisfy the triple-Q condition, $Q^{(1)} + Q^{(2)} + Q^{(3)} = 0$. While the wave vectors of the C, NC and IC phases are oriented 120° degrees apart, in the T phase this constraint is relaxed [23]. The fundamental CDW wave vectors in the NC-like region found in Figure 3.8 have the same characterization as the T phase, in that they satisfy the triple-Q condition and the angles between the wave vectors are not equal to 120°. The width of each domain is approximately 4.4 nm as determined from the location of the most prominent satellite peak in the FFT. Given the thermal history of the sample it is not surprising that features characteristic of the T phase were observed.

The existence of electronic inhomogeneity provides evidence that CDW formation in

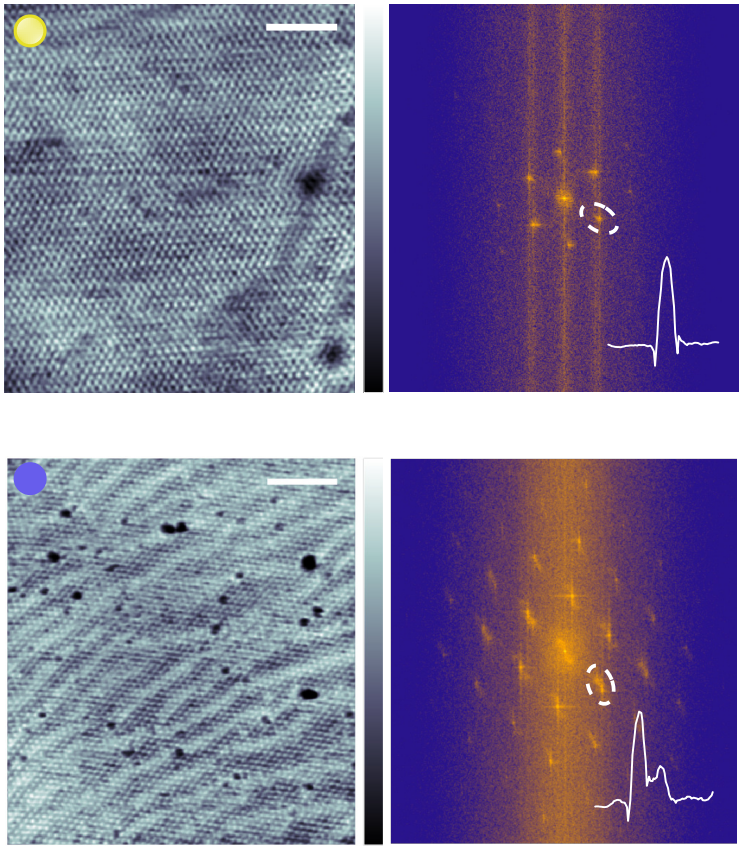

Figure 3.8: (Top) A detail of the C-like region outlined in yellow in Figure 3.7, and its corresponding FFT. Only the fundamental CDW modes are visible in the FFT. A line cut through the circled peak indicates the absence of a satellite peak. Scale bar = 9 nm, $V_t = -0.30$ V, $I_{set} = 1.40$ nA. (Bottom) A detail of an NC-like region similar to that outlined in blue in Figure 3.7,, and its corresponding FFT. The FFT contains the fundamental CDW modes as well as satellite peaks, as evident in a line cut through the circled peak. The presence of a satellite peak is indicative of the NC phase. Scale bar = 11 nm, $V_t = 0.40$ V, $I_{set} = 0.60$ nA.

ultrathin 1T-TaS_2 stems from local interactions. The presence of a CDW phase at all implies that even at elevated temperatures, a Peierls instability along the c axis is not likely the dominant interaction driving CDW formation. This observation is in agreement with theory that demonstrates that the CDW phases of 1T-TaS_2 can arise from purely intralayer interactions [23], and experiment [19, 21, 75] which finds the existence of isolated CDW phases at the surface of bulk crystals. The observation of electronic variation in the CDW state that is stable over an extended period of time further supports the dependency of the CDW phase in ultrathin 1T-TaS_2 on the local environment. In the quasi-2D limit, defects in the electronic crystal would play a significant role in determining the properties of 1T-TaS_2, compared to in bulk samples of the material [31, 93]. The role of defects in determining the structure of the CDW phase in ultrathin 1T-ceTaS2 is discussed in further detail in Section 4.3.

3.3.1 The coexistence of chiral states

In the topographic scan of the flake taken where it lay on hBN (Figure 3.9) we observe the presence of a mirror domain wall in the CDW phase. With its own lattice parameters and symmetry, the CDW phase can be described as an electronic crystal. In addition to the typical lattice definitions associated with a crystal, the CDW phase can also possesses various defects. We have already discussed the discommensurations present in both the C and the NC phase of 1T-TaS_2, but here we find the existence of another common defect observed in crystals, a mirror twin boundary. As described in Section 2.2.3, there are two possible chiral orientations of the C and NC phase. In Figure 3.9 we observe a boundary, outlined in red, that separates a region in one chiral orientation from a region in the other orientation. The FFT of an area where both chiralities are present will consist of the superposition of the fundamental CDW modes for each orientation (Figure 3.10) resulting in the appearance of 12 peaks where each pair of peaks corresponding to the same CDW fundamental mode ($\boldsymbol{Q^{(1)}}$ or $\boldsymbol{Q^{(2)}}$ or $\boldsymbol{Q^{(3)}}$) are separated by an angle $\approx 2 \times 13.9° = 27.8°$. A detail of the boundary wall is given in Figure 3.11 along with the FFT of the image. As expected, the FFT contains 12 peaks.

3.4 Electrically driven and tip induced phase transitions

To perform bidirectional resistance switching, we first navigate to a region of the flake within the conduction channel where the flake lies on hBN (Figure 3.9). NC-like and C-

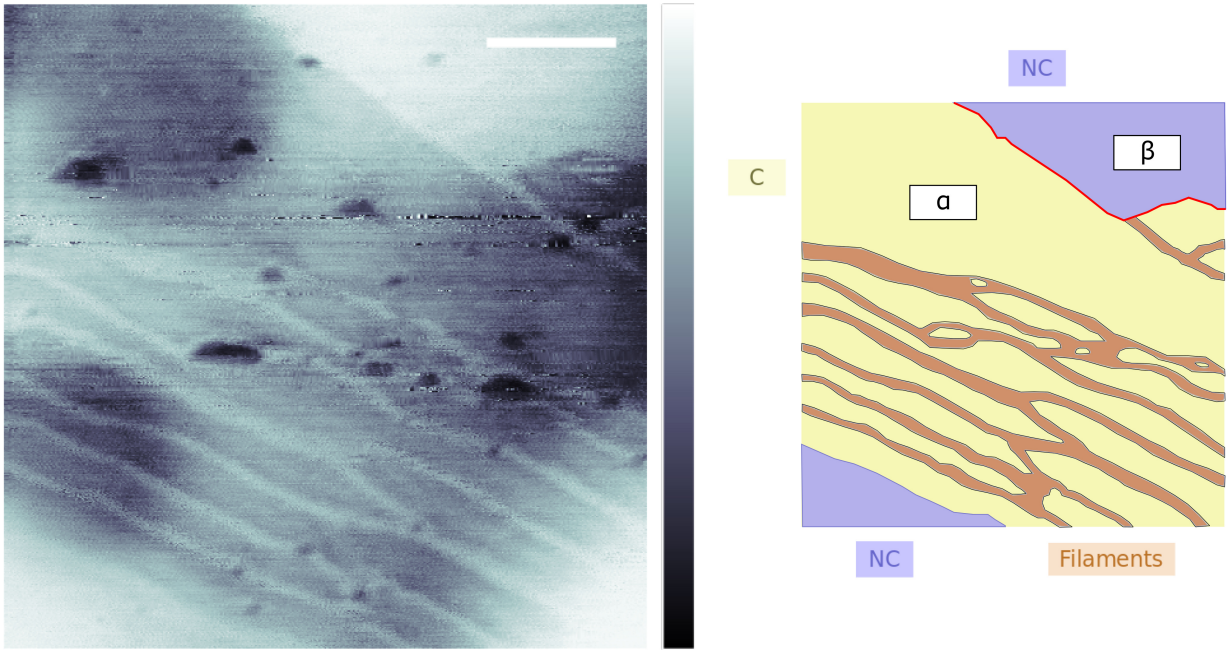

Figure 3.9: (a) (Left) A wide STM scan comprised of two distinct region types. In the top left and bottom right there are NC-like regions with visible striations, while a C-like region with no striations runs from the bottom left to the top right. The C region also contains filaments. Two chiral orientations of the CDW are observed, labelled α and β. Scale bar = 30 nm, V_t = 0.30 V, I_{set} = 1.40 nA. (Right) A schematic delineating the different regions visible in the STM scan.

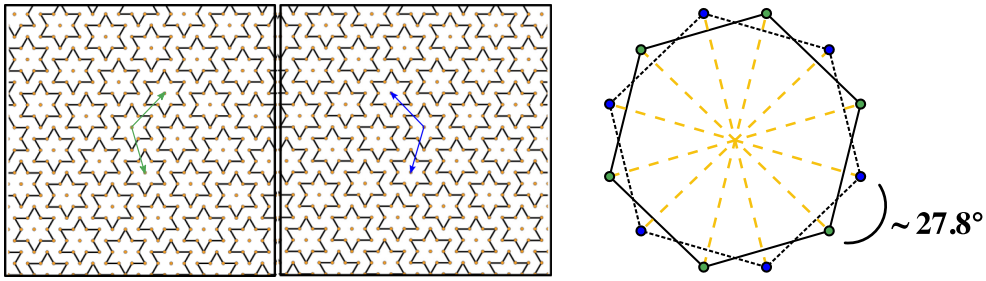

Figure 3.10: The presence of a mirror twin boundary (represented schematically in the left panel of the figure) causes the appearance of 12 peaks in the FFT (right panel). In the C phase, the pairs of peaks are separated by 27.8°, twice the angle between the CDW wave vector and the atomic lattice vector.

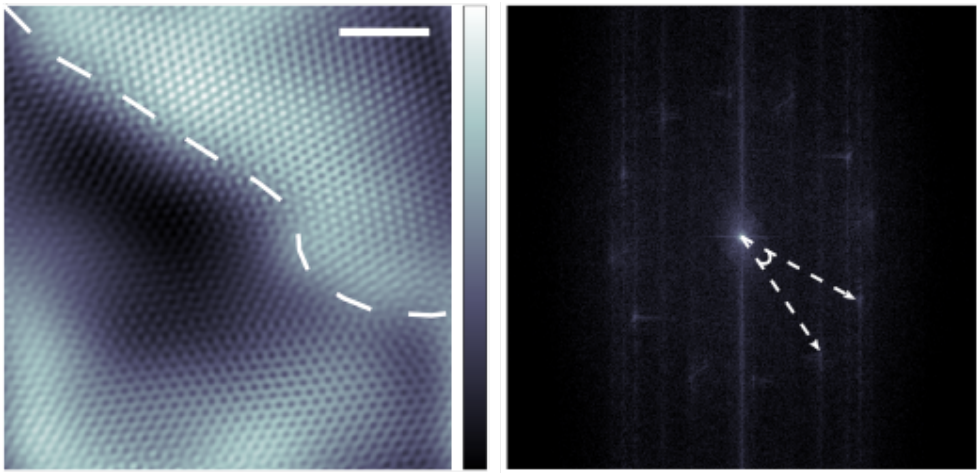

Figure 3.11: (Left) A mirror twin boundary is observed in an ultrathin sample of 1T-TaS_2. Scale bar = 8 nm, V_t = 0.44 V, I_{set} = 0.75 nA. (Right) FFT of the same region. Twelve peaks are visible indicating the coexistence of the two different chiral orientations of the CDW in 1T-TaS_2. The angle between the two vectors indicated is equal to $\sim 27.5°$.

like regions similar to those observed in the topography scans of the flake sitting on gold are observed. There are defects in the image that are similar to the etch pits measured by Yamaguchi et al. (1997) [72]. These pits grow with repeated scanning of the tip. In the context of this work, these defect sites provide a set of markers for tracking the evolution of the different features of the CDW phase.

We initially start in the low-resistance state at 170 K, and run a series of linear sweeps of laterally applied voltage, as described in Section 3.2 of this thesis. Figure 3.12b illustrates one set of STM images taken before and after a set of electrical signals were applied. In this particular case, a DC voltage was applied with a sweep rate of 0.05 V/s, and the maximum voltage set was 4 V. After the voltage sweeps, the measured resistance had increased by only $\sim 1\%$ (Figure 3.12a). Similar to Figure 3.7, distinct NC-like and C-like regions are observed prior to applying a bias across the sample, and the C region also contains filament structures. After electrically driving the flake, the NC region now dominates the image. It is important to recognize that an STM scan of a single area (150 nm $\times$ 150 nm) of the flake will not provide quantitative data regarding the total volume fractions of the two domain types. Simulations discussed in Chapter 4 will illustrate how changes in the inhomogeneous phase across the entire sample can result in bidirectional resistance switching.

In addition to the changes caused by the application of an electric field, we also observe interconversion between the domain types as a consequence of the rastering tip. The

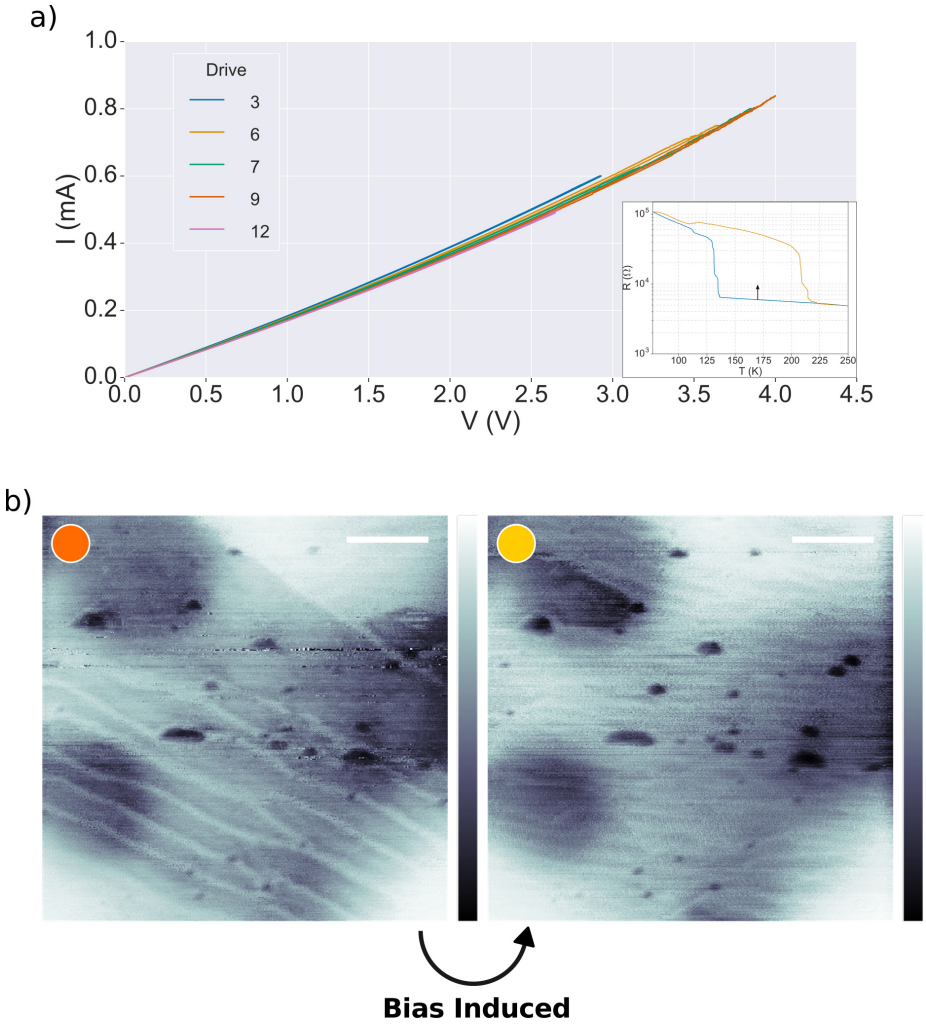

Figure 3.12: (a) The IV traces measured while electrically driving the sample. In this instance the resistance only increased by $\sim 1\%$. (b) STM scans illustrating the change in the phase separated state with the application of a bias. Scale bar = 30 nm, $V_t = 0.30$ V, $I_{set} = 1.40$ nA. Initially there is a mix of the C-like and NC-like phases. After a bias is applied across the sample, the NC region dominates.

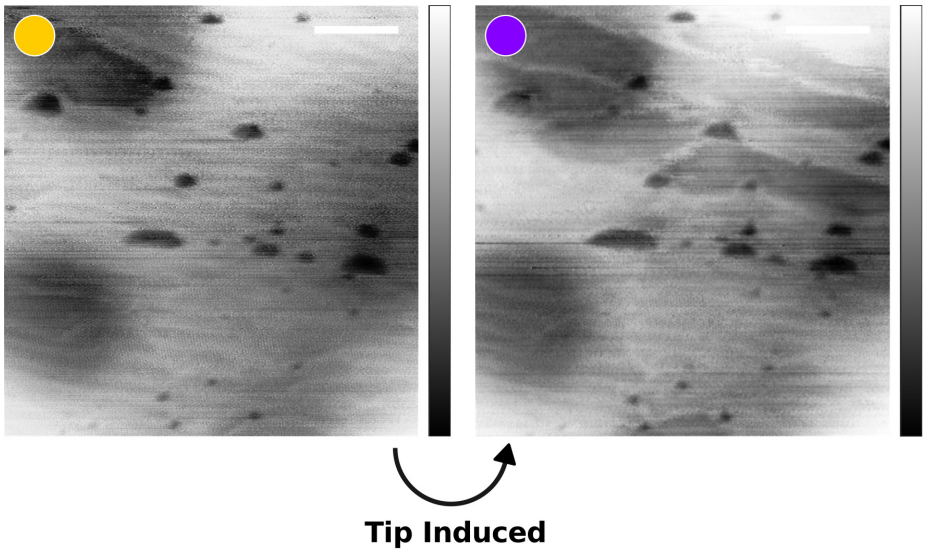

Figure 3.13: Consecutive STM scans demonstrating the effect of tip rastering on the phase separated state. The initial state (left) is identical to the "after" state given in Figure 3.12b. Scanning with the tip resulted in sections of the NC-like phase to be converted to the C-like phase. Scale bar = 30 nm, $V_t = 0.30$ V, $I_{set} = 1.40$ nA.

scans given in Figure 3.13 were taken following the electrical driving and illustrate the effect of the tip on the phase separated state. With repeated scanning of the tip, at a tunneling voltage of $V_t = 0.3$ V, NC-like regions of the sample within the scanning area were converted to C-like regions. Unlike what is observed during the electrical driving, the overall resistance of the sample did not change from one scan to the next, indicating that the observed differences in the scans were due to the local perturbation of the tip as opposed to part of a global thermodynamic process.

The scans in both Figure 3.7 and Figure 3.9 contain additional features we have labelled "filaments". These structures bear some similarity to the striations observed in the NC-like domains and are sensitive to perturbations. Both the scanning of the STM tip and the application of a lateral electric field change the arrangement of the filaments within the scan window. Whether these features represent sparse residual boundaries of NC-like domains or an entirely separate structure, warrants future study.[94]

The evolution of the state due to driving can be clearly seen in the changes in the FFTs of consecutive STM scans (Figure 3.14). Initially, the FFT contains 12 peaks. There are two possible chiral orientations of the CDW that arise in 1T-TaS_2, often referred to in the literature as the α and β orientations [60]. The initial STM scan in Figure 3.12 contains

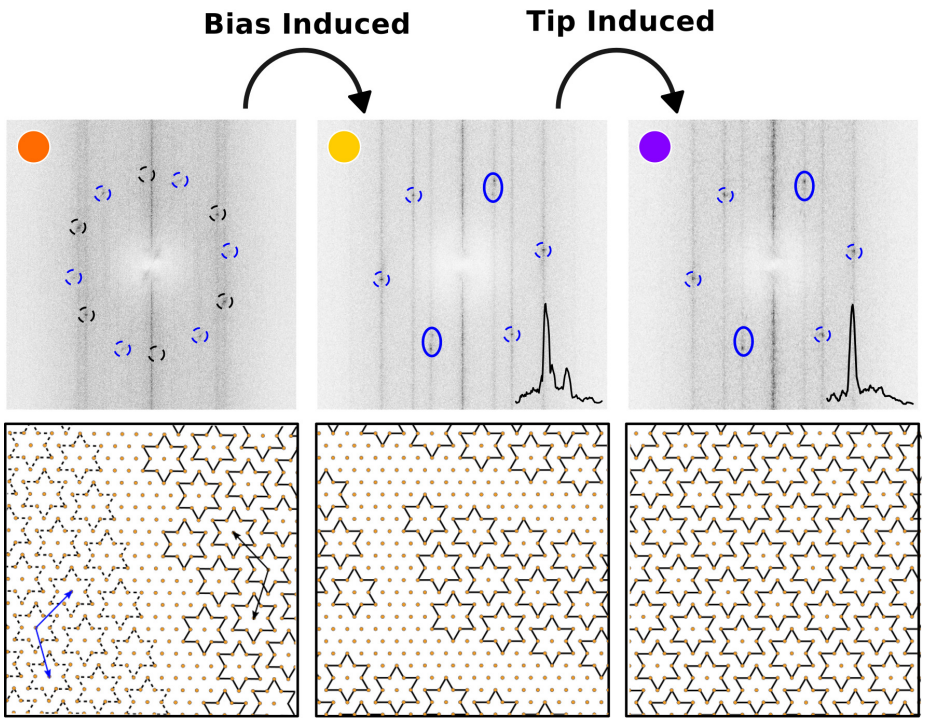

Figure 3.14: (Top) FFTs of the STM scans in Figure 3.12b, and of the final state following repeated rastering with the tip. The FFTs with colored dots in the top left hand corner correspond to the STM scans with the same colored dot. (Bottom) Schematics that demonstrate how the state is evolving. Initially the state consists of a mixture of α and β domains and thus 12 peaks are observed in the FFT. After electrical driving, only one orientation remains, with the state being dominated by the NC phase. The FFT now consists of the fundamental modes of a single orientation of the CDW with a visible satellite peak. Lastly, after continuous scanning with the tip, the NC region has been converted to the C phase. Consequently, in the FFT the satellite peak has now disappeared.

a mirror domain wall separating an NC-like region of the CDW in the α orientation from a C-like region of the CDW in the β orientation. Consequently, both chiral modes are observed in the FFT of the image, resulting in the appearance of 12 peaks (Figure 3.10). After electrically driving the sample, the NC region dominates the image and thus the FFT now only contains 6 peaks, representing a single orientation of the CDW. Consistent with the prevalence of the NC-like region in the image, a satellite peak in the FFT is visible. As the area is continuously scanned, the NC region is gradually converted into C, and thus in the FFT of the final scan the satellite peak is no longer present.

3.5 Conclusion

We have demonstrated the electrical behaviour of ultrathin flakes of 1T-TaS_2. As 1T-TaS_2 is thinned towards the 2D limit, the hysteresis region of the NC-C transition broadens, with the transition occurring in stepwise fashion. Within the hysteresis region, the material can be driven to states possessing a resistivity between that of the C and NC states by applying lateral electrical signals. However, the material is not able to be driven entirely to the C phase, with the resistivity eventually reaching a maximum at an intermediate value. We found that by using an AC voltage, the resistivity saturation point was reached with less stochastic variability and at a lower applied voltage compared to when using a DC signal. In addition to driving the flake towards the C phase, driving back towards the low-resistance state can be accomplished by continuing to ramp up the voltage signal until a transition is observed. By using an AC signal to drive the material to the saturation point, and then a DC voltage to drive the material back towards the NC phase, we were able to repeatedly toggle between the intermediate resistance state and the low-resistance state.

Using the device design outlined in Chapter 2 of this thesis, we then measured the topography of exfoliated ultrathin flakes of 1T-TaS_2. We focussed on the temperature range of the NC-C hysteresis region, with the goal of imaging both the equilibrium CDW phases present, as well as the non-equilibrium phases accessing by applying an electric field. Rather than constituting a novel phase with an electronic structure different than the bulk equilibrium phases, we found ultrathin 1T-TaS_2 to exist in a state with electronic inhomogeneity. We imaged two distinct region types, which could be differentiated based upon whether they contained discommensurations reminiscent of those observed in the NC phase. After applying an electrical signal to this inhomogeneous state, we were able to measure the rearrangement of these domains. Additionally, changes in the state were also observed after repeated scanning with the STM tip. In both cases, these results demonstrate the ability to manipulate, and measure in real-space, electronic phase domains

at the nanoscale. In Chapter 4 of this theory we apply a model of phase separation to qualitative relate this manipulation of an inhomogeneous electronic state to the bulk electrical properties observed in ultrathin 1T-TaS_2.

Chapter 4

Phase separation in ultrathin 1 T−TaS_2

4.1 Introduction

Given the temperature at which the STM measurements in Chapter 3 were performed, and the similarities between the features observed and the known, characteristic structure of the phases present in bulk 1T-TaS_2, we believe the data indicates that within the NC-C hysteresis region of the phase diagram, the ultrathin flakes studied in this thesis are in a phase separated state. In general, phase separation and electronic inhomogeneity at both the nanoscale and the mesoscale is often a consequence of the complexity within a system [95–97]. Hysteresis in an observable through a first-order phase transition is typically indicative of the presence of superheating/supercooling [98]. Within the hysteresis region, the two phases involved in the transition are nearly degenerate and can coexist, forming a phase separated state characterized by a complex microstructure consisting of intertwined domains of the ground state of the system and the nearly degenerate metastable state. The data presented in Figure 3.7 and Figure 3.9 provides evidence for the presence of phase separation in ultrathin 1T-TaS2, with the electronic state imaged comprising irregularly shaped domains of C-like and NC-like regions of a size on the order of hundreds of nanometers.

Additional evidence for the presence of phase separation in ultrathin 1T-TaS_2 can be found in the thickness dependent resistivity of the material over the same temperature range. As described in Section 3.2, the NC-C transition region in ultrathin flakes exhibits different characteristics compared to what is observed in bulk samples. When the material

is thinned, stepwise transitions appear, and in the 2D limit the discontinuous jump in the resistivity is not observed at all [31]. This result is potentially consistent with a disorder-induced phase separated state [80], and suggests that ultrathin flakes of 1T-TaS_2 cooled below the NC-C transition temperature are prone to spatial inhomogeneity..

Considering the evidence for the existence of phase separation in 1T-TaS_2, in this chapter we delve deeper into the dynamics of this process. To understand the conditions that give rise to phase separation we first discuss the thermodynamics of a system with a free energy profile that consists of a double well potential, using the liquid-vapour phase transition of CO_2 as an illustrative example. After reviewing the fundamentals of phase separation, we develop and apply a model of phase separation to elucidate the mechanism behind the bidirectional resistance switching discussed in Chapter 3 of this thesis.

4.2 Phase separation: Nucleation and spinodal decomposition

The coexistence of two phases is not uncommon in first-order phase transitions. There can exist a region within the phase diagram of a system where a heterogeneous state consisting of domains of multiple phases is energetically more stable compared to a homogeneous phase. A common example is the liquid-vapour phase transition in CO_2, a system whose free energy, $F(T, V, N)$, consists of a double well potential. In such a system, there exists two local minima corresponding to two distinct homogeneous phases. The free energy of the heterogeneous state, F_{het}, defined as a mixture of the two homogeneous phases, is given by:

$$F_{het} = c_I F_I + c_{II} F_{II}. \tag{4.1}$$

By the lever rule, used to determine the fraction of each phase in a binary equilibrium state,

$$c_I = \frac{V_{II} - V}{V_{II} - V_I}, \qquad c_{II} = \frac{V - V_I}{V_{II} - V_I}, \tag{4.2}$$

and thus the free energy of the heterogeneous state is equal to

$$F_{het} = \frac{V_{II} - V}{V_{II} - V_I} F_I + \frac{V - V_I}{V_{II} - V_I} F_{II}. \tag{4.3}$$

Equation 4.3 describes the line that is tangent to both $F(T, V_I, N)$ and $F(T, V_{II}, N)$. Figure 4.1 presents the free energy of CO_2 where the dashed line represents the free energy

of the heterogeneous state.[1]

The segment of the curve where the heterogeneous state is the free energy minimum is defined as the binodal region, and is given by the total shaded area in Figure 4.1. In this region, the homogeneous phase is not necessarily unstable, but rather is metastable. A metastable phase is unstable to finite perturbations, perturbations large enough to eclipse the energy barrier between the metastable local minimum and the ground state of the system, but is potentially stable to infinitesimal changes. The area of the curve shaded in blue defines the spinodal region, the subset of the binodal region where the system is unstable to even infinitesimal changes in a state variable. This region has a negative curvature in $F(T,V,N)$,

$$\frac{\partial^2 F(T,V,N)}{\partial V^2} < 0 \tag{4.7}$$

Figure 4.2 schematically demonstrates the evolution of the free energy of 1T-TaS_2 specifically as temperature is varied. When the system is cooled, two effects are observed: the C phase becomes the ground state, and the lattice parameters of the NC phase are modified (see dotted line in Figure 4.2). While the C phase is the new global minimum, the NC state is still metastable with the existence of an energy barrier separating NC phase from the C phase. The free energy of the system is also modified as the material is thinned. As 1T-TaS_2 is exfoliated to the 2D limit, the barrier separating the NC phase from the C phase increases. Experimentally, this manifests in the broadening of the NC-C hysteresis region. The picture described above only considers the existence of the homogeneous NC and C phases, but there is nothing that precludes the possibility for a phase separated

[1]The free energy CO_2 is modelled by the van der Waals equation of state, given in its extensive form as,

$$\left(p + \frac{N^2 a}{V^2}\right)(V - Nb) = NRT, \tag{4.4}$$

where a and b are constants that can be interpreted as the average interaction between gas particles and the volume excluded by a mole of particles respectively. The Helmholtz free energy can then be written as,

$$F(T,V,N) = -Nk_BT\left[1 + log\frac{(V - Nb')\,T^{3/2}}{N}\right] - \frac{a'N^2}{V}, \tag{4.5}$$

where the reduced form of the constants a and b, a' and b' have been used. Simplifying Equation 4.5 by making the volume and free energy intensive, and by using the reduced units $\tilde{v} = v/v_c$, $\tilde{T} = T/T_c$, and $\tilde{f} = f/k_BT_c$, we arrive at the form of the free energy plotted in Figure 4.1,

$$\tilde{f}\left(\tilde{T},\tilde{v}\right) = -\tilde{T}\left[1 + \log\left(\tilde{v} - 1/3\right)\tilde{T}^{3/2}\right] - \frac{9}{8\tilde{v}}. \tag{4.6}$$

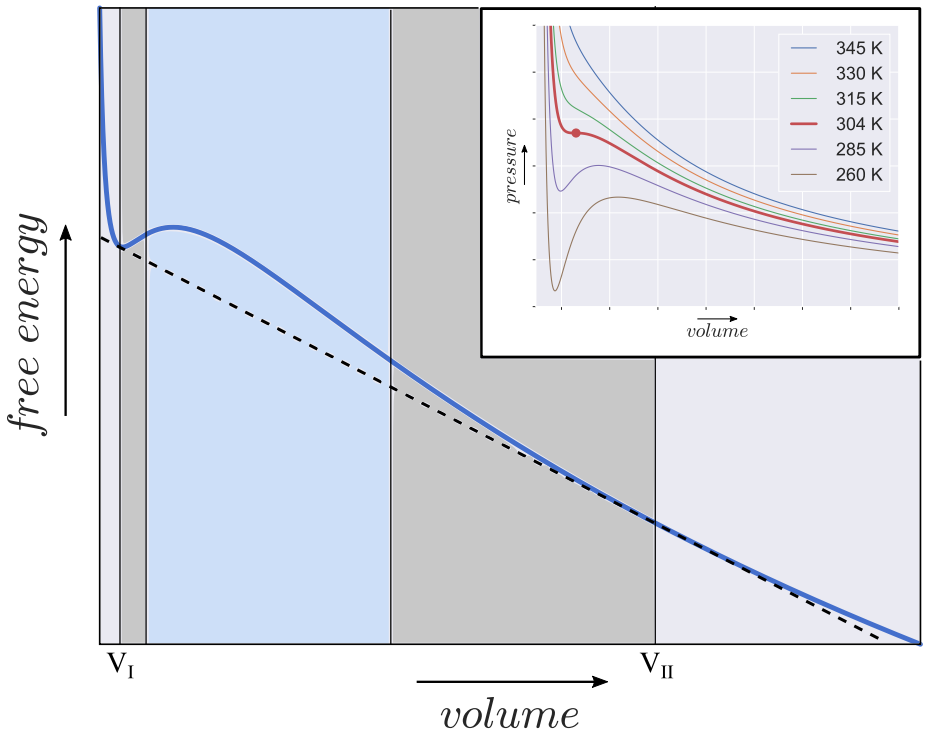

Figure 4.1: The free energy CO_2 as given by the van der Waals equation of state. The inset presents different isotherms of CO_2 around the critical temperature of the liquid-vapour phase transition ($\sim$ 304 K). The isotherms were modelled using the van der Waals equation of state (see Equation 4.4) and the isotherm corresponding to the critical temperature is given by the thick red line.

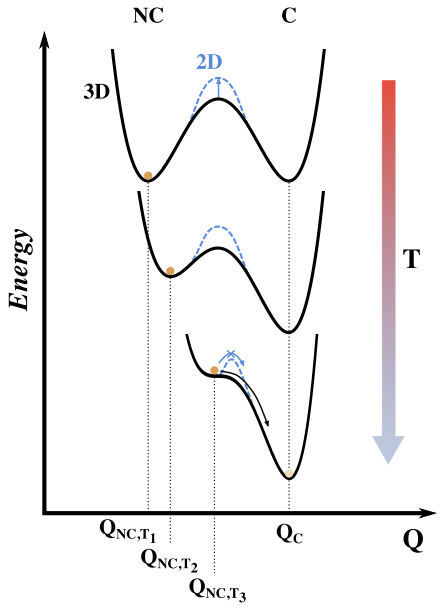

Figure 4.2: A schematic demonstrating the change in the free energy of 1T-TaS_2 as the material is thinned. Thinning 1T-TaS_2 causes the barrier between the NC and C phases to increase, enhancing the metastability of the NC phase as the temperature is cooled.

state to exist.

The coexistence of different phases has been observed in systems such as binary alloys and block copolymers. When a system is rapidly quenched below a critical temperature into a region of the phase diagram with competing phases, those phases form a phase separated state. Two mechanisms for the emergence of phase separation are commonly discussed: nucleation and spinodal decomposition. Nucleation describes the growth of droplets of one phase within another due to large fluctuations in the value of the characteristic order parameter that describes the phase. Conversely, spinodal decomposition, as the name implies, concerns the instability of the homogeneous phase to infinitessimal long-wavelength fluctuations in the order parameter.

Nucleation is often discussed as the competition between the energy benefit obtained from the increase in the volume of a domain, and the cost associated with the formation of a domain wall. The energetics of nucleation are captured by comparing the surface energy cost associated with the presence of a domain wall, and the energy benefit of the increase in the volume of the domain as it grows. The difference in free energy between the system with one droplet and the system with zero droplets is phenomenologically given by:

$$\Delta F\left(R\right) = 4\pi\sigma R^2 - \frac{4}{3}\pi\epsilon R^3 \tag{4.8}$$

where R is the radius of the droplet, and σ and ϵ are the surface free energy per unit area and the bulk free energy per unit volume respectively. There exists a critical radius, $R_C = \sigma/\epsilon$ at which point this energy difference is maximized. For droplets with $R < R_C$ the surface free energy cost dominates, and consequently the droplet would shrink and disappear. However, for $R > R_C$ the size of the droplet increases.

The value of the parameters σ and ϵ depend upon the state of the system. In the spinodal decomposition regime, σ vanishes, and thus the homogeneous state with no droplets is unstable towards even infinitesimal fluctuations in the order parameter. Based on the relationship between these parameters we can construct an cartoon phase diagram schematic, as depicted in Figure 4.3. In the grey region between the coexistence curve and the spinodal, the homogeneous phase is metastable, and with large enough fluctuations, nucleation can occur. When the system is quenched from T_i to T_q in the blue region, under the spinodal curve, the homogeneous phase is unstable to even infinitessimal fluctuations, resulting in spinodal decomposition into a microstructure with concentrations C_α and C_β of the two constituent phases. We define an order parameter based on the concentration of each constituent phase

$$\psi\left(\boldsymbol{r}, t\right) = c\left(\boldsymbol{r}, t\right) - c_0, \tag{4.9}$$

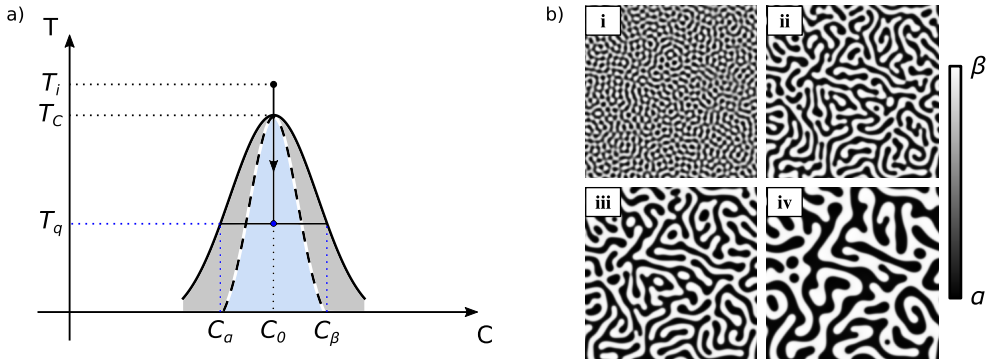

Figure 4.3: (a) Schematic of the phase diagram of a material that undergoes phase separation. The temperature of the system is plotted along the y-axis while the concentration of the constituent phases is plotted along the x-axis. The coexistence curve is represented by the solid line, while the spinodal curve is represented by the dashed line. (b) The evolution of a microstructure through phase separation. The dark regions represent one constituent phase, while the light regions represent the other phase. Coarsening of the different regions occurs after the initial formation of a phase separated state.

where $c(\boldsymbol{r}, t)$ is the concentration of one of the phases at time t, and c_0 is the average concentration over the entire system. This order parameter is useful for characterizing the state of the system and is useful for defining the free energy functional of the system.

4.2.1 The Cahn-Hilliard Equation

Figure4.3b presents a schematic of the development of a microstructure, comprising intertwined domains of the constituent phases. The dynamics describing the formation of this microstructure were simulated using the Cahn-Hilliard equation [99, 100]. The Cahn-Hilliard free energy functional is of the form:

$$F\{\psi(\boldsymbol{r})\} = \int d^d\boldsymbol{r} \left\{ \frac{1}{2} (\nabla\psi)^2 + f(\psi(\boldsymbol{r})) \right\}. \tag{4.10}$$

The gradient term corresponds to the energy cost associated with having changes in the phase concentration, i.e. domains, while $f(\psi)$ represents the bulk free energy per unit volume of a homogeneous system.

The dynamics of the order parameter are characterized by diffusion in a chemical po-

tential gradient, where it is assumed that material is conserved,

$$\frac{\partial \psi}{\partial t} + \nabla \cdot \boldsymbol{j} = 0. \tag{4.11}$$

The current, j, is defined phenomenologically as,

$$\boldsymbol{j} = -M \nabla \frac{\partial F}{\partial \psi \left(\boldsymbol{r} \right)}, \tag{4.12}$$

where the parameter M represents mobility. Plugging 4.12 into 4.11 gives the *Cahn-Hilliard equation*:

$$\frac{\partial \psi}{\partial t} = M \nabla^2 \left[\frac{\partial f}{\partial \psi} - \nabla^2 \psi \right]. \tag{4.13}$$

Figure 4.4a presents different examples of phase separated states, simulated using the Cahn-Hilliard equation, each starting from a different initial average concentration. In these simulations, the two-dimensional system is initialized with the value of the order parameter being given by the average concentration c_0, and then random fluctuations about the mean are generated at random lattice points. The system is then allowed to evolve according to Equation 4.13. What is observed is the separation of the system into a state comprised entirely of the two constituent domains, the two minima in the free energy diagram, followed by coarsening of the different regions (see Figure 4.3b). The initial concentration value fixes the final concentrations of each domain type. Depending on these volume fractions, the resulting microstructure displays different features. With equal amounts of each domain type, the microstructure consists of an intertwined pattern. As the volume fraction of one of the phases is increased, the final microstructure contains droplets of the phase with the smaller volume fraction dispersed throughout the other domain type.

4.2.2 The $Y - \nabla$ transformation

To relate the geometric structure of a given phase separated state to the bulk resistivity of the system, we calculate a resistance for each microstructure by discretizing the image into a 2D resistor network, and applying the algorithm outlined in Frank and Lobb (1988). [102]. The building blocks of the algorithm consists of the standard transformations for determining equivalent conductances of multiple resistors in series and multiple resistors

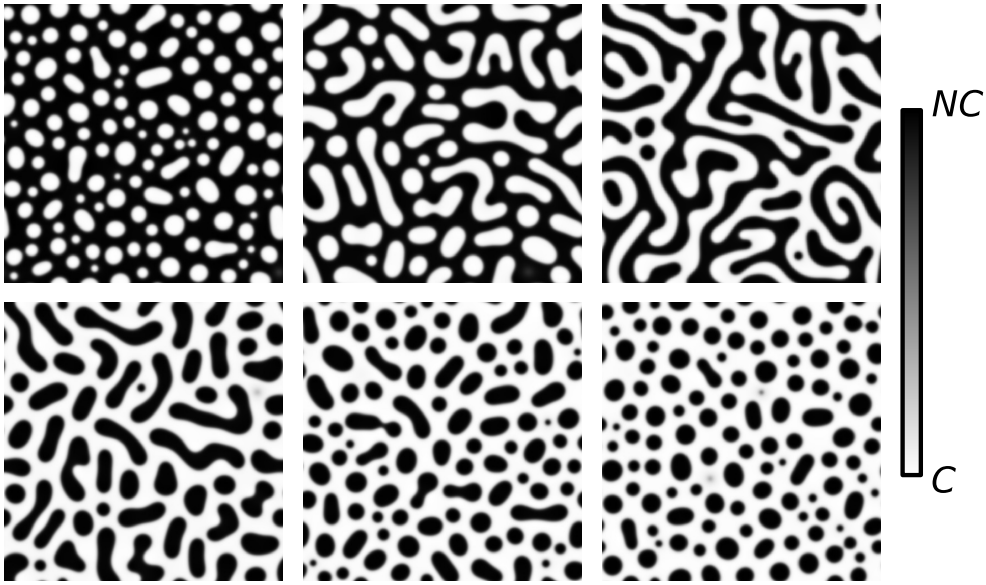

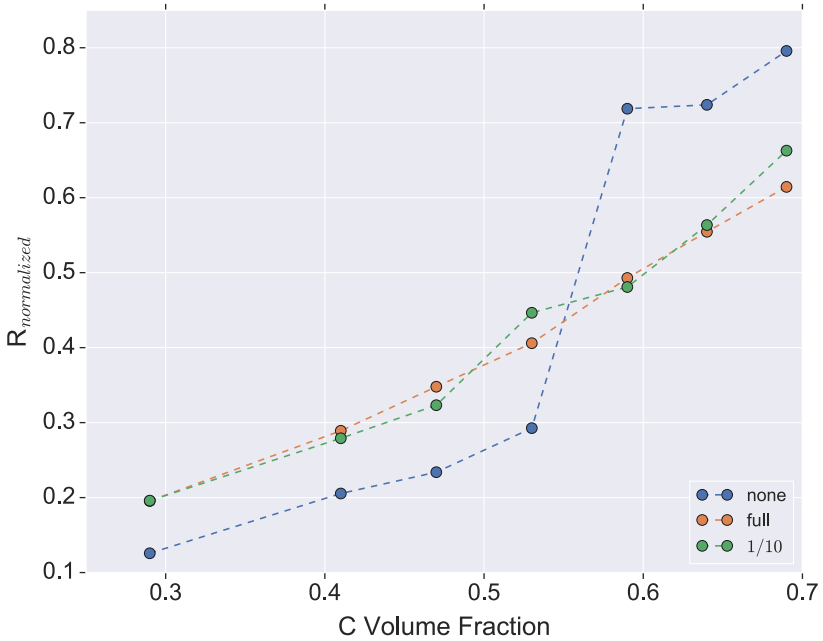

Figure 4.4: (a) Microstructures formed at various starting C phase concentrations. The structures were generated using the materials knowledge system package in Python [101]. (b) The resistances calculated for the different microstructures generated. The three curves correspond to three different methods for defining contact electrodes (see main text).

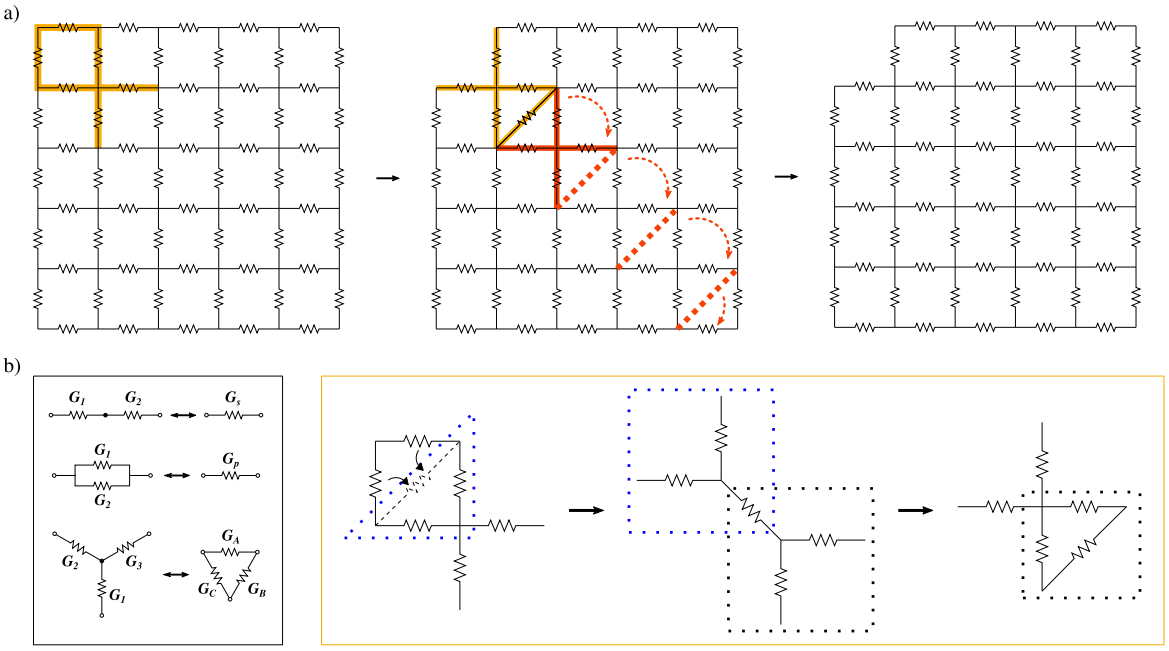

Figure 4.5: (a) The main steps in the algorithm operating piecewise on a 2D resistor network to calculate an equivalent resistance [102]. Each step of the algorithm uses two instances of the $Y-\nabla$ transformation (see orange box in (b)). (b) The transformations used to find an equivalent resistance for a 2D resistor network. (Black box) (Top) Equivalent resistance for two resistors in series. (Middle) Equivalent resistance for two resistors in parallel (Bottom) The $Y-\nabla$ transformation that allows for the deconstruction of a 2D resistor network. (Orange box) The sequence of steps repeated to deconstruct a 2D resistor network.

in parallel, as well as the $Y - \nabla$ transformation (Figure 4.5b black box):

$$Series\ resistors: G_s = \frac{G_1 G_2}{G_1 + G_2} \tag{4.14}$$

$$Parallel\ resistors: G_p = G_1 + G_2 \tag{4.15}$$

$$Y\text{-}\nabla: \begin{cases} G_1 = G_B G_C \left[\frac{1}{G_A} + \frac{1}{G_B} + \frac{1}{G_C}\right] \\ G_2 = G_C G_A \left[\frac{1}{G_A} + \frac{1}{G_B} + \frac{1}{G_C}\right] \\ G_3 = G_A G_B \left[\frac{1}{G_A} + \frac{1}{G_B} + \frac{1}{G_C}\right] \end{cases} \tag{4.16}$$

Continuously applying the transformation outlined in the orange box, as demonstrated in Figure 4.5a, an equivalent resistance is determined for a given 2D resistor network.

With the algorithm defined as in Figure 4.5a, an equivalent resistance is found assuming contacts exist at the bottom left and top right node. Depending on the size of the simulation, finite size effects could play a part in determining the resistance of the network, with the result being overly sensitive to the arrangement of the microstructure directly adjacent to the contacts. The consequences of these effects are visible in Figure 4.4b, where the different traces correspond to three different ways of defining the contacts. For the case of the blue trace, the contacts are defined as discussed above, the resistance is determined from the bottom left node of the network to the top right. In the case of the orange and green traces, contacts are defined to be blocks of nodes as opposed to the single corner node, with the former comprising the entire leftmost and rightmost columns of nodes, and the latter consisting of a block of 1/10 of the nodes. While finite size effects are undesirable, they describe a realistic scenario potentially observed with the ultrathin samples measured earlier in this chapter. Essentially these effects would correspond to a "weak link" contact description, where the ultrathin flakes are not contacted uniformly. Ultimately, for the simulations performed later in this chapter, the definition of the contacts is largely irrelevant, as rather than comparing unrelated microstructures, the bulk resistances are calculated for a continuously evolving phase separated state, and thus the changes in resistance are less dramatic.

4.3 Time-dependent Ginzburg-Landau theory

With the Cahn-Hilliard equation it is assumed that the order parameter is conserved. Consequently, phase separation emerges naturally from the parameters of the problem. A

more accurate model would allow for the order parameter to vary, such as time-dependent Ginzburg-Landau theory (TDGL) [103]. The governing equation in TDGL is,

$$\frac{\partial u}{\partial t} = -\Gamma \frac{\partial F}{\partial u} \tag{4.17}$$

where Γ is a damping parameter, u is the order parameter, and F is a Landau free energy representative of the system being modelled. Starting from a Landau free energy F with minima at $u = 0$ (the C phase) and $u = 1$ (the NC phase), we introduce the phenomenological parameter f to tune the stability of the C phase relative to the NC phase by tilting the free energy potential:

$$F(u) = \frac{a^2}{2}u^2(1-u)^2 + fu^2(3-2u) + \frac{1}{2}(\nabla u)^2, \tag{4.18}$$

The model is initialized to a random, inhomogeneous microstructure and the system is then allowed to evolve according to Equation 4.17. Without introducing disorder, the system will form either the homogeneous C or NC phase, depending on the value of the tilt parameter, f. However, if disorder is introduced into the model in the form of pinning centres, impurity sites where the order parameter is reset to $u = 1$ at the end of each time step, then a phase separated state is generated. In the quasi-2D limit, defect sites of this kind would play a significant role in determining the properties of 1T-TaS_2, compared to in bulk samples of the material [31]. Under these conditions, a phase separated structure containing intertwined C and NC phase domains is generated. The NC domains are situated around clusters of pinning centers, and the relative volume fractions of the two phases depend on both f and the total number of impurity sites introduced (Figure 4.6a).

4.4 Bidirectional resistance switching of a system in a phase separated state

The data collected in this work does not preclude the possibility that the system possesses symmetry not probed by the STM experiments above, or that the driving of the inhomogeneous electronic state involves a continuous evolution towards the C phase. An example of such an evolution would be one that proceeds through a modification of the domain period in NC-like regions with the creation or annihilation of domain walls. However, many of the features observed in the bidirectional resistance switching of ultrathin 1T-TaS_2 can be explained in the context of the system being in a phase separated state. For a sample of

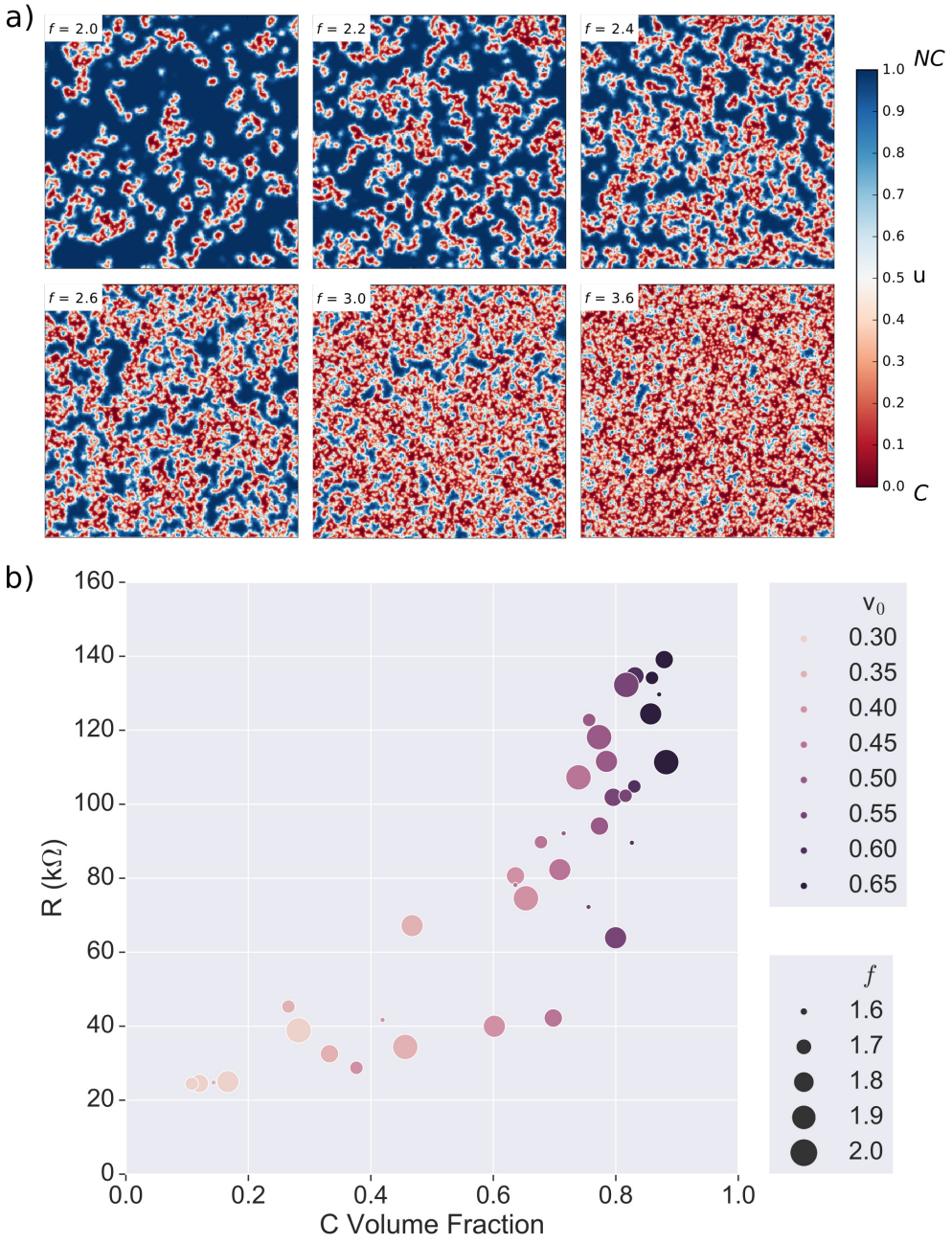

Figure 4.6: (a) Microstructures formed at various values of the tilting parameter f. (b) The resistances calculated for microstructures generated from different values of f and initial C phase volume fractions (v_0).

1T-TaS_2 in a phase separated state, the bulk resistivity is determined by the arrangement of the NC-like and C-like domains and their relative volume fractions, with the initial volume fractions being set by the temperature of the sample. The bidirectional resistance switching emerges from the competition between the NC and C phases. It is observed that an applied electric field modifies the balance of competition between the two states, stabilizing the C phase relative to the NC phase up to some critical value, at which point breakdown of the C phase occurs. The fundamental microscopic mechanism that couples the applied electric field to the observed charge orders remains an open question, with a number of possibilities put forward in the literature. Regarding the transition of the C phase to the NC phase, Joule heating [30], carrier-driven breakdown [87], and a modification of the interlayer stacking [42, 43] have all been proposed as potential mechanisms, while Patel et al. (2020), [86], suggested that conversion of the NC phase to the C phase is facilitated by the stabilization of the C phase due to its greater polarizability.

Regardless of the underlying mechanism involved, starting from when the sample is in the low-resistance state, one can imagine the driving proceeding through different stages, each depending upon the voltage drop across the flake. Given the non-uniformity of the charge ordering in a phase separated state, the voltage drop varies spatially across the sample. When the flake is in the low-resistance state, there exists a percolative NC path, and the majority of the applied voltage drops across the NC region spanning the flake. The applied electric field stabilizes the C phase relative to the NC phase, causing the C state volume fraction to increase, until the percolative NC path no longer exists, and the resistance subsequently increases. As the volume fraction of the C phase continues to grow, less of the applied voltage drops across NC domains. Consequently, the driving saturates at a certain intermediate C volume fraction, at the point when the majority of the voltage drops across C domains. Once the resistance saturates, as the voltage is increased, current flow through the C domains increases as well. At a certain critical current, breakdown of the C domains occurs, and the metallic percolative path is again formed, causing the resistance to drop. Once this breakdown occurs, the voltage again drops across the NC domains, and consequently it is possible to observe a transition back into a more resistive state. This picture is corroborated by the results in the literature mentioned in Section 3.2 and discussed in Figure 3.4, where the authors were unable to drive the sample entirely back to the low-resistance state.

Figure 4.7 schematically represents the evolution of the inhomogeneous state described above. As in Section 4.2.1 on the Cahn-Hilliard equation, the microstructure is discretized into a 2D resistor network with NC and C nodes. Initially, the system is considered to be in a state with a relatively small C phase volume fraction, as depicted in Figure 4.7a. Due to the coexistence of the C and NC phase domains, the voltage applied across the

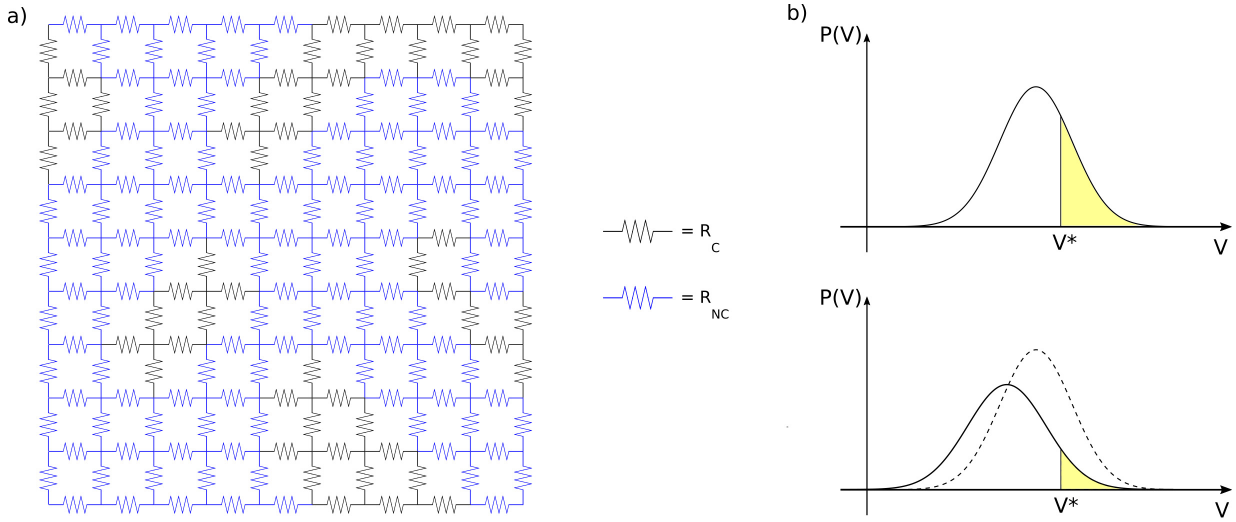

Figure 4.7: (a) The system is discretized and modeled as a 2D resistor network. The resistance of the microstructure is calculated using the algorithm pictorially represented in Figure 4.5. (b) The voltage dropping across the NC nodes will follow some distribution $P(V)$ (top). NC nodes with a value beyond the threshold value $V*$ are converted to C, changing the distribution of the voltage drops (bottom).

sample will not drop homogeneously but will depend on the geometric arrangement of the microstructure. Consequently, the voltage drop across the complete set of NC regions will have some distribution $P(V)$. As a voltage is applied to the sample, the voltage drop across some of the NC nodes exceeds a certain critical value $V*$ resulting in those NC nodes in the resistor network to become C. When this conversion occurs the distribution of the voltage across the NC nodes changes (Figure 4.7b). Eventually, the voltage drop across none of the NC nodes will exceed $V*$, and the system will have reached an equilibrium state independent of V.

This evolution of the inhomogeneous state is approximated in the simulations by first introducing a limiting value $u_{lim} = 0.5$ below which the order parameter is depinned from an impurity site, meaning it is not reset to $u = 1$ at the end of each time step. With this modification, the final microstructure generated from the time evolution of the system becomes dependent on the initial C phase volume fraction, v_0, in addition to the tilting parameter and the number of pinning centers. For small values of v_0 ($v_0 \leq 0.40$), the system evolves to a percolated NC phase, with a resistivity comparable to that of the homogeneous NC phase, while for larger v_0, the system goes to the C phase. This result is demonstrated in Figure 4.6b, where the resistance of the generated microstructure is calculated for different sets of values of v_0 and f. The driving model is completed by adding a second set of threshold parameters, f_c and u_c, to control the conversion of C nodes to NC nodes. When $f = f_c$, nodes where the order parameter is greater than u_c are converted to $u = 1$, the NC phase.

Utilizing the model described above, we qualitatively reproduce the main features observed during the electrical driving. The linear voltage sweep is simulated by a linear sweep of f. The stabilization of the C phase relative to the NC phase corresponds to an increase in the parameter f. Figure 4.8b illustrates a simulated sweep starting from a microstructure that is predominantly in the NC phase. Examples of the simulated microstructures generated during the sweep are given in Figure 4.8d, panels (i-vii). As f is increased, some of the pinning centers are depinned, causing the volume fraction of the C phase (orange domains) in Figure 4.8d) to increase, and resulting in an increase in the bulk resistance. When f is swept back to its initial value, the state the system returns to is different than its initial state, as the steady-state solution depends on both the value of f and on the history of the material. Figure 4.8c demonstrates a sweep starting from the predominantly C phase from Figure 4.8d, panel (vii). Once f is increased to f_c, NC domains form around clusters of pinning centres (Figure 4.8d panel (ix)). The state of the system when f is returned to its initial value has a significantly larger volume fraction of NC regions compared to the initial microstructure, and thus a lower resistance, demonstrating the bistability of the C and NC phase mixture.

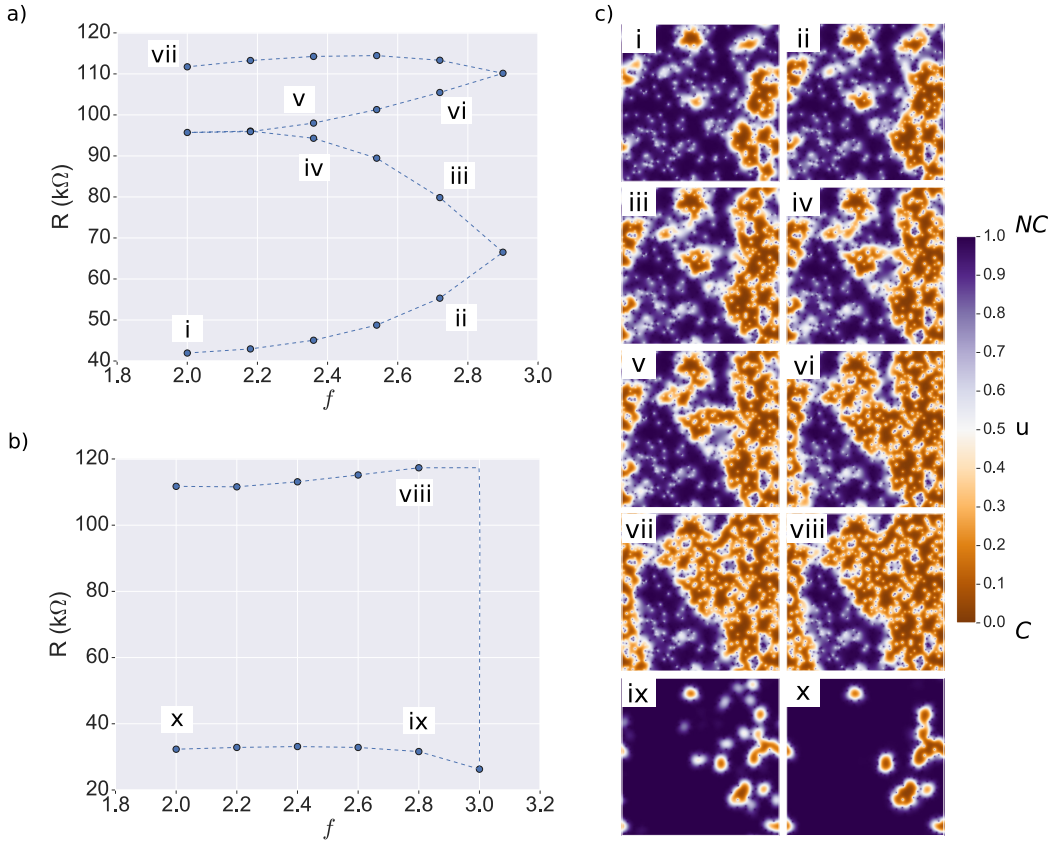

Figure 4.8: (a) A simulated electrical driving sweep using the TDGL model described in the text. Starting from a state predominantly in the NC phase, f is increased, resulting in the conversion of some NC regions to C domains. In the simulated sweep f plays the role of the applied voltage in the electrical driving. The Roman numerals labelling the points in the sweep refer to the corresponding microstructures in (c). (b) Continuing the sweep from (a), starting from a microstructure that is predominantly C, f is swept until $f = f_c$, at which point C regions are converted to NC domains that form around clusters of pinning centers. (c) Examples of the simulated microstructures generated in sweeps (a) and (b). $u = 0$ represents the C phase, while $u = 1$ is the NC phase.

As evidenced in Figure 4.8b, multiple sweeps to the same voltage value will continuously manipulate the state of the material. Assuming the maximum voltage set is less than the voltage at which breakdown of the C domains occurs, the material will be driven to some intermediate state with a higher resistance compared to the initial state. With this consideration in mind, applying a lateral AC bias across the sample will drive the material more efficiently than a DC bias, as when using an AC signal multiple sweeps are performed. As previously discussed, Figure 3.3 demonstrates this behavior. Using an AC bias, the sample is driven to the saturation resistance level more directly, and at lower voltages compared to when a DC bias is used. Whether there exists an alternative explanation for the enhancement observed when using an AC voltage, one that is based upon the underlying microscopic mechanism that facilitates the electrical driving, is beyond the scope of this work.

4.5 Conclusion

In summary, a model of phase separation has been used to explore the connections between the electronic inhomogeneity present in ultrathin 1T-TaS_2 and the bulk resistivity of the sample. Starting with a spatially varying order parameter representing the CDW state of the material, and a double well Landau free energy, we allowed the system to evolve according to time-dependent Ginzburg Landau theory. Without introducing disorder, only the homogeneous C or NC phase was realized. However, after incorporating disorder into the system, in the form of pinning centres fixed to the NC phase, a phase separated state was obtained. This state possessed inhomogeneity with distinct regions of the two constituent phases corresponding to the two minima in the double well potential.

To simulate the electrical driving described in Chapter 3, the model was extended by incorporating ideas from percolation theory. In the electrical driving, it is observed that an electric field stabilizes the C phase relative to the NC phase, up until a critical value at which point breakdown of the NC phase occurs. To simulate this behaviour, a phenomenological parameter, f, was introduced to control the tilt of the free energy potential, and thus the relative energies of the two minima. Additional critical parameters were used to define when the pinning centres of the order parameter would become unpinned, and at what critical electrical field, breakdown of the NC phase to the C phase would occur. The voltage signals used to manipulate the inhomogeneous state were then simulated by sweeping the value of f. Employing this model, percolative like behaviour was observed. When a NC path across the sample existed, the resistivity measured would be comparable to the low-resistance state, as the NC phase was converted to the C phase, eventually the

percolative path was disrupted resulting in a jump in the resistance. In this fashion, the model qualitatively reproduced the multistability of different states and the accessing of states with resistivities that lie between that of the low and high-resistance phases.

The model described above does not explicitly allow for the rearrangement of the NC and C domains as the location of the pinning centres essentially fixes the geometric arrangement of the regions. Thermal noise and Joule heating effects stemming from the flow of charge carriers are not included, but would result in a more complete picture that might allow for the possibility of the rearrangement of the microstructure. Despite this limitation, the model does recreate many of the essential features of the observed driving. These results highlight the importance of considering phase separation when probing the origin of bulk properties. For example, many of the characteristics of the emergent bidirectional resistance switching elucidated in this chapter, can be explained when considering the system to be originating in a phase separated state.

Chapter 5

Summary and Outlook

In many respects, exfoliated materials in the 2D limit are ideal systems to image with scanning tunneling microscopy (STM). Such materials are naturally atomically flat, and depending on the specific material being studied, can possess relatively unreactive surfaces. The two primary challenges associated with imaging such flakes is the difficulty navigating to a flake of interest in the STM and the presence of contamination introduced during the exfoliation procedure. By taking advantage of the optical contrast between different materials, or films of the same material but with different thicknesses, we were able to design a device geometry that allowed for the facile location of flakes with micron sized lateral dimensions. With the first iteration of devices described in Section 2.4.2, where a gold pad is fabricated with a hole in the centre across which a flake is transferred, the flake could be located within minutes of approaching the surface. Furthermore, the work in this thesis demonstrates that exfoliated samples are sufficiently clear of contamination to be probed with STM after minimal heating. Although we were unsuccessful maintaining a tip suitable for scanning tunneling spectroscopy (STS) measurements, it was possible to follow paths to regions of interests that were sufficiently free of contamination that the regions could be imaged successfully. The techniques described in this thesis for imaging 1T-TaS_2 can be applied to the measurement of any exfoliated, conductive 2D material.

Within the NC-C hysteresis region of ultrathin 1T-TaS_2, electrical measurements reveal the presence of non-equilibrium phases with resistivities that lie between the values associated with the equilibrium C and NC phases. It has been suggested in the literature that these states represent novel phases present only in ultrathin flakes of the material and possess an electronic structure different than that of the equilibrium bulk phases. Using a device design that not only allowed for the navigation to specific regions of interest on a flake, but also enabled the measurement of the bulk electrical properties of the flake *in*

situ, we studied ultrathin flakes of 1T-TaS_2 in the hysteresis region of the NC-C phase transition with the goal of determining the electronic structure of these non-equilibrium states. Within the hysteresis region of the NC-C phase transition, we found ultrathin 1T-TaS_2 to exist in a state with electronic inhomogeneity. This inhomogeneous state contained distinct domains with features reminiscent of the bulk NC and C phases. The presence of electronic inhomogeneity in 1T-TaS_2 is indicative of the competition between different equilibrium states. The geometric arrangement of the constituent phases within the inhomogeneous state was found to be amenable to perturbation through the application of lateral electrical signals. Consequently, we were able to measure the evolution of the state as a function of applied electric field. The images collected demonstrate the ability to both observe and manipulate phase domains at the nanoscale. Further work would involve a more detailed mapping of the phase diagram of ultrathin 1T-TaS_2 than what was presented in this thesis, including a thickness dependent study. By capturing the full range of phases possible for flakes of increasing thicknesses, the role of stacking in 1T-TaS_2 could potentially be probed. One limitation of such a study would be that STM is ultimately a surface probe. Consequently, if the changes in the phase diagram can not be correlated with bulk properties of the material, then one can not be certain that the surface does not exhibit a phase distinct from that of the bulk material.

Inspired by the phase coexistence present in other correlated electronic systems, a model of phase separation was used to explore the possible connections between the electronic inhomogeneity present in 1T-TaS_2 and the bulk resistivity of the material. By attempting to correlate the STM data with the bulk electrical behaviour of ultrathin 1T-TaS_2, we endeavoured to address the limitation of STM described above. Starting from a Landau free energy representative of a double well potential, a phase separated state was realized by incorporating disorder in the form of pinning centres where the phase was fixed to the low-resistance NC state. These pinning centres can be interpreted as the discommensurations in the NC phase. After obtaining an inhomogeneous state, the evolution of the state with the application of an electric field was modelled based on some of the ideas of percolation theory. Many of the features observed in the electrical behaviour of ultrathin 1T-TaS_2 are reproduced with this simple model. In particular, the saturation of the resistance at an intermediate value less than the resistivity of the high-resistance C phase is explained. Furthermore, the multistability of microstructures with different volume fractions of the constituent phases at a given temperature is realized.

Both the electrical behaviour observed in ultrathin flakes of 1T-TaS_2, and the presence of inhomogeneity, are similar to that observed in perovskite manganites and other correlated materials, such as vanadium oxides [104–107], and doped Mott insulators [96]. All of these compounds are characterized by competing metallic and insulating phases that give

rise to mesoscopic structural inhomogeneity. The macroscopic behaviour in these systems is directly related to the inhomogeneity present at smaller length scales. While many of the fundamental characteristics observed in manganites, vanadium oxides and doped Mott insulators are similar, the nature of the phases comprising the inhomogeneous state, and the stimuli required to manipulate the different phases, vary depending upon the factors underlying the metal-insulator transition. Unlike in the correlated systems mentioned above, in the case of 1T-TaS_2, the competition exists specifically between distinct CDW phases. Further study is warranted in the NC-C transition temperature range to probe the nature of the inhomogeneous state of 1T-TaS_2 in greater detail. However, the results presented in this thesis emphasize the complexity in the phase diagram of 1T-TaS_2, and demonstrate the importance of understanding the characteristics of its phase competition morphologies in order to identify potential applications for this material.

References

(1) Walker, S. M.; Patel, T.; Okamoto, J.; Langenberg, D.; Bergeron, E. A.; Gao, J.; Lao, X.; Sun, Y. P.; Tsen, A. W.; Baugh, J. Observation and manipulation of a phase separated state in a charge density wave material. *Nano Letters* **2022**, *22*, 1929–1936.

(2) Datta, S., *Electronic transport in mesoscopic systems*; Cambridge University Press: 1997.

(3) Novoselov, K. S.; Geim, A. K.; Morozov, S. V.; Jiang, D.-e.; Zhang, Y.; Dubonos, S. V.; Grigorieva, I. V.; Firsov, A. A. Electric field effect in atomically thin carbon films. *Science* **2004**, *306*, 666–669.

(4) Novoselov, K. S.; Geim, A. K.; Morozov, S. V.; Jiang, D.; Katsnelson, M. I.; Grigorieva, I.; Dubonos, S.; Firsov; AA Two-dimensional gas of massless Dirac fermions in graphene. *Nature* **2005**, *438*, 197–200.

(5) Geim, A. K.; Novoselov, K. S. In *Nanoscience and Technology: A collection of reviews from Nature journals*; World Scientific: 2010, pp 11–19.

(6) Novoselov, K.; Mishchenko, o. A.; Carvalho, o. A.; Neto, A. C. 2D materials and van der Waals heterostructures. *Science* **2016**, *353*.

(7) Geim, A. K.; Grigorieva, I. V. Van der Waals heterostructures. *Nature* **2013**, *499*, 419–425.

(8) Dagotto, E. Complexity in strongly correlated electronic systems. *Science* **2005**, *309*, 257–262.

(9) Bednorz, J. G.; Müller, K. A. Possible high-T_c superconductivity in the Ba-La-Cu-O system. *Zeitschrift für Physik B Condensed Matter* **1986**, *64*, 189–193.

(10) Lang, K.; Madhavan, V.; Hoffman, J.; Hudson, E. W.; Eisaki, H.; Uchida, S.; Davis, J. Imaging the granular structure of high-T_c superconductivity in underdoped $Bi_2Sr_2CaCu_2O_{8+\delta}$. *Nature* **2002**, *415*, 412–416.

(11) Moreo, A.; Yunoki, S.; Dagotto, E. Phase separation scenario for manganese oxides and related materials. *Science* **1999**, *283*, 2034–2040.

(12) Goldenfeld, N.; Kadanoff, L. P. Simple lessons from complexity. *Science* **1999**, *284*, 87–89.

(13) Roy, S. B. First order magneto-structural phase transition and associated multifunctional properties in magnetic solids. *Journal of Physics: Condensed Matter* **2013**, *25*, 183201.

(14) Wilson, J. A.; Di Salvo, F.; Mahajan, S. Charge-density waves and superlattices in the metallic layered transition metal dichalcogenides. *Advances in Physics* **1975**, *24*, 117–201.

(15) Dardel, B.; Grioni, M.; Malterre, D.; Weibel, P.; Baer, Y.; Lévy, F. Temperature-dependent pseudogap and electron localization in 1T-TaS_2. *Physical Review B* **1992**, *45*, 1462.

(16) Dardel, B.; Grioni, M.; Malterre, D.; Weibel, P.; Baer, Y.; Lévy, F. Spectroscopic signatures of phase transitions in a charge-density-wave system: 1T-TaS_2. *Physical Review B* **1992**, *46*, 7407.

(17) Bak, P. Commensurate phases, incommensurate phases and the devil's staircase. *Reports on Progress in Physics* **1982**, *45*, 587.

(18) Rossnagel, K. On the origin of charge-density waves in select layered transition-metal dichalcogenides. *Journal of Physics: Condensed Matter* **2011**, *23*, 213001.

(19) Butler, C.; Yoshida, M.; Hanaguri, T.; Iwasa, Y. Mottness versus unit-cell doubling as the driver of the insulating state in 1T-TaS_2. *Nature Communications* **2020**, *11*, 1–6.

(20) Wang, Y.; Yao, W.; Xin, Z.; Han, T.; Wang, Z.; Chen, L.; Cai, C.; Li, Y.; Zhang, Y. Band insulator to Mott insulator transition in 1T-TaS_2. *Nature Communications* **2020**, *11*, 1–7.

(21) Von Witte, G.; Kißlinger, T.; Horstmann, J. G.; Rossnagel, K.; Schneider, M. A.; Ropers, C.; Hammer, L. Surface structure and stacking of the commensurate (13 x 13) R 13. 9 degrees charge density wave phase of 1T-TaS_2 (0001). *Physical Review B* **2019**, *100*, 155407.

(22) Ritschel, T.; Berger, H.; Geck, J. Stacking-driven gap formation in layered 1T-TaS_2. *Physical Review B* **2018**, *98*, 195134.

(23) Nakatsugawa, K.; Tanda, S.; Ikeda, T. N. Multivalley Free Energy Landscape and the Origin of Stripe and Quasi-Stripe CDW Structures in Monolayer MX_2 Compounds. *Scientific Reports* **2020**, *10*, 1–9.

(24) Grüner, G., *Density waves in solids*; CRC press: 2018.

(25) Chan, S.-K.; Heine, V. Spin density wave and soft phonon mode from nesting Fermi surfaces. *Journal of Physics F: Metal Physics* **1973**, *3*, 795.

(26) Johannes, M.; Mazin, I. Fermi surface nesting and the origin of charge density waves in metals. *Physical Review B* **2008**, *77*, 165135.

(27) Fröhlich, H. Electrons in lattice fields. *Advances in Physics* **1954**, *3*, 325–361.

(28) Momma, K.; Izumi, F. VESTA 3 for three-dimensional visualization of crystal, volumetric and morphology data. *Journal of Applied Crystallography* **2011**, *44*, 1272–1276.

(29) Fang, Y.; Pan, J.; He, J.; Luo, R.; Wang, D.; Che, X.; Bu, K.; Zhao, W.; Liu, P.; Mu, G., et al. Structure re-determination and superconductivity observation of bulk 1T-MoS_2. *Angewandte Chemie* **2018**, *130*, 1246–1249.

(30) Yoshida, M.; Suzuki, R.; Zhang, Y.; Nakano, M.; Iwasa, Y. Memristive phase switching in two-dimensional 1T-TaS_2 crystals. *Science Advances* **2015**, *1*, e1500606.

(31) Tsen, A. W.; Hovden, R.; Wang, D.; Kim, Y. D.; Okamoto, J.; Spoth, K. A.; Liu, Y.; Lu, W.; Sun, Y.; Hone, J. C.; Kourkoutis, L. F.; Kim, P.; Pasupathy, A. N. Structure and control of charge density waves in two-dimensional 1T-TaS_2. *Proceedings of the National Academy of Sciences* **2015**, *112*, 15054–15059.

(32) Yu, Y.; Yang, F.; Lu, X. F.; Yan, Y. J.; Cho, Y.-H.; Ma, L.; Niu, X.; Kim, S.; Son, Y.-W.; Feng, D.; Li, S.; Sang-Wook, C.; Chen, X. H.; Yuanbo, Z. Gate-tunable phase transitions in thin flakes of 1T-TaS_2. *Nature Nanotechnology* **2015**, *10*, 270–276.

(33) Ritschel, T.; Trinckauf, J.; Koepernik, K.; Büchner, B.; Zimmermann, M. v.; Berger, H.; Joe, Y.; Abbamonte, P.; Geck, J. Orbital textures and charge density waves in transition metal dichalcogenides. *Nature Physics* **2015**, *11*, 328–331.

(34) Fazekas, P.; Tosatti, E. Electrical, structural and magnetic properties of pure and doped 1T-TaS_2. *Philosophical Magazine B* **1979**, *39*, 229–244.

(35) Fazekas, P.; Tosatti, E. Charge carrier localization in pure and doped 1T-TaS_2. *Physica B+ C* **1980**, *99*, 183–187.

(36) Whangbo, M. H.; Canadell, E. Analogies between the concepts of molecular chemistry and solid-state physics concerning structural instabilities. Electronic origin of the structural modulations in layered transition metal dichalcogenides. *Journal of the American Chemical Society* **1992**, *114*, 9587–9600.

(37) Smith, N.; Kevan, S.; DiSalvo, F. Band structures of the layer compounds 1T-TaS_2 and 2H-$TaSe_2$ in the presence of commensurate charge-density waves. *Journal of Physics C: Solid State Physics* **1985**, *18*, 3175.

(38) Kim, J.-J.; Yamaguchi, W.; Hasegawa, T.; Kitazawa, K. Observation of Mott Localization Gap Using Low Temperature Scanning Tunneling Spectroscopy in Commensurate 1T-TaS_2. *Physical Review Letters* **1994**, *73*, 2103.

(39) Martino, E.; Pisoni, A.; Ćirić, L.; Arakcheeva, A.; Berger, H.; Akrap, A.; Putzke, C.; Moll, P. J.; Batistić, I.; Tutiš, E., et al. Preferential out-of-plane conduction and quasi-one-dimensional electronic states in layered 1T-TaS_2. *npj 2D Materials and Applications* **2020**, *4*, 1–9.

(40) Sipos, B.; Kusmartseva, A. F.; Akrap, A.; Berger, H.; Forró, L.; Tutiš, E. From Mott state to superconductivity in 1T-TaS_2. *Nature Materials* **2008**, *7*, 960–965.

(41) Wang, Z.; Sun, Y.-Y.; Abdelwahab, I.; Cao, L.; Yu, W.; Ju, H.; Zhu, J.; Fu, W.; Chu, L.; Xu, H., et al. Surface-Limited Superconducting Phase Transition on 1T-TaS_2. *ACS Nano* **2018**, *12*, 12619–12628.

(42) Ma, L.; Ye, C.; Yu, Y.; Lu, X. F.; Niu, X.; Kim, S.; Feng, D.; Tománek, D.; Son, Y.-W.; Chen, X. H.; Zhang, Y. A metallic mosaic phase and the origin of Mott-insulating state in 1T-TaS_2. *Nature Communications* **2016**, *7*, 1–8.

(43) Cho, D.; Cheon, S.; Kim, K.-S.; Lee, S.-H.; Cho, Y.-H.; Cheong, S.-W.; Yeom, H. W. Nanoscale manipulation of the Mott insulating state coupled to charge order in 1T-TaS_2. *Nature Communications* **2016**, *7*, 1–6.

(44) Stojchevska, L.; Vaskivskyi, I.; Mertelj, T.; Kusar, P.; Svetin, D.; Brazovskii, S.; Mihailovic, D. Ultrafast switching to a stable hidden quantum state in an electronic crystal. *Science* **2014**, *344*, 177–180.

(45) Vaskivskyi, I.; Mihailovic, I.; Brazovskii, S.; Gospodaric, J.; Mertelj, T.; Svetin, D.; Sutar, P.; Mihailovic, D. Fast electronic resistance switching involving hidden charge density wave states. *Nature Communications* **2016**, *7*, 1–6.

(46) Voigtländer, B., *Scanning probe microscopy: Atomic force microscopy and scanning tunneling microscopy*; Springer: 2015.

(47) Güntherodt, H.-J.; Wiesendanger, R., *Scanning tunneling microscopy I: general principles and applications to clean and adsorbate-covered surfaces*; Springer: 1992.

(48) Wiesendanger, R.; Güntherodt, H.-J.; Baumeister, W., *Scanning tunneling microscopy II: further applications and related scanning techniques*; Springer: 1992.

(49) Wiesendanger, R.; Güntherodt, H.-J., *Scanning tunneling microscopy III: theory of STM and related scanning probe methods*; Springer Science & Business Media: 2013; Vol. 29.

(50) Bardeen, J. Tunnelling from a many-particle point of view. *Physical Review Letters* **1961**, *6*, 57.

(51) Binnig, G.; Rohrer, H.; Gerber, C.; Weibel, E. Surface studies by scanning tunneling microscopy. *Physical Review Letters* **1982**, *49*, 57.

(52) McMillan, W. Landau theory of charge-density waves in transition-metal dichalcogenides. *Physical Review B* **1975**, *12*, 1187.

(53) Nakanishi, K.; Shiba, H. Domain-like incommensurate charge-density-wave states and the first-order incommensurate-commensurate transitions in layered tantalum dichalcogenides. I. 1T-polytype. *Journal of the Physical Society of Japan* **1977**, *43*, 1839–1847.

(54) Nakanishi, K.; Takatera, H.; Yamada, Y.; Shiba, H. The nearly commensurate phase and effect of harmonics on the successive phase transition in 1T-TaS_2. *Journal of the Physical Society of Japan* **1977**, *43*, 1509–1517.

(55) Nakanishi, K.; Shiba, H. Theory of three-dimensional orderings of charge-density waves in 1T-TaX_2 (X: S, Se). *Journal of the Physical Society of Japan* **1984**, *53*, 1103–1113.

(56) Cho, D.; Gye, G.; Lee, J.; Lee, S.-H.; Wang, L.; Cheong, S.-W.; Yeom, H. W. Correlated electronic states at domain walls of a Mott-charge-density-wave insulator 1T-TaS_2. *Nature Communications* **2017**, *8*, 1–6.

(57) Park, J. W.; Cho, G. Y.; Lee, J.; Yeom, H. W. Emergent honeycomb network of topological excitations in correlated charge density wave. *Nature Communications* **2019**, *10*, 1–7.

(58) Park, J. W.; Lee, J.; Yeom, H. W. Zoology of domain walls in quasi-2D correlated charge density wave of 1T-TaS_2. *npj Quantum Materials* **2021**, *6*, 1–6.

(59) Thomson, R.; Burk, B.; Zettl, A.; Clarke, J. Scanning tunneling microscopy of the charge-density-wave structure in 1T-TaS_2. *Physical Review B* **1994**, *49*, 16899.

(60) Zong, A.; Shen, X.; Kogar, A.; Ye, L.; Marks, C.; Chowdhury, D.; Rohwer, T.; Freelon, B.; Weathersby, S.; Li, R.; Yang, J.; Checkelsky, J.; Wang, X.; Nuh, G. Ultrafast manipulation of mirror domain walls in a charge density wave. *Science Advances* **2018**, *4*, eaau5501.

(61) Ravnik, J. Studies of ultrafast processes in correlated materials using scanning tunnelling microscope., Ph.D. Thesis, Univerza v Ljubljani, Fakulteta za matematiko in fiziko, 2019.

(62) Yothers, M. P.; Browder, A. E.; Bumm, L. A. Real-space post-processing correction of thermal drift and piezoelectric actuator nonlinearities in scanning tunneling microscope images. *Review of Scientific Instruments* **2017**, *88*, 013708.

(63) Rahe, P.; Bechstein, R.; Kühnle, A. Vertical and lateral drift corrections of scanning probe microscopy images. *Journal of Vacuum Science & Technology B, Nanotechnology and Microelectronics: Materials, Processing, Measurement, and Phenomena* **2010**, *28*, C4E31–C4E38.

(64) Lawler, M.; Fujita, K.; Lee, J.; Schmidt, A.; Kohsaka, Y.; Kim, C. K.; Eisaki, H.; Uchida, S.; Davis, J.; Sethna, J., et al. Intra-unit-cell electronic nematicity of the high-T_c copper-oxide pseudogap states. *Nature* **2010**, *466*, 347–351.

(65) Pásztor, Á.; Scarfato, A.; Spera, M.; Barreteau, C.; Giannini, E.; Renner, C. Holographic imaging of the complex charge density wave order parameter. *Physical Review Research* **2019**, *1*, 033114.

(66) Mizes, H.; Park, S.-i.; Harrison, W. Multiple-tip interpretation of anomalous scanning-tunneling-microscopy images of layered materials. *Physical Review B* **1987**, *36*, 4491.

(67) Walker, M.; Withers, R. Stacking of charge-density waves in 1T transition-metal dichalcogenides. *Physical Review B* **1983**, *28*, 2766.

(68) Tanda, S.; Sambongi, T.; Tani, T.; Tanaka, S. X-ray study of charge density wave structure in 1T-TaS_2. *Journal of the Physical Society of Japan* **1984**, *53*, 476–479.

(69) Stahl, Q.; Kusch, M.; Heinsch, F.; Garbarino, G.; Kretzschmar, N.; Hanff, K.; Rossnagel, K.; Geck, J.; Ritschel, T. Collapse of layer dimerization in the photo-induced hidden state of 1T-TaS_2. *Nature Communications* **2020**, *11*, 1–7.

(70) Lee, S.-H.; Goh, J. S.; Cho, D. Origin of the Insulating Phase and First-Order Metal-Insulator Transition in 1T-TaS_2. *Physical Review Letters* **2019**, *122*, 106404.

(71) Meyer, J. C.; Geim, A. K.; Katsnelson, M. I.; Novoselov, K. S.; Booth, T. J.; Roth, S. The structure of suspended graphene sheets. *Nature* **2007**, *446*, 60–63.

(72) Yamaguchi, W.; Shiino, O.; Sugawara, H.; Hasegawa, T.; Kitazawa, K. Surface etching of 1T-TaS_2 with UHV-STM. *Applied Surface Science* **1997**, *119*, 67–75.

(73) Altvater, M. A.; Tilak, N.; Rao, S.; Li, G.; Won, C.-J.; Cheong, S.-W.; Andrei, E. Y. Charge Density Wave Vortex Lattice Observed in Graphene-Passivated 1T-TaS_2 by Ambient Scanning Tunneling Microscopy. *Nano Letters* **2021**, *21*, 6132–6138.

(74) Martinez-Castro, J.; Mauro, D.; Pásztor, Á.; Gutiérrez-Lezama, I.; Scarfato, A.; Morpurgo, A. F.; Renner, C. Scanning tunneling microscopy of an air sensitive dichalcogenide through an encapsulating layer. *Nano Letters* **2018**, *18*, 6696–6702.

(75) He, R.; Okamoto, J.; Ye, Z.; Ye, G.; Anderson, H.; Dai, X.; Wu, X.; Hu, J.; Liu, Y.; Lu, W., et al. Distinct surface and bulk charge density waves in ultrathin 1T-TaS_2. *Physical Review B* **2016**, *94*, 201108.

(76) Wu, X. L.; Lieber, C. M. Hexagonal domain-like charge density wave phase of TaS_2 determined by scanning tunneling microscopy. *Science* **1989**, *243*, 1703–1705.

(77) Burk, B.; Thomson, R.; Zettl, A.; Clarke, J. Charge-density-wave domains in 1T-TaS_2 observed by satellite structure in scanning-tunneling-microscopy images. *Physical Review Letters* **1991**, *66*, 3040.

(78) Wu, X. L.; Lieber, C. M. Direct observation of growth and melting of the hexagonal-domain charge-density-wave phase in 1T-TaS_2 by scanning tunneling microscopy. *Physical Review Letters* **1990**, *64*, 1150.

(79) Uehara, M.; Mori, S.; Chen, C.; Cheong, S.-W. Percolative phase separation underlies colossal magnetoresistance in mixed-valent manganites. *Nature* **1999**, *399*, 560–563.

(80) Dagotto, E.; Hotta, T.; Moreo, A. Colossal magnetoresistant materials: the key role of phase separation. *Physics Reports* **2001**, *344*, 1–153.

(81) Tokunaga, M.; Tokunaga, Y.; Tamegai, T. Imaging of Percolative Conduction Paths and Their Breakdown in Phase-Separated $(La_{1-y}Pr_y)_{0.7}Ca_{0.3}MnO_3$ with y = 0.7. *Physical Review Letters* **2004**, *93*, 037203.

(82) Dagotto, E., *Nanoscale phase separation and colossal magnetoresistance: the physics of manganites and related compounds*; Springer Science & Business Media: 2013; Vol. 136.

(83) Imry, Y.; Wortis, M. Influence of quenched impurities on first-order phase transitions. *Physical Review B* **1979**, *19*, 3580.

(84) Burgy, J.; Dagotto, E.; Mayr, M. Percolative transitions with first-order characteristics in the context of colossal magnetoresistance manganites. *Physical Review B* **2003**, *67*, 014410.

(85) Kirkpatrick, S. Percolation and conduction. *Reviews of Modern Physics* **1973**, *45*, 574.

(86) Patel, T.; Okamoto, J.; Dekker, T.; Yang, B.; Gao, J.; Luo, X.; Lu, W.; Sun, Y.; Tsen, A. W. Photocurrent Imaging of Multi-Memristive Charge Density Wave Switching in Two-Dimensional 1T-TaS_2. *Nano Letters* **2020**, *20*, 7200–7206.

(87) Hollander, M. J.; Liu, Y.; Lu, W.-J.; Li, L.-J.; Sun, Y.-P.; Robinson, J. A.; Datta, S. Electrically driven reversible insulator-metal phase transition in 1T-TaS_2. *Nano Letters* **2015**, *15*, 1861–1866.

(88) Ma, Y.; Wang, Z.; Hou, Y.; Wu, D.; Lu, C.; Petrovic, C. Observation of multiple metastable states induced by electric pulses in the hysteresis temperature range of 1T-TaS_2. *Physical Review B* **2019**, *99*, 045102.

(89) Ludwiczak, K.; Lacinska, E.; Binder, J.; Lutsyk, I.; Rogala, M.; Dabrowski, P.; Klusek, Z.; Stepniewski, R.; Wysmolek, A. Impeded phase transition in 1T-TaS_2: Thermoelectric fingerprint of long-lived mixed states. *Solid State Communications* **2020**, *305*, 113749.

(90) Frenzel, A. J.; McLeod, A. S.; Wang, D. Z.-R.; Liu, Y.; Lu, W.; Ni, G.; Tsen, A. W.; Sun, Y.; Pasupathy, A. N.; Basov, D. Infrared nanoimaging of the metal-insulator transition in the charge-density-wave van der Waals material 1T-TaS_2. *Physical Review B* **2018**, *97*, 035111.

(91) Tanda, S.; Sambongi, T. X-ray study of the new charge-density-wave phase in 1T-TaS_2. *Synthetic Metals* **1985**, *11*, 85–100.

(92) McMillan, W. L. Theory of discommensurations and the commensurate-incommensurate charge-density-wave phase transition. *Physical Review B* **1976**, *14*, 1496.

(93) Grüner, G. The dynamics of charge-density waves. *Reviews of Modern Physics* **1988**, *60*, 1129.

(94) Bu, K.; Zhang, W.; Fei, Y.; Wu, Z.; Zheng, Y.; Gao, J.; Luo, X.; Sun, Y.-P.; Yin, Y. Possible strain induced Mott gap collapse in 1T-TaS_2. *Communications Physics* **2019**, *2*, 1–7.

(95) Battisti, I.; Bastiaans, K. M.; Fedoseev, V.; De La Torre, A.; Iliopoulos, N.; Tamai, A.; Hunter, E. C.; Perry, R. S.; Zaanen, J.; Baumberger, F.; Allan, M. P. Universality of pseudogap and emergent order in lightly doped Mott insulators. *Nature Physics* **2017**, *13*, 21–25.

(96) Sun, Z.; Guevara, J. M.; Sykora, S.; Pärschke, E. M.; Manna, K.; Maljuk, A.; Wurmehl, S.; van den Brink, J.; Büchner, B.; Hess, C. Evidence for a percolative Mott insulator-metal transition in doped Sr_2IrO_4. *Physical Review Research* **2021**, *3*, 023075.

(97) Fradkin, E.; Kivelson, S. A.; Tranquada, J. M. Colloquium: Theory of intertwined orders in high temperature superconductors. *Reviews of Modern Physics* **2015**, *87*, 457.

(98) Chaikin, P. M.; Lubensky, T. C., *Principles of condensed matter physics*; Vol. 10.

(99) Cahn, J. W.; Hilliard, J. E. Free energy of a nonuniform system. I. Interfacial free energy. *The Journal of Chemical Physics* **1958**, *28*, 258–267.

(100) Cahn, J. W. On spinodal decomposition. *Acta Metallurgica* **1961**, *9*, 795–801.

(101) Brough, D. B.; Wheeler, D.; Kalidindi, S. R. Materials knowledge systems in python a data science framework for accelerated development of hierarchical materials. *Integrating materials and manufacturing innovation* **2017**, *6*, 36–53.

(102) Frank, D.; Lobb, C. Highly efficient algorithm for percolative transport studies in two dimensions. *Physical Review B* **1988**, *37*, 302.

(103) McMillan, W. Time-dependent Laudau theory of charge-density waves in transition-metal dichalcogenides. *Physical Review B* **1975**, *12*, 1197.

(104) McLeod, A.; Van Heumen, E.; Ramirez, J.; Wang, S.; Saerbeck, T.; Guenon, S.; Goldflam, M.; Anderegg, L.; Kelly, P.; Mueller, A.; Liu, M. K.; Schuller, I. K.; Basov, D. N. Nanotextured phase coexistence in the correlated insulator V_2O_3. *Nature Physics* **2017**, *13*, 80–86.

(105) Stefanovich, G.; Pergament, A.; Stefanovich, D. Electrical switching and Mott transition in VO_2. *Journal of Physics: Condensed Matter* **2000**, *12*, 8837.

(106) Liu, M.; Wagner, M.; Abreu, E.; Kittiwatanakul, S.; McLeod, A.; Fei, Z.; Goldflam, M.; Dai, S.; Fogler, M.; Lu, J., et al. Anisotropic electronic state via spontaneous phase separation in strained vanadium dioxide films. *Physical Review Letters* **2013**, *111*, 096602.

(107) Qazilbash, M. M.; Brehm, M.; Chae, B.-G.; Ho, P.-C.; Andreev, G. O.; Kim, B.-J.; Yun, S. J.; Balatsky, A.; Maple, M.; Keilmann, F., et al. Mott transition in VO_2 revealed by infrared spectroscopy and nano-imaging. *Science* **2007**, *318*, 1750–1753.

(108) Feenstra, R. Cross-sectional scanning tunnelling microscopy of III-V semiconductor structures. *Semiconductor Science and Technology* **1994**, *9*, 2157.

(109) Chiu, Y.-P.; Huang, B.-C.; Shih, M.-C.; Huang, P.-C.; Chen, C.-W. Atomic-scale mapping of electronic structures across heterointerfaces by cross-sectional scanning tunneling microscopy. *Journal of Physics: Condensed Matter* **2015**, *27*, 343001.

(110) Paul, W.; Miyahara, Y.; Grütter, P. H. Simple Si (111) surface preparation by thin wafer cleavage. *Journal of Vacuum Science & Technology A: Vacuum, Surfaces, and Films* **2013**, *31*, 023201.

(111) Huang, B.-C.; Chiu, Y.-P.; Huang, P.-C.; Wang, W.-C.; Tra, V. T.; Yang, J.-C.; He, Q.; Lin, J.-Y.; Chang, C.-S.; Chu, Y.-H. Mapping band alignment across complex oxide heterointerfaces. *Physical Review Letters* **2012**, *109*, 246807.

(112) Nuffer, R.; Müssig, H.-J.; Dabrowski, J. Cross-sectional STM/STS - a useful tool for identification of dopants in silicon. *Solid-State Electronics* **2000**, *44*, 875–880.

(113) Johnson, M.; Maier, U.; Meier, H.-P.; Salemink, H. Atomic-scale view of AlGaAs/GaAs heterostructures with cross-sectional scanning tunneling microscopy. *Applied Physics Letters* **1993**, *63*, 1273–1275.

(114) Pandey, K. New π-bonded chain model for Si (111)-(2 $\times$ 1) surface. *Physical Review Letters* **1981**, *47*, 1913.

(115) Chen, W.; Madhavan, V.; Jamneala, T.; Crommie, M. Scanning tunneling microscopy observation of an electronic superlattice at the surface of clean gold. *Physical Review Letters* **1998**, *80*, 1469.

Appendices

Introduction

The appendices are organized as follows. In Appendix A additional details are provided regarding the device fabrication and measurement setup of the work presented in Chapters 2 and 3 of this thesis. Appendix B and Appendix C concern separate scanning tunneling microscopy experiments. While these measurements are secondary to the work described in this thesis, they hopefully contain some useful techniques and practical considerations that are of assistance in performing scanning tunneling microscopy successfully.

Appendix A

Fabrication and measurement details

A.1 Fabrication Details

A.1.1 Synthesis of 1T-TaS_2

Single crystals of 1T-TaS_2 were grown by chemical vapor transport with iodine as the transport agent. High-purity Ta (3.5 N) and S (3.5 N) were mixed in chemical stoichiometry and heated at 1123 K for 4 days in an evacuated quartz tube. The harvested TaS_2 powders and iodine (density: 5 mg/cm^3) were then sealed in another quartz tube and heated for 2 weeks in a two-zone furnace, where the source and growth zones were held at 1173 K and 1073 K, respectively. The tubes were then rapidly quenched in cold water to retain the 1T phase.

A.1.2 Electrode fabrication

Electrodes were fabricated on an SiO_2 (285 nm)/Si substrate. Standard electron beam lithography and e-beam metal deposition techniques were used to fabricate 20 μm $\times$ 20 μm pads of Au (12 nm)/Ti (3 nm). An array of 1 μm size markers (Au (7 nm)/Ti (3 nm)) spaced 2 μm apart was deposited on top of the pads. The pads were contacted by larger 120 μm $\times$ 55 μm contacts of Au (60 nm)/Ti (10 nm), fabricated using mask-less photolithography and e-beam deposition.

A.1.3 2D material transfer procedure

To prevent oxidation of the 1T-TaS_2 flakes the exfoliation and transfer of 2D materials was done inside a N_2 filled glovebox with O_2 and H_2O partial pressures below 0.1 ppm. The materials were exfoliated and transferred sequentially on top of each other using the following method:

1. A bulk crystal of the 2D material is exfoliated onto a piece of Scotch tape.
2. A polypropylene carbonate (PPC) thin film is prepared by spin coating (1600 RPM, 30 sec) PPC in an anisole solution (15% PPC by weight) on a glass cover slide. The Scotch tape with the exfoliated flakes is pressed onto the thin film of PPC and then peeled off.
3. The PPC thin film is transferred onto a polydimethylsiloxane (PDMS) stamp sitting on a glass slide.
4. A home-built setup utilizing a motorized arm attached to a microscope is used to identify a suitable flake on the PPC film.
5. The selected flake is aligned with the fabricated electrodes as desired and brought into contact with the substrate. The substrate is then heated to 363 K, causing the PPC to melt and peal off of the glass slide at the point of contact, transferring the flake and PPC film to the substrate.
6. The heater is switched off and the electrodes with the transferred flake and PPC are put into a vacuum chamber for 30 min. before the PPC is washed away in a chloroform bath, leaving only the flake on the substrate.
7. The sample is then rinsed with acetone and isopropanol.

A.2 STM measurements

All STM measurements were performed with an Omicron LT-STM outfitted with four electrical contacts. STM topography was taken in constant-current mode with the bias applied to the tip. Commercial, chemically etched tungsten tips were used for all of the images displayed in this thesis, unless otherwise noted. PtIr tips were prepared by cutting PtIr wire and then mounted into an empty tip holder. The samples were heated to 388 K prior to being transferred to the STM chamber.

Appendix B

Cross-sectional scanning tunneling microscopy

Cross-sectional scanning tunneling microscopy (xSTM) is an experimental technique useful for preparing clean surfaces of semiconductor crystals. A standard STM technique for obtaining a pristine sample is to cleave a crystal *in situ*, exposing a clean surface to image. In xSTM, this technique is adapted for semiconductor wafers. The sample of interested is mounted upright and held in place such that the wafer can be cleaved with a knock of the wobblestick traditionally used to shuttle STM samples through the different chambers of the instrument. A scribe mark is made on the edge of the wafer to facilitate the cleaving of the sample. This method exposes a cross-section of the wafer, opening up the possibilities for a variety of experiments [108, 109]. For example, it can be used to measure surfaces not readily grown [110], mapping the topography and band structures of interfaces of heterostructures [111], probing local effects induced by dopants [112], and measuring compositional spatial variations due to clustering in alloys [113]. In this appendix we first demonstrate the technique of xSTM by presenting data collected from imaging a non-standard cleaved silicon surface, Si (111). We then present preliminary results from attempts to study interfaces of a III-V heterostructure grown via molecular beam epitaxy (MBE). While these experiments ultimately did not prove fruitful, they demonstrate some of the possibilities and limitations of xSTM. All of the STM scans presented were taken at 77 K.

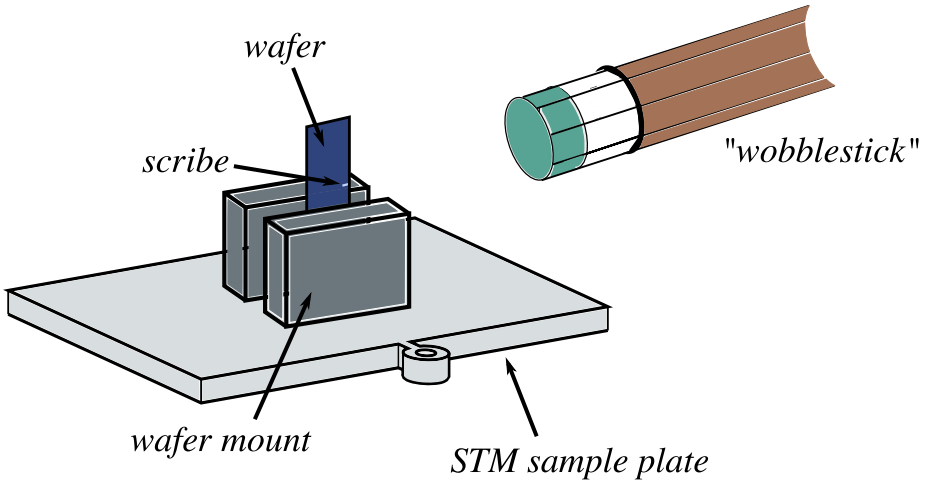

Figure B.1: Schematic of the xSTM set-up. In the figure, a pool cue is used to represent the STM wobblestick.

B.1 Si (111) (2×1) reconstruction

The cleaved Si (111) surface undergoes a (2×1) reconstruction [114].[1] As shown in Figure B.2b, deeper layers of atoms remain in their standard positions, while the topography of the top two layers more closely resembles the Si (110) plane. The displacement of the atoms in the topmost layers results in the observed chain structure outlined in black in Figure B.2a. These chains are associated with the formation of π-bonded surface states. Figure B.2c is an STM scan of the cleaved Si (111) surface. The chain of atoms in the topmost layer is imaged. In this particular scan, a grain boundary in the surface is also clearly resolved.

The xSTM technique is a facile method for preparing a pristine silicon sample [110]. Given the relative ease of cleaving the wafer, a chamber not explicitly designed for this form of sample preparation can be readily adapted. In our case, after machining a sample plate specifically designed to vertically mount a wafer, the cleaving was accomplished simply using the basic wobblestick already present in the preparation chamber of the STM essentially as a pool cue (Figure B.1) The resulting surface is ideal for calibration measurements as the measured lattice displays true atomic resolution, and the tunneling gap achieved is exceptionally stable. Additionally, on Si (111) the xSTM method produces large, flat terraces, opening the possibility of utilizing this technique to locate and probe

[1] In Wood's notation, the surface structure is given as multiples of the standard unit cell.

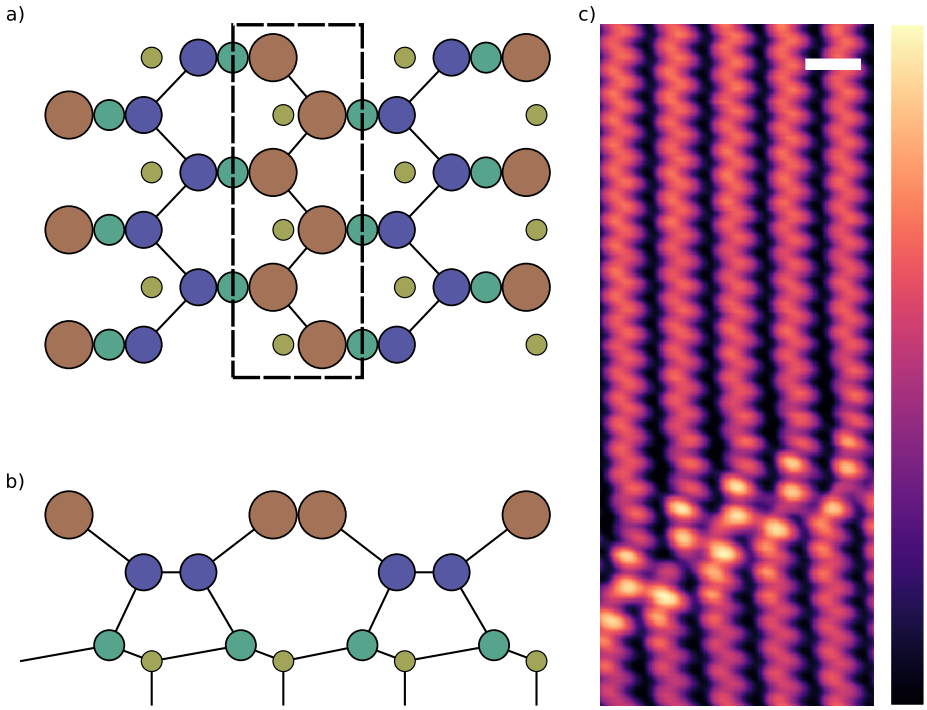

Figure B.2: The Si (111) (2×1) surface reconstruction. (a) Top view. (b) Side view. The atoms are colour and size coded to reflect the different planes of the crystal. (c) The chains of Si atoms (outlined in black in (a)) are imaged in STM. In this particular scan, a grain boundary is also resolved. Scale bar = 0.64 nm, $V_t = 1.20$ V, $I_{set} = 0.15$ nA.

dopants in silicon. The protrusions and depressions in the scan given in Figure B.3a correspond to local disruptions in the atomic structure, such as those caused by the presence of dopants or lattice defects.

B.2 III-V heterostructures

The ability to grow an epitaxial Al layer on a III-V heterostructure is important for the realization of devices that require the semiconductor to be proximitized. In the experiments described in this section, epitaxial Al was grown on a InGaAs buffer with a InP substrate. We attempted to adapt the xSTM technique to probe the Al/InGaAs interface with the goal of determining both the interface quality and whether the Al formed a eutectic with the buffer layer. Given that the substrate is a binary compound while the buffer layer is ternary, one would expect more defects in the buffer layer compared to the InP. These defects would have an effect on the cleaving of the wafer. In the bottom scan in Figure B.4 the InP/InGaAs interface is clearly identifiable due to the abrupt change in the cleavage pattern. The yellow, dashed line in Figure B.4 marks the location of the interface. Although the interface between the substrate and the buffer layer was clearly visible, the Al interface was not distinguishable from an amorphous layer present at the surface of the wafer (top scan in Figure B.4). This result demonstrates some of the limitations of the xSTM technique for probing features near the surface of the wafer. The cleavage process is inherently damaging. While deep within the exposed cross-section, large atomically flat terraces can be located, close to the surface of the wafer, the quality of the cleaved edge is significantly less ideal.

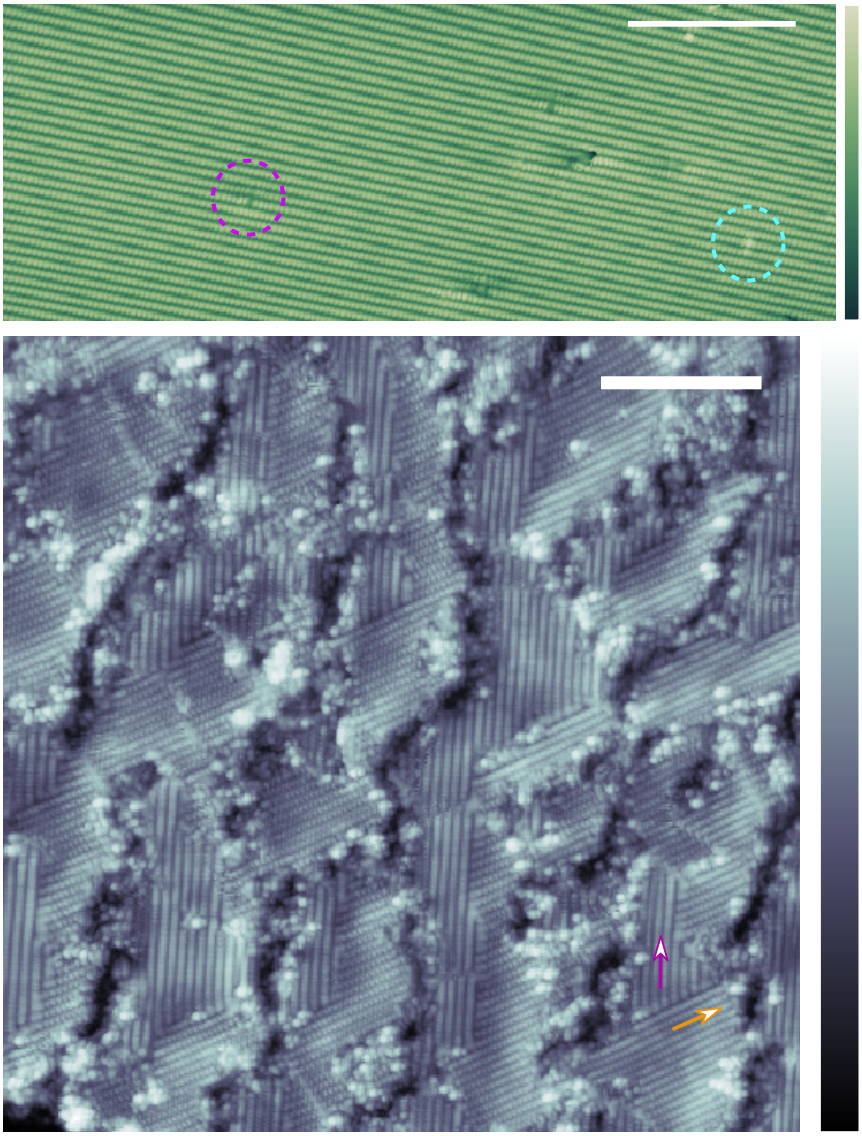

Figure B.3: (Top) Wide terraces are exposed by the xSTM method. On the Si (111) (2×1) surface one can see protrusions and depressions potentially relating to exposed defects and implanted dopants. Scale bar = 20 nm, V_t = 1.20 V, I_{set} = 0.35 nA.. (Bottom) Two different orientations of the reconstruction are visible, as indicated by the purple and orange arrows. In this sample, the prepared surface was significantly more damaged with visible cracks. Scale bar = 10 nm, V_t = 2.00 V, I_{set} = 0.34 nA.

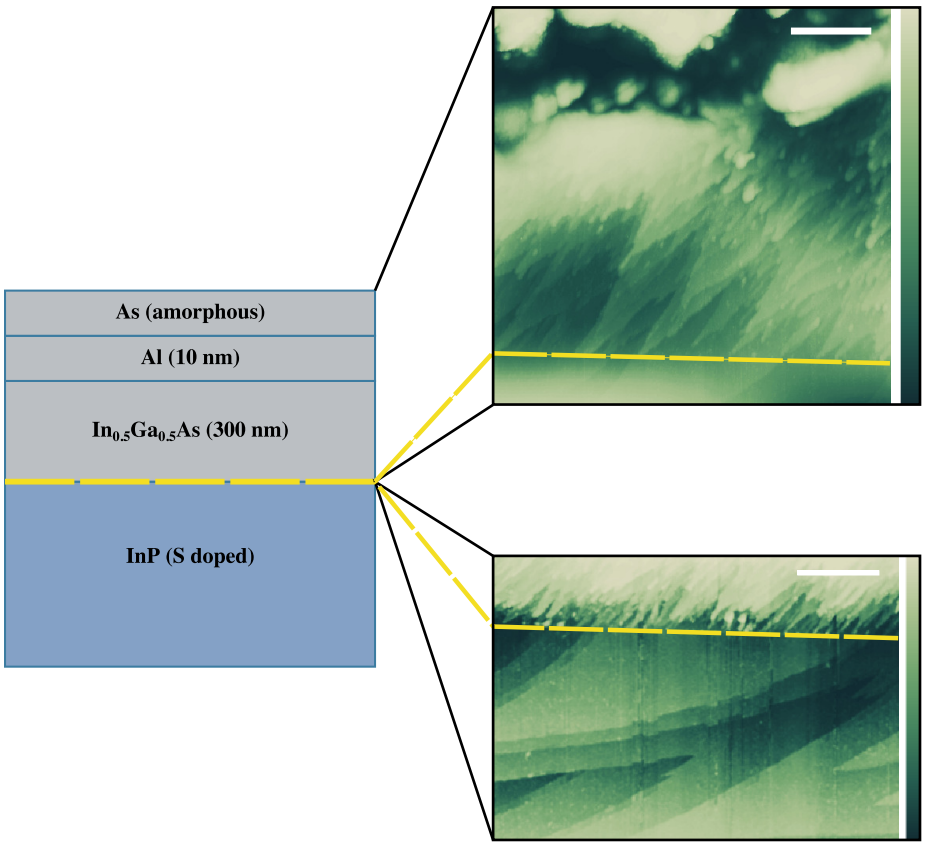

Figure B.4: Cross-section of a III-V heterostructure with epitaxial aluminum on the surface. The interface between the binary substrate InP and the ternary buffer layer $In_{0.5}Ga_{0.5}As$ is marked in yellow. In the top STM scan there exists an amorphous layer that obscures the Al layer. (Top) Scale bar = 40 nm, $V_t = 3.00$ V, $I_{set} = 0.20$ nA. (Bottom) Scale bar = 100 nm, $V_t = 4.00$ V, $I_{set} = 0.20$ nA.

Appendix C

Additional distortion effects in scanning tunneling microscopy

C.1 Hysteretic noise

C.1.1 Au (111)

Au (111) is known to undergo a surface reconstruction and exhibit a characteristic surface state with a herringbone geometry (Figure C.2a) [115]. This sample serves as a useful reference for performing scanning tunneling spectroscopy (STS) experiments, as there is a step in the spectroscopy ($\frac{dI}{dV}$) curve at ≈ 0.45 V. Therefore, Au (111) can be used to calibrate the tip before and after an STS experiment is performed on an unknown sample: by measuring the stepwise $\frac{dI}{dV}$, one can confirm that the density of states of the tip is indeed flat.

We image a Au (111) film grown on mica. All scans were taken at 77 K. In the scans shown in Figure C.1, we observe a form of hysteretic noise. A blurring or streaking occurs at the front of both the forward scan (orange region) and the backward scan (blue region). The blurring was observed as either a fall or a rise in individual line scans. If in the forward direction the effect is seen as a gradual falling, then in the reverse scan it is observed as a gradual rising, and vice versa. This effect was observed over a wide range of parameters, including large variations in scan speeds and the implementation of delay times at the start and end of each scan line.

After cleaning the sample in the preparation chamber with extensive heating, and allowing for the pressure in the chamber to reach normal levels, the hysteresis noise was

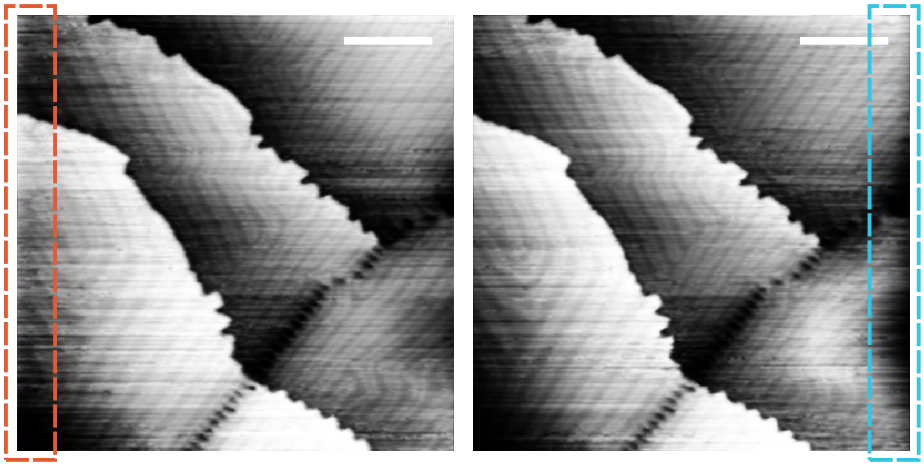

Figure C.1: Hysteretic noise observed when measuring Au (111). Scale bar = 27 nm, $V_t = -0.50$ V, $I_{set} = 0.40$ nA.

no longer visible in the scan. Figure C.2a presents a wide scan of the clean Au (111) surface, demonstrating the herringbone superstructure on multiple terraces. Details of the surface before and after the cleaning are given in Figure C.2b, top and bottom respectively. This example illustrates how contamination on the tip or the sample can manifest itself in unintuitive ways.

C.2 Signs of an irregular tip

C.2.1 Si (111)

Doubling of features When modelling the tunneling current it is commonly assumed that there is only a single source of tunneling electrons from the end of the tip and that the tip possesses spherical symmetry. With these assumption, the measured topography reflects the symmetries of the electronic structure of the sample. In practice, tunneling can occur from multiple atoms on the tip, resulting in artifacts to appear in the topographic scans. The most common evidence for the presence of a non-ideal tip is the multiplying of surface features. This effect is most evident on protruding surface elements, such as either a step or a terrace, or an adsorbed species. The STM scans of Si (111) presented in Figure C.3 exhibit both the doubling of surface adatoms, and that of a step in the sample. Not all surface features may be multiplied, depending on the height offset between the

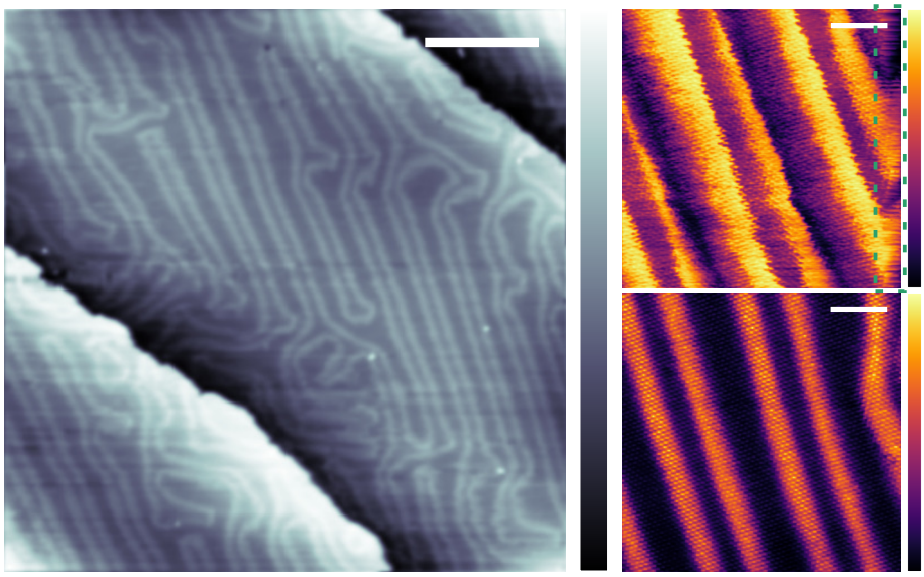

Figure C.2: The Au (111) surface demonstrating the herringbone surface state. The scans on the right illustrate the effects of heating the sample on the observed hysteretic noise depicted in Figure C.1. (Left) Scale bar = 7.6 nm, $V_t = -0.05$ V, $I_{set} = 0.90$ nA. (Top) Scale bar = 2.8 nm, $V_t = -0.40$ V, $I_{set} = 0.10$ nA. (Bottom) Scale bar = 4.55 nm, $V_t = -0.01$ V, $I_{set} = 0.70$ nA.

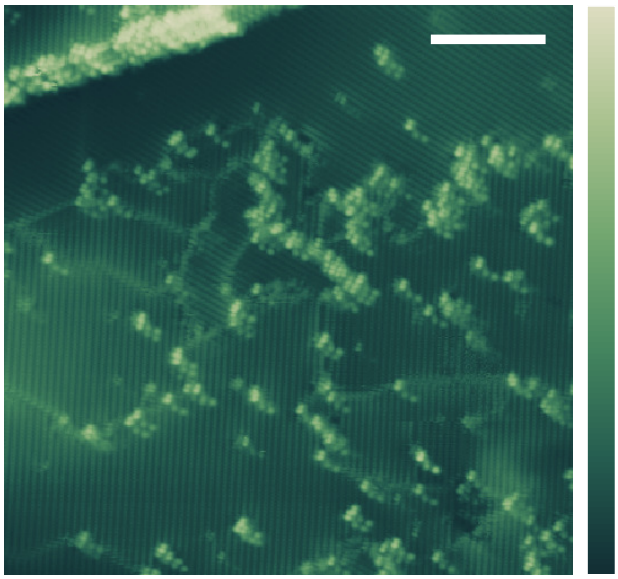

Figure C.3: The multiplying of surface features due to an irregular tip. Scale bar = 10 nm, $V_t = 2.00$ V, $I_{set} = 0.20$ nA.

different atoms of the tip involved in tunneling. This example serves as another reminder that the data collected via STM is a convolution of the tip and the sample. Therefore, the presence of an irregular tip will have consequences on the resulting scan.